

APPLICATIONS OF NONLINEAR OPTICAL GAIN MECHANISMS FROM  
PHONON AND ATOMIC VAPOR INTERACTIONS

A Dissertation

by

CHARLES WESLEY BALLMANN

Submitted to the Office of Graduate and Professional Studies of  
Texas A&M University  
in partial fulfillment of the requirements for the degree of

DOCTOR OF PHILOSOPHY

Chair of Committee,	Marlan O. Scully
Co-Chair of Committee,	Vladislav V. Yakovlev
Committee Members,	Alexei V. Sokolov
	Philip R. Hemmer
	Edward S. Fry
Head of Department,	Peter M. McIntyre

May 2017

Major Subject: Physics

Copyright 2017 Charles Wesley Ballmann

## ABSTRACT

There are many methods to achieve optical gain for laser applications; such methods have been used to make improved spectroscopy and microscopy apparatus. In particular, gain from acoustic and atomic interactions has attained much interest, as is evident in the literature. In this work, we report the results of several experiments involving nonlinear Brillouin scattering and three-level gain in rubidium vapor.

Brillouin scattering, both spontaneous and stimulated, in principle result from the scattering of light off of acoustic waves in a medium. While both spontaneous and stimulated Brillouin scattering have been applied to spectroscopy of various samples, from condensed matter to gases, only spontaneous Brillouin scattering has been used for microscopy purposes. We report our result from several proof-of-principle experiments in which stimulated Brillouin scattering and impulsive stimulated Brillouin scattering were applied to microscopic purposes for the first time. We show the advantages these methods afford over spontaneous Brillouin scattering and make a statistical comparison between them.

There are also many ways to achieve gain in atomic vapors. Using a setup similar to the stimulated Brillouin scattering setup we performed gain in a three-level  $\Lambda$  system in warm rubidium vapor. To our knowledge, this is the first time this three-level analog of Mollow's two-level system with Doppler broadening has been experimentally investigated. Our results show about 0.12% gain in the probe beam.

This work, and extensions of it, should provide additional methods of performing spectroscopy and microscopy in various materials from atoms to bulk matter.

## DEDICATION

To the Holy Triune God: Father, Son, and Holy Spirit. He gave me the strength and wisdom to undertake this journey. To Him I am eternally indebted.

## ACKNOWLEDGMENTS

My work here at Texas A&M University was only possible because of all the help and guidance I received from both the friends and professors here, as well as the physics department staff.

I first and foremost want to express my gratitude to Almighty God for His love, strength and wisdom. I can do nothing apart from Him. He saved me with the sacrifice of His Son, the Lord Jesus Christ, and sustains me through His grace. There were times during graduate school that I became very ill and would not have made it without His Providence. A lifetime of praise could not thank Him enough.

Second I would like to thank my parents, who through many phone calls throughout graduate school, and my visits to them, showed their love and support through this hard time. I also want to thank my siblings for their love and the joy they bring to my life. I also want to thank my grandparents and the rest of my extended family for their prayers and support.

I want to thank the tremendous science, math and engineering professors I had in my undergraduate education. Two professors in particular, Dr. Daniel K. Marble and Dr. Jimmy McCoy, made a tremendous impression on me. Their love of science, professionalism, and rigor in which they taught their courses were exceptionally captivating. Added to this, they cared deeply about their students, and greatly enjoyed seeing their students excel. They went above and beyond in teaching their students and prepared them to succeed anywhere.

I would like to express my gratitude to Dr. Marlan O. Scully, for his support both financial and academic. His example and legacy are truly exemplary, and his leadership and vision of exploring new things is something I wish to continue to cultivate in my own

life. Dr. Alexei V. Sokolov was such a blessing to me and my fellow graduate students. He gave us both guidance and support in both the lab and the classroom and is a vital part of the IQSE group. I took quantum optics from Dr. M. Suhail Zubairy, and his passion and knowledge of his field made the course all that much more enjoyable, as well as my time in graduate school. Dr. Philip R. Hemmer has always provided ideas and experience on any experiments that we were doing and was a tremendous asset to any group collaborations. Dr. Edward S. Fry has always amazed me at the clever ways that he achieved experimental realization of many difficult measurements. In addition, his being department head before and during my first few years at Texas A&M made the college of physics and astronomy the powerhouse it is to this day.

I was at Texas A&M a few years before Dr. Vladislav V. Yakovlev was recruited to the university. Seeing his research and the implications of it, I was hoping I would be able to collaborate with him in the future. This wish became reality, and I performed much of my graduate work under his leadership. I have the most heartfelt thanks for how he runs his group and how he approaches research. I also made many new friends in his labs that were such a blessing to me.

Lastly, I would like to thank all of the fellow graduate students that were either my comrades in coursework or my daily companions in the lab, or both. I would like to thank Dr. Andrew J. Traverso for all that he taught me and others in the lab. He is a good teacher, scientist and friend. I also want to thank Dr. Jonathan V. Thompson, for the help and collaboration together, and being a good friend. We have both faced many difficulties together in graduate school, but together we always found a solution. Many other students and postdocs, a short list being, Dr. Nara Altangerel, Dr. Gombojav O. Ariunbold, Han Cai, Zachary Coker, Dr. Ellie Figueroa, Dr. Brett H. Hokr, Dr. Xia Hua, Dr. John Mason, Dr. Zhaokai Meng, Dawson Nodurft, Dr. Chris O'Brien, Dr. Georgi I. Petrov, Dr. Eyob A. Sete, Dr. Gavriil Shchedrin, Yujie Shen, Dr. Matthew M. Springer, Dr. Benjamin Strycker,

Maria Troyanova-Wood, Dr. Dmitri V. Voronine, Dr. Kai Wang, Dr. Da-Wei Wang, Dr. Zhenhuan Yi, Dr. Luqi Yuan, Alexandra Zhdanova, these all helped me and provided the group with energy and made science fun.

## NOMENCLATURE

SpBS	Spontaneous Brillouin Scattering
SBS	Stimulated Brillouin Scattering
ISBS	Impulsive Stimulated Brillouin Scattering
FFT	Fast Fourier Transform
EIT	Electromagnetically induced transparency
LWI	Lasing without inversion
Rb	Rubidium
$\Omega_B$	Spontaneous Brillouin Shift
LIDAR	Light Detection and Ranging
CW	Continuous Wave

## TABLE OF CONTENTS

	Page
ABSTRACT . . . . .	ii
DEDICATION . . . . .	iii
ACKNOWLEDGMENTS . . . . .	iv
NOMENCLATURE . . . . .	vii
TABLE OF CONTENTS . . . . .	viii
LIST OF FIGURES . . . . .	x
LIST OF TABLES . . . . .	xiv
1. INTRODUCTION . . . . .	1
1.1 Conceptual Framework . . . . .	1
1.2 Literature Review . . . . .	2
1.2.1 Brillouin Scattering Literature . . . . .	2
1.2.2 Background Literature for Three-Level Systems in Rubidium . . . . .	4
1.3 Theoretical Review . . . . .	5
1.3.1 Spontaneous Light Scattering . . . . .	5
1.3.1.1 Intensity of the Scattered Light . . . . .	5
1.3.1.2 Thermodynamic Fluctuations Source of Polarization . . . . .	5
1.3.2 Spontaneous Brillouin Scattering . . . . .	7
1.3.3 Stimulated Brillouin Scattering . . . . .	10
1.3.3.1 Electrostriction . . . . .	10
1.3.3.2 Basic Equations for SBS . . . . .	11
1.3.4 Impulsive Stimulated Brillouin Scattering . . . . .	13
1.3.4.1 Basic Principles of ISBS . . . . .	13
1.3.4.2 Heterodyne Detection in ISBS . . . . .	16
1.3.5 Allan Variance . . . . .	18
2. STIMULATED BRILLOUIN SCATTERING MICROSCOPY . . . . .	23
2.1 Introduction . . . . .	23
2.2 Conceptual Framework . . . . .	26



2.3	Experimental Configuration . . . . .	29
2.4	Experimental Results . . . . .	31
2.5	Discussion . . . . .	34
3.	OPTICAL GAIN IN A DRIVEN THREE-LEVEL $\Lambda$ SYSTEM IN RUBIDIUM	37
3.1	Introduction . . . . .	37
3.2	Experiment . . . . .	38
3.2.1	Experimental Setup . . . . .	38
3.2.2	Experimental Parameters . . . . .	40
3.3	Results and Discussion . . . . .	40
4.	IMPULSIVE STIMULATED BRILLOUIN SCATTERING MICROSCOPY . .	44
4.1	Introduction . . . . .	44
4.2	Conceptual Framework . . . . .	45
4.3	Experimental Configuration . . . . .	47
4.4	Experimental Results . . . . .	49
4.5	Discussion . . . . .	51
5.	STATISTICAL COMPARISON OF SPONTANEOUS AND STIMULATED BRIL- LOUIN SCATTERING . . . . .	54
5.1	Introduction . . . . .	54
5.2	Experimental Configuration . . . . .	55
5.3	Experimental Results . . . . .	57
5.3.1	Impulsive Stimulated Brillouin Scattering Data . . . . .	57
5.3.2	Spontaneous Brillouin Data . . . . .	64
5.4	Discussion . . . . .	65
6.	CONCLUSION AND FURTHER WORK . . . . .	70
	REFERENCES . . . . .	71
	APPENDIX A. COMPUTER CODE FOR SBS MICROSCOPY EXPERIMENT .	83
	APPENDIX B. COMPUTER CODE FOR ISBS MICROSCOPY EXPERIMENT .	111
	APPENDIX C. COMPUTER CODE FOR STATISTICAL COMPARISON EX- PERIMENT . . . . .	117

## LIST OF FIGURES

FIGURE	Page
1.1	Conceptual picture illustrating Bragg scattering of light from a grating. . . . . 7
1.2	Conceptual picture illustrating spontaneous Brillouin scattering. A beam of light is incident from the bottom into the sample. The light is scattered off of the acoustic fluctuations in the material. The shift in frequency of the scattered light is dependent on the angle from which the scattered light is collected. . . . . 9
1.3	Dielectric slab experiencing force due to fringing field. . . . . 10
1.4	Conceptual picture of the SBS process. Two beams, $\omega_1$ and $\omega_2$ , are incident into a medium in a counterpropagating arrangement. The intensity profile of the beams will create and amplify a moving density grating from which further scattering occurs. . . . . 12
1.5	Conceptual picture illustrating impulsive stimulated Brillouin scattering. The two fields are incident from the right. A density grating is induced in the material by the intensity pattern of the pump beam interference. . . . . 14
1.6	Conceptual picture illustrating a common setup for realizing impulsive stimulated Brillouin scattering. The two fields are incident from the right and are diffracted by a transmission grating (TG). The grating is reimaged in the sample by a 4-f lens system. All beams are blocked on the end except the scattered probe and the collinear reference beam for heterodyne detection. . . . . 15
1.7	Sample data of a voltage reading over time. . . . . 19
1.8	Allan variance of the data above. . . . . 21
2.1	Conceptual picture illustrating stimulated Brillouin scattering. The two fields are incident from the left and right at frequencies $f_1$ and $f_2$ respectively. In the center, the waves in the medium represent the density variations (acoustic waves). $L$ is the total interaction length in the sample. (Figure graphic generated in Mayavi2 [1]) . . . . . 27

2.2	Schematic of the experimental setup. BS: Beam Splitter, PBC: Polarized Beam Cube, AOM: Acousto-optic Modulator . . . . .	30
2.3	Schematic of the imaging setup. For illustration, the pump and probe beams are red ( $\omega_1$ ) and magenta ( $\omega_2$ ), respectively. Two glass slides are sandwiched together with 1 mm of separation between them and sealed to form a cell that was filled with water. The entire sample was mounted on a motorized xy stage system. See Methods section for further details. . . . .	31
2.4	SBS spectrum of water. The loss and gain peaks on the left and right, respectively, are from SBS while the center feature is from absorptive stimulated Rayleigh scattering. The Brillouin frequency shift is measured to be $\Omega_B/2\pi = 5.04 \pm 0.15$ GHz with a Brillouin linewidth of $\Gamma_B/2\pi = 245 \pm 30$ MHz. The grey and magenta bars at the bottom indicate the frequency ranges used for the background (Figure 4.3b) and signal (Figure 4.3c), respectively, of the image scans. . . . .	32
2.5	a) A picture of the image etched on a clear microscope slide (grey background is the table, yellow scale bar is 1 mm in horizontal direction). The etched lines are $\sim 250 \mu\text{m}$ wide. Scan of the image in water without b) and with c) SBS. The step size is $100 \mu\text{m}$ in each dimension. In b), the resulting image obtained when the frequency scan (per pixel) excludes the SBS gain peak by scanning the $\sim 3\text{--}4$ GHz frequency range indicated by the grey bar in Figure 2.4. In c), the same image scan but with the SBS signal from water obtained by scanning the $\sim 4\text{--}6.3$ GHz region indicated by the magenta line in Figure 2.4. The signal in c) is generated everywhere except where the glass is etched. The signals in b) and c) are normalized with the maximum of c). . . . .	36
3.1	Diagram of the experimental setup. Both the pump and probe are tunable diode lasers (TDL). Both beams are polarization filtered to ensure they have the same polarization at the $\lambda/4$ plate. OI, optical isolator; VA, variable attenuator; SL, spherical lens; PBS, polarized beam splitter; BD, balanced detector; All unmarked mirrors are dielectric mirrors. . . . .	38
3.2	The $D_2$ levels of $^{85}\text{Rb}$ and $^{87}\text{Rb}$ in our cell at natural abundance ( $\approx 72\%$ and $28\%$ of $^{85}\text{Rb}$ and $^{87}\text{Rb}$ respectively). . . . .	41
3.3	Scan of the pump and probe lasers over the $^{85}\text{Rb}$ and $^{87}\text{Rb}$ $D_2$ levels with both beams linearly polarized. The graph data is normalized to the maximum and minimum of the data. . . . .	42

3.4	Scan of the pump and probe lasers over the $^{85}\text{Rb}$ and $^{87}\text{Rb}$ D <sub>2</sub> levels with both beams circularly polarized. The graph data is normalized to the maximum and minimum of the data. We see strong gain around the $F = 2 \rightarrow F'$ transition when the pump is at the $F = 3 \rightarrow F'$ transition in $^{85}\text{Rb}$ . . . . .	43
4.1	Conceptual picture illustrating ISBS. In (a), the pump beam (APLX, 6 ps) is combined with the probe laser (Lion, CW) using a cold mirror (CM) and focused with a cylindrical lens (CL) onto the transmission grating (TG). The grating is then reimaged with a 4f lens telescope ( $f_1$ & $f_2$ ) into the sample and collected on a photodiode (PD). The ISBS process is shown conceptually in (b). The incoming pump pulses intersect and interfere in the medium. This intensity distribution induces a density grating, which may be both acoustic(propagating) and thermal(static). The blue waves illustrate the density variations in the material that make up the induced grating. The probe beam (red) scatters off this grating and is measured. The reference beam from the probe is not shown for clarity. . . . .	47
4.2	(a) A typical ISBS signal (512 averages) from a saturated brine solution ( $\sim 26\%$ NaCl at $\sim 20$ °C) with (b) a corresponding Fourier transform. The dashed red curve in (b) shows a Lorentzian fit to the data. . . . .	49
4.3	ISBS image of four liquids in a window cell. The liquids are (starting from top right and going clockwise) Brine ( $\sim 26\%$ NaCl), tap Water, Isopropyl Alcohol (91%) and Methanol. . . . .	50
4.4	ISBS image of tap water in a Y microchannel cell. The upper middle channel contains a small amount of air, showing that this signal is coming from the water and not geometric scattering. The black outside the channels has a glass signal that is too high for our detection system. . . . .	52
5.1	Simplified schematic of the ISBS setup. The two beams are loosely focused on a transmission grating (TG) and re-imaged on the sample. The signal is then optically filtered and sent to the photodiode. CL - Cylindrical Lens, SL - Spherical Lens, CM - Cold mirror (all other unmarked mirrors are dielectric) . . . . .	56
5.2	Simplified schematic of the SpBS setup. After the interaction the spontaneous Rayleigh scattered light is filtered with a Rb cell. The beam is then focused into a VIPA where it is dispersed. The far field image is collected with a CCD and then analyzed. SL - Spherical Lens, CL - Cylindrical Lens, PC - Polarization Cube . . . . .	57
5.3	ISBS signals from an average of $10^5$ oscilloscope traces for each liquid. The cylindrical lens used to focus onto the transmission grating was 10 cm.	58

5.4	ISBS signals from an average of $10^5$ oscilloscope traces for each liquid. The cylindrical lens used to focus onto the transmission grating was 20 cm.	59
5.5	Simulations of sound waves diffracting through a single slit. (a) and (b) show the diffraction of sound waves generated from our nanosecond pulses using 20 and 10 cm cylindrical lenses, respectively. (c) and (d) show the diffraction of sound waves generated from our picosecond pulses using 20 and 10 cm cylindrical lenses, respectively. The difference in diffraction between nanosecond and picosecond beams is due to the fact that the nanosecond beam has a larger diameter, therefore it focuses down smaller.	61
5.6	The threshold for SBS as a function of pulse length. As pulses get short, the intensity needed to reach threshold quickly rises. . . . .	62
5.7	The Allan variances of the ISBS signal of acetone verses the number of samples taken. . . . .	64
5.8	The Allan variances of the ISBS signal of methanol verses the number of samples taken. . . . .	65
5.9	The Allan variances of the ISBS signal of water verses the number of samples taken. . . . .	66
5.10	SpBS signals of acetone and methanol with 60 mW input power on sample.	67
5.11	The Allan variance of the SpBS signal of acetone and methanol verses the number of samples taken. . . . .	68
5.12	Measured ISBS frequencies using the number of averages required for the minimum uncertainty. . . . .	68
5.13	Measured SpBS frequencies using the number of averages required for the minimum uncertainty. . . . .	69

## LIST OF TABLES

TABLE	Page
3.1 Table of some important experimental parameters. . . . .	40

# 1. INTRODUCTION\*

## 1.1 Conceptual Framework

In this chapter, we will discuss the important parts of the history and theoretical aspects of spontaneous Brillouin scattering, stimulated Brillouin scattering and three level systems.

In chapter 2 we will discuss how we demonstrated two-dimensional stimulated Brillouin scattering microscopy for the first time using low power continuous-wave lasers tunable around 780 nm. Spontaneous Brillouin spectroscopy has much potential for probing viscoelastic properties remotely and non-invasively on a microscopic scale. Nonlinear Brillouin scattering spectroscopy and microscopy may provide a way to tremendously accelerate the data acquisition and improve spatial resolution. This general imaging setup can be easily adapted for specific applications in biology and material science. The low power and optical wavelengths in the water transparency window used in this setup provide a powerful bioimaging technique for probing the mechanical properties of hard and soft tissue.

Experimental setups for two-beam stimulated Brillouin scattering can be very similar to setups for probing two- and three-level systems in atomic vapors. In chapter 3 we report experimentally achieved optical gain of a weak probe beam in a three-level  $\Lambda$  system in a low density Rubidium vapor cell driven by a single pump beam. The maximum measured gain of the probe beam was about 0.12%. This work could lead to new approaches for enhancing molecular spectroscopy applications.

While stimulated Brillouin scattering has many advantage over spontaneous Brillouin

---

\*Portions of this chapter are reprinted with permission from “Stimulated Brillouin Scattering Microscopic Imaging” by Ballmann, C W, Thompson, J V, Traverso, A J, Meng, Z, Scully, M O, Yakovlev, V V, 2015. Scientific Reports, 5, 1–7, Copyright 2015 Nature Publishing Group

scattering, there are still several hindrances to its use. In chapter 4 we show how we have demonstrate an alternative nonlinear Brillouin scattering technique as a solution to many of these hindrances. We demonstrate fast two-dimensional microscopic optical imaging of materials' mechanical properties for the very first time using impulsive stimulated Brillouin scattering. Impulsive stimulated Brillouin scattering (ISBS) was used in a novel optical configuration, which is capable of providing accurate local assessment of viscoelastic properties faster than conventional Brillouin spectroscopy. This proof-of-principle imaging experiment was demonstrated using materials of known properties and microfluidic devices. Applications to non-invasive biomedical imaging are discussed. The fast acquisition times and strong signal of ISBS coupled with the ability of Brillouin scattering to easily measure materials' viscoelastic properties make this an attractive technique for biological use.

In chapter 5, a comparison is made between spontaneous Brillouin scattering (SpBS) and impulsive stimulated Brillouin scattering (ISBS) using statistics of large data samples. ISBS shows promise over conventional spontaneous and stimulated Brillouin scattering in reducing both implementation complexity and data acquisition times. This is especially critical for applications in microscopy. Here, experimental results are compared for SpBS using continuous wave lasers and ISBS performed with nanosecond and picosecond lasers. We calculate the Allan variance of the data to find the optimum number of data needed for each data point. This is especially important for imaging, when the time per pixel is very limited.

## **1.2 Literature Review**

### **1.2.1 Brillouin Scattering Literature**

In Russian literature, the Brillouin scattering effect is called Mandelshtam–Brillouin scattering; however, most all literature today only refers to it simply as Brillouin scat-



tering. Leonid Mandelshtam first described true spontaneous Brillouin scattering, which originates from dissipating fluctuations in a medium, in 1918. However, his results were not published until 1926 [2]. The first published theoretical work predicting the scattering of photons by acoustic phonons was by Brillouin in 1922 [3] and was experimentally verified in crystals and liquids in 1930 by Gross [4]. Over the years, spontaneous Brillouin scattering has been applied to many complex materials such as muscle fibers [5], bone tissue [6], eyes [7], spider silks [8], thin films [9] and quantized spin waves [10]. A few physical properties of materials that spontaneous Brillouin has been applied to are tensile and compressive strain [11], temperature [12], elastic moduli [13, 14], bulk viscosity [15], acoustic velocity, refractive index, and phonon lifetime [16]. Brillouin scattering can be performed using surface acoustic waves as well and not just in bulk material. Surface Brillouin scattering has been used to characterize very hard films [17] and thin metal films [18]. Brillouin scattering has also been proposed for remote sensing [19] such as in Brillouin-LIDAR [20, 21].

Many instrumentation improvements have recently been made for spontaneous Brillouin experiments [22, 23, 24], particularly for biological applications. Since Brillouin scattering is a non-contact, label free method, it has seen many applications in biology for the measurement of properties that would be difficult to measure with other methods. The internal mechanical properties of a single biological cell have been reported using GHz ultrasound imaging induced by ultrashort laser pulses [25, 26], as well as the elastic properties of viruses, which have been assessed using conventional Brillouin spectroscopy [27]. Several studies have been initiated to observe changes in soft tissue due to injury or disease [28, 29, 30]. Confocal Brillouin and Raman microscopy has been combined to give exciting flexibility for a large number of applications, with the ability to measure many properties simultaneously [31, 32]. Recently, we have demonstrated simultaneous imaging spontaneous Brillouin and Raman microscopy [33]; clearly, the same approach

can be extended to nonlinear Brillouin and Raman microscopes, which potentially offer better spatial resolution and faster acquisition rate imaging.

### 1.2.2 Background Literature for Three-Level Systems in Rubidium

Two- and three-level systems have been studied extensively in recent years. Such simple systems are perfect for theoretically and experimentally testing quantum theory and light-matter interactions. Many interesting phenomena, such as resonance fluorescence [34], the Hanle effect [35], lasing without inversion (LWI) [36, 37], electromagnetically induced transparency (EIT) [38], and coherent population trapping [39] are just a few examples of important quantum optical effects demonstrated in such systems. Alkali metal vapors are important in such experiments since these vapors are monatomic elements (however at ultrahigh densities, dimers and trimers start forming as well) and have the lowest ionization energies of the elements, which allows the use of lower frequency light for excitation.

Sources of gain in atomic systems have been an important area of interest as well. Mollow was the first to theoretically consider the effects of a weak probe beam interacting with a two level atom in the presence of a strong pump field [40]. This was experimentally verified by Wu *et al.* in 1977 in an atomic sodium beam [41]. Gain in three level systems has also been theoretically described [42, 43, 44, 45]. However only in [42] and [45] is the absorption of a probe beam in a  $\Lambda$  system with a single pump considered. In [43, 44], a  $\Lambda$  configuration is considered, but almost entirely with two driving fields. Only in [42] is a three-level, non-degenerate  $\Lambda$  system considered where the pump is on resonance with the lower frequency transition.

## 1.3 Theoretical Review

### 1.3.1 Spontaneous Light Scattering

#### 1.3.1.1 Intensity of the Scattered Light

When electromagnetic radiation is incident upon an atom or molecule, an induced dipole moment ensues as a result and it will scatter some the incident light, the intensity of which is given by the time averaged magnitude of the Poynting vector (See Jackson [46], Section 9.2 for a detailed derivation)

$$I_s = \frac{1}{r^2} \frac{dP}{d\Omega} = \frac{n\omega^4 \epsilon_0 |\alpha(\omega)|^2 |\mathbf{E}_0|^2}{8\pi^2 c^3 r^2} \sin^2(\phi). \quad (1.1)$$

Here  $|\mathbf{E}_0|$  is the magnitude of the incident field, and  $\alpha$  is the polarizability of the particle.

#### 1.3.1.2 Thermodynamic Fluctuations Source of Polarization

In the macroscopic case, thermodynamic fluctuations, namely, fluctuations in the dielectric constant, will cause an incident field to scatter. In this case, since

$$\mathbf{P} = \Delta\epsilon \mathbf{E}_0, \quad (1.2)$$

the medium develops an additional polarization due to these fluctuations. The change in the dielectric constant can be written in terms of the density and temperature (see Boyd [16]),

$$\Delta\epsilon = \left( \frac{\partial\epsilon}{\partial\rho} \right)_T \Delta\rho + \left( \frac{\partial\epsilon}{\partial T} \right)_\rho \Delta T. \quad (1.3)$$

However the change in dielectric constant is small for changes in temperature and can be neglected, leaving only the first term. The variation in density can also be written in terms

of fluctuations in the entropy and pressure,

$$\Delta\rho = \left(\frac{\partial\rho}{\partial p}\right)_s \Delta p + \left(\frac{\partial\rho}{\partial s}\right)_p \Delta s. \quad (1.4)$$

The fluctuations in the pressure are adiabatic density fluctuations, while the second term describes isobaric density fluctuations. The first term therefore describes acoustic fluctuations, from which spontaneous Brillouin scattering is a result, while the second term provides scattering from thermal fluctuations, which results in Rayleigh scattering.

Now consider the driven wave equation

$$\nabla^2 E - \frac{n^2}{c^2} \frac{\partial^2 E}{\partial t^2} = \frac{1}{\epsilon_0 c^2} \frac{\partial^2 P}{\partial t^2}. \quad (1.5)$$

The solutions to this equation will of course depend on the source terms. The acoustic waves will obey the equation of motion for a pressure wave (Fabelinskii [47], equation 34.9)

$$\frac{\partial^2 \Delta p}{\partial t^2} - \Gamma' \nabla^2 \frac{\partial \Delta p}{\partial t} - v^2 \nabla^2 \Delta p = 0 \quad (1.6)$$

while the density fluctuations will obey the diffusion equation of the form

$$\rho c_p \frac{\partial \Delta s}{\partial t} - \kappa \nabla^2 \Delta s = 0. \quad (1.7)$$

The diffusion equation of course does not yield propagating waves like the acoustic wave equation above (1.6). Therefore, in the case of Brillouin scattering, the scattered light will be Doppler shifted in frequency, while for Rayleigh scattering the light will have a frequency distribution centered at the frequency of the incident radiation.

### 1.3.2 Spontaneous Brillouin Scattering

Consider the Bragg scattering of light from a moving grating. The path length difference between two light rays can be seen figuratively in figure 1.1. There will only be

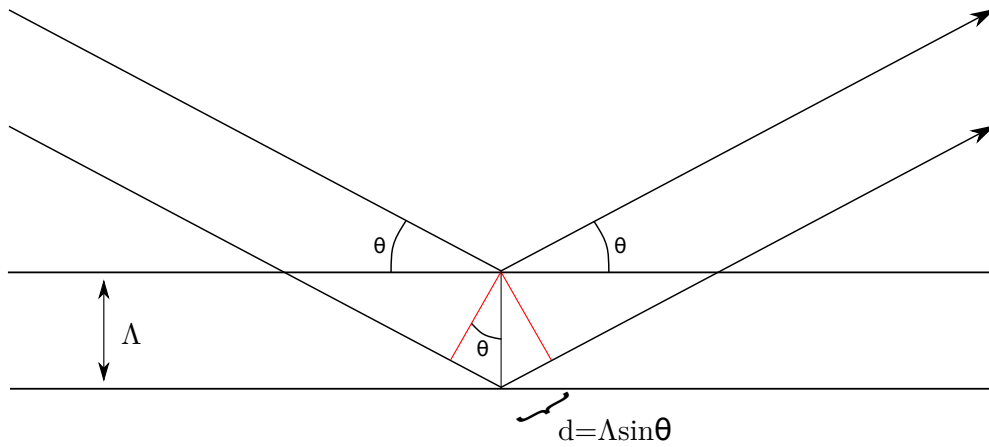


Figure 1.1: Conceptual picture illustrating Bragg scattering of light from a grating.

constructive interference if  $2d = \lambda$ , which means

$$\lambda = 2\Lambda \sin(\theta). \quad (1.8)$$

This wave will satisfy phase matching and be shifted in frequency according to the two relations,

$$\mathbf{k}_2 = \mathbf{k}_1 \pm \mathbf{q} \quad (1.9)$$

$$\omega_2 = \omega_1 \pm \Omega \quad (1.10)$$

where  $\mathbf{k}_1$  and  $\omega_1$  are the incident wavevector and frequency,  $\mathbf{k}_2$  and  $\omega_2$  are the scattered wavevector and frequency,  $\mathbf{q}$  and  $\Omega$  are the acoustic wave wavevector and frequency, and the plus/minus means the wave is traveling towards/away from the incident radiation. The above assumes that the material is thick enough so that the incident light can interact with many wavefronts. This is true as long as

$$\frac{\lambda L}{\Lambda^2} \gg 1, \quad (1.11)$$

where  $L$  is the length of the interaction medium,  $\lambda$  is the incident wavelength, and  $\Lambda$  is the phonon wavelength. In the other limit is Raman-Nath scattering, in which multiple diffraction orders will occur at any angle of incidence.

Having described Bragg scattering from one acoustic wave, now consider scattering from the plethora of spontaneously generated gratings that are inherent in any medium. Figure 1.2 provides a conceptual picture of the SpBS process. A beam of light enters a medium and scatters off of the acoustic fluctuations in the medium. The scattered light is shifted in frequency by  $\pm\Omega$ , where  $\Omega$  is the frequency of the acoustic wave. This shift can be expressed in the following equation,

$$\Omega_B = 2|\mathbf{k}|v \sin(\Theta/2) = 2n\omega\beta \sin(\Theta/2) \quad (1.12)$$

where  $\mathbf{k}$  and  $\omega$  are the wavevector and frequency of the incident light,  $n$  is the index of

refraction,  $\beta = \frac{v}{c}$  where  $v$  is the speed of sound in the material and  $c$  is the vacuum speed of light, and  $\Theta$  is the angle between incident and scattered light.

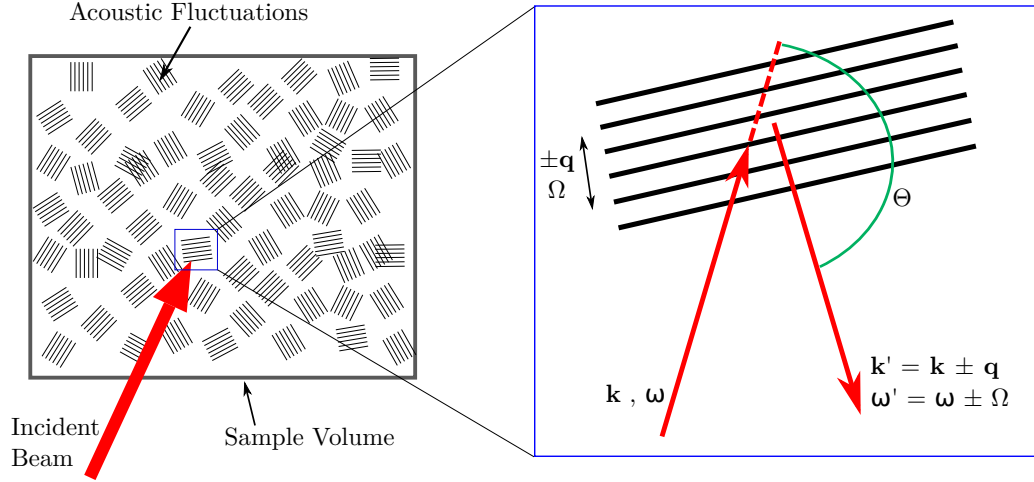


Figure 1.2: Conceptual picture illustrating spontaneous Brillouin scattering. A beam of light is incident from the bottom into the sample. The light is scattered off of the acoustic fluctuations in the material. The shift in frequency of the scattered light is dependent on the angle from which the scattered light is collected.

The scattering off of spontaneous acoustic waves yields a small signal though, and this signal can be dwarfed by spontaneous Rayleigh scattering if special filtering is not implemented. The Landau-Placzek relation (fairly accurate for low dispersive media) gives an estimate of the relative integrated intensities of the spontaneous Rayleigh and Brillouin scattering processes and is given by

$$\frac{I_R}{2I_B} = \frac{c_p - c_v}{c_v} = \gamma - 1, \quad (1.13)$$

where  $I_R$  is the integrated intensity of the center Rayleigh peak,  $I_B$  is the integrated intensity of either Brillouin peak, and where  $c_p$  and  $c_v$  are the specific heat at constant pressure

and volume, respectively. From this relation we see immediately that the center Rayleigh peak will typically be larger than both integrated Brillouin peaks.

### 1.3.3 Stimulated Brillouin Scattering

#### 1.3.3.1 Electrostriction

Consider a dielectric slab placed in a nonuniform electric field as shown in figure 1.3. The slab will experience a force due to the fringing field. Now the force is given by

$$\mathbf{F} = -\nabla U, \quad (1.14)$$

and the energy stored in the capacitor can be written as

$$U = \frac{1}{2} \frac{Q^2}{C}, \quad (1.15)$$

where  $Q$  is the total charge and  $C$  is the capacitance.

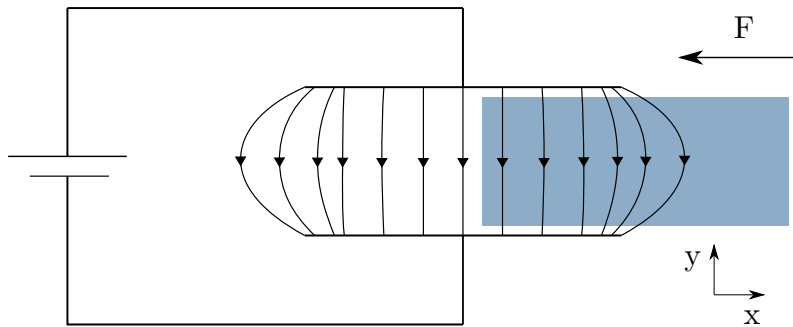


Figure 1.3: Dielectric slab experiencing force due to fringing field.

With the charge held fixed, the capacitance will change as the dielectric moves in the



x direction and the force will be

$$F_x = \frac{d}{dx} \frac{1}{2} \frac{Q^2}{C} = \frac{1}{2} V^2 \frac{dC}{dx}. \quad (1.16)$$

Since a dielectric increases the capacitance, the change in capacitance ( $\frac{dC}{dx}$ ) will be negative since moving in the positive x direction (see figure 1.14) will decrease the capacitance. Therefore the force will be in the negative x direction, pulling the dielectric deeper between the plates (provided that the dielectric slab has a greater electric susceptibility than the medium outside of it).

The same type effect happens to a medium in the presence of a strong optical field. This process is known as electrostriction, and is a central component in SBS creation in media with low absorption.

### 1.3.3.2 Basic Equations for SBS

Consider two laser fields at  $\omega_1$  and  $\omega_2$ , incident upon a medium in a counterpropagating geometry as shown in figure 1.4. The two overlapped beams will beat together at the beat frequency ( $\omega_b = |\omega_1 - \omega_2|$ ) which creates a periodic intensity structure in the medium. As seen above, the medium will move towards the regions of high intensity due to electrostriction. This creates a periodic density distribution in the medium. This grating will be moving at the speed of sound in the medium, and will scatter the beams according to the same principles given above.

Now suppose that  $\omega_2$  is a weak beam,  $\omega_1$  is a strong pump beam, and  $\omega_1 > \omega_2$ . We will now consider what will happen to the  $\omega_2$  beam as it propagates through the medium. The density wave will obey equation 1.6, only now there is a source term on the right hand side. Solving this equation for the density  $\rho(\mathbf{x}, t)$  and using this solution in equation 1.5 will provide, after some work and approximations (see Boyd [16]), the equations for the

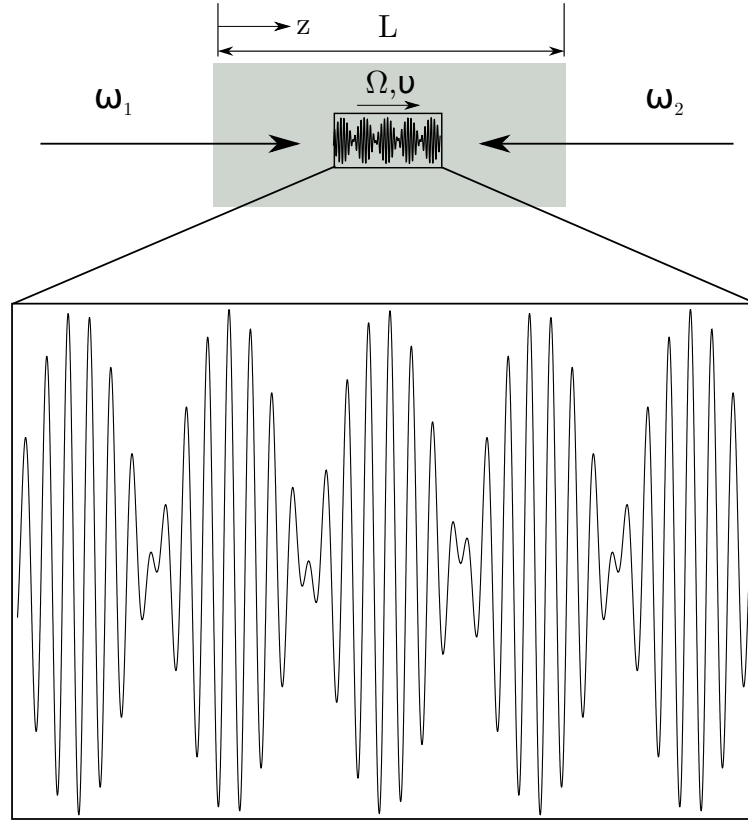


Figure 1.4: Conceptual picture of the SBS process. Two beams,  $\omega_1$  and  $\omega_2$ , are incident into a medium in a counterpropagating arrangement. The intensity profile of the beams will create and amplify a moving density grating from which further scattering occurs.

intensities of the two beams with time and are given by,

$$\frac{dI_1}{dz} = -gI_1I_2 \quad (1.17)$$

$$\frac{dI_2}{dz} = -gI_1I_2 \quad (1.18)$$

A useful approximation to these equations is in the constant-pump limit ( $I_1 = \text{constant}$ ). Equation (1.17) can be quickly solved to yield,

$$I_2(z) = I_2(L)e^{gI_1(L-z)}. \quad (1.19)$$

Therefore the Stokes beam  $I_2$  will experience exponential gain (again, provided the pump is constant). The anti-Stokes beam on the other hand will follow an equation of the form,

$$I_{AS}(z) = I_{AS}(0)e^{-gI_S z}. \quad (1.20)$$

We see that the anti-Stokes component is exponentially attenuated. To see why this is the case, consider the velocity of the sound waves in the medium (again for  $\omega_1 > \omega_2$ )

$$v_s = \frac{\Omega}{q} = \frac{\omega_1 - \omega_2}{k_1 - k_2} = \frac{\Delta\omega}{\Delta k} = v_g. \quad (1.21)$$

We see that the group velocity of the two beating beams is traveling at the speed of sound in the material and in the positive  $z$  direction (see figure 1.4). Therefore, only the sound wave contributing to the Stokes beam is driven and amplified.

### 1.3.4 Impulsive Stimulated Brillouin Scattering

#### 1.3.4.1 Basic Principles of ISBS

ISBS is a form of SBS that has many advantages over traditional SBS such as the ability to control the frequency of the phonon created, the ability to use a pulsed pump source with a narrow-band probe, and ease of implementation.

In ISBS, the pump beam is split in two and then intersected again inside the sample. The interference pattern at the intersection of the two pump beams will form a transient density grating in the medium. For sound waves to be generated electrostrictively, the pump beam has to have enough frequency bandwidth to create and amplify the sound waves following the conditions outlined above, namely, the frequency and wavevector differences have to create a group velocity equal to the speed of sound (1.21). The period of the

induced grating is given by,

$$\Lambda = \frac{\lambda_{\text{pump}}}{2 \sin(\theta_{\text{pump}}/2)} \quad (1.22)$$

where  $\lambda_{\text{pump}}$  is the pump wavelength and  $\theta_{\text{pump}}$  is the angle of intersection of the two pump beams (see figure 1.5). The frequency of the sound wave is given by  $f = v_s/\Lambda$ , where  $v_s$  is the speed of sound in the material and  $\Lambda$  is given by equation 1.22. The condition required for it to be process to be impulsive requires that the temporal length of the pump beams be shorter than one cycle of the acoustic wave.

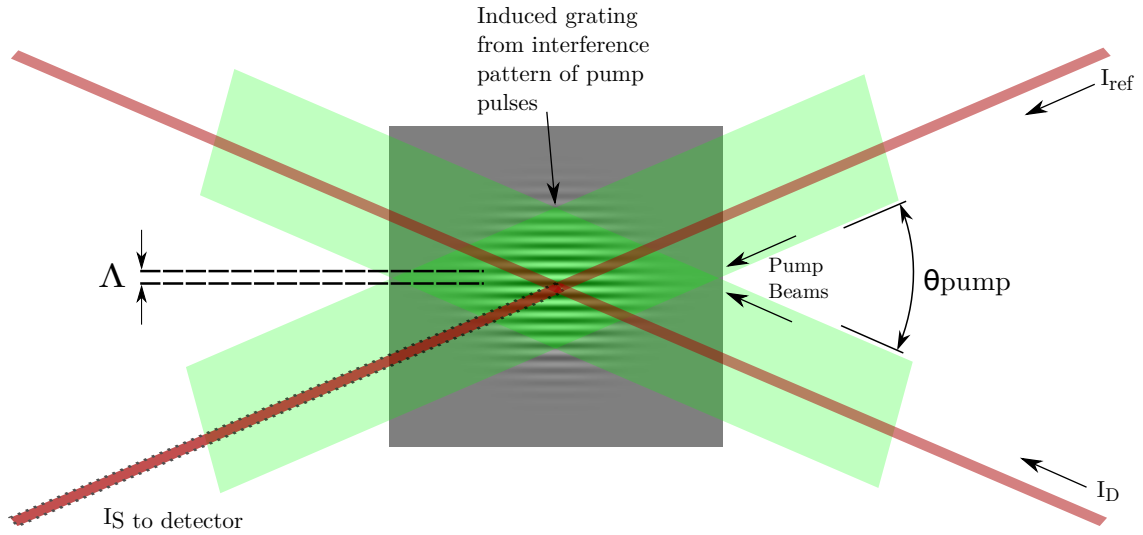


Figure 1.5: Conceptual picture illustrating impulsive stimulated Brillouin scattering. The two fields are incident from the right. A density grating is induced in the material by the intensity pattern of the pump beam interference.

The probe beam, which can be a single beam or two beams in a heterodyne configuration, is Bragg scattered off of this transient grating and collected with a photodiode. An illustration of this process is shown in figures 1.5 and 1.6. Bragg scattering of a beam of light off of a transient grating, formed by standing wave interference in a material from an-

other light beam, was first observed experimentally in 1967 by Boersch and Eichler [48]. A detailed compilation of theoretical and experimental work on dynamic gratings can be found in Ref. [49]. A robust experimental configuration often used to realize ISBS [50] uses a phase mask image which is refocused on the sample as seen in figure 1.6.

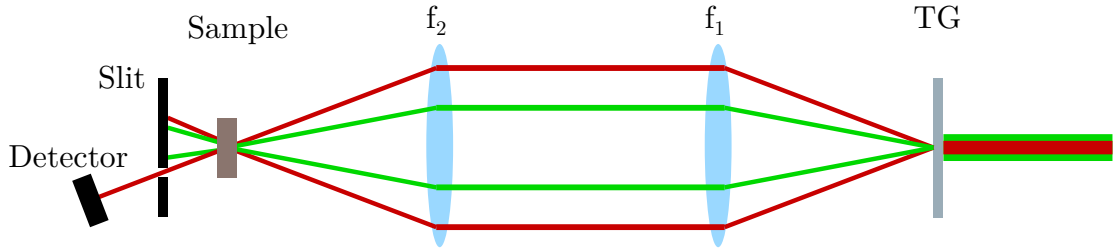


Figure 1.6: Conceptual picture illustrating a common setup for realizing impulsive stimulated Brillouin scattering. The two fields are incident from the right and are diffracted by a transmission grating (TG). The grating is reimaged in the sample by a 4-f lens system. All beams are blocked on the end except the scattered probe and the collinear reference beam for heterodyne detection.

In this way, the Bragg condition is already satisfied so that tedious alignment, as well as delay lines, are avoided. The induced grating wavelength can be expressed as [51],

$$\Lambda_i = \left( \frac{f_2}{f_1} \right) \frac{\Lambda_0}{2}, \quad (1.23)$$

where  $\Lambda_0$  is the grating period and  $f_1$  and  $f_2$  are focal lengths of the two imaging lenses (see Fig. 1.6). The output frequency can then be expressed as

$$f_{signal} = \frac{v_s}{\Lambda_i}. \quad (1.24)$$

### 1.3.4.2 Heterodyne Detection in ISBS

We can then use the diffracted and reference beams (Figure 1.5 or 1.6) in an optical heterodyne detection configuration [51] to increase the signal, which is given by

$$I_S = I_{Ref} + I_R + 2\sqrt{I_{Ref}I_R} \cos(\theta_p), \quad (1.25)$$

where  $\theta_p$  is the phase difference between  $I_{ref}$  and  $I_R$  and  $I_R = \eta I_D$  ( $\eta$  is the diffraction efficiency) is the diffracted portion of  $I_D$ . The last term in equation 1.25 is what is of interest since the signal is multiplied by the reference signal which is quite large in comparison. This amplification effect is one of the main reasons for this heterodyne detection scheme. The signal from electrostrictive ISBS in principle should be at twice the frequency listed above<sup>1</sup>. This is because two counterpropagating sound waves are generated and form a standing wave as they propagate. This standing wave disappears twice each acoustic cycle, therefore the diffracted signal will be modulated at  $2f_{signal}$ . However, in the heterodyne configuration, this is not the case and the signal comes in at  $f_{signal}$ . To see why this is so, consider two probe beams in a heterodyne configuration like outlined above. These probe beams will have the form

$$\mathbf{E}_1(\mathbf{x}, t) = \mathbf{E}_0 e^{i\mathbf{k}_1 \cdot \mathbf{x} - \omega t} \quad (1.26)$$

$$\mathbf{E}_2(\mathbf{x}, t) = \mathbf{E}_0 e^{i\mathbf{k}_2 \cdot \mathbf{x} - \omega t}, \quad (1.27)$$

where we have assumed that both beams have equal intensity for simpler analysis. We will be concerned only with the frequency part of these waves after the interaction. The

---

<sup>1</sup>It also possible to have absorption induced gratings, which will not be at  $2f_{signal}$  but at  $f_{signal}$ . The following argument is confined strictly to electrostrictively generated gratings and the effect that heterodyning has on the observed frequency.

intensity on the photodiode is given by,

$$I_S = |E_{total}|^2 = |\mathbf{E}_1 + \mathbf{E}_2|^2. \quad (1.28)$$

After the interaction, the frequency components from  $\mathbf{E}_1$  and  $\mathbf{E}_2$  will give an  $\mathbf{E}_{total}$  of the form

$$|\mathbf{E}_{total}| = |F(\mathbf{x})F(\omega, \Omega, t)| = |F(\mathbf{x})| |\sin(\omega t) + \eta \sin((\omega + \Omega)t) + \eta \sin((\omega - \Omega)t)|, \quad (1.29)$$

where  $F(\mathbf{x})$  is the functional component of  $\mathbf{E}_{total}$ ,  $\eta$  is the diffraction efficiency, and  $\Omega$  is the frequency of the sound wave. Notice there are  $\pm$  components of  $\Omega$ , one from each of the counterpropagating sound waves. For simplicity, let us rewrite the equation for  $|F(\omega, \Omega, t)|$  and square it to find the signal the diode will see

$$|F(\omega, \Omega, t)|^2 = |\sin(A) + \eta \sin(A + B) + \eta \sin(A - B)|^2, \quad (1.30)$$

where  $A=\omega t$  and  $B=\Omega t$ . Now it can squared out and simplified,

$$\begin{aligned}
|F(\omega, \Omega, t)|^2 &= \\
&= \sin^2(A) + \eta^2 \sin^2(A + B) + \eta^2 \sin^2(A - B) + 2\eta \sin(A) \sin(A + B) \\
&\quad + 2\eta \sin(A) \sin(A - B) + 2\eta^2 \sin(A + B) \sin(A - B) \\
&\approx 2\eta \sin(A) \sin(A + B) + 2\eta \sin(A) \sin(A - B) \\
&\approx 1/2 + 2\eta \cos(B) \\
&= (1/2 - 2\eta) + 4\eta \cos^2(B/2) \\
&\approx 4\eta \cos^2(B/2)
\end{aligned}$$

The terms of order  $\eta^2$  have been dropped since they are very small, and the terms with frequency  $A$  and higher are too fast for the diode response. The last step is a result of the fact that the DC component cannot be seen with AC coupling, but will affect the signal frequency seen. The last term shows that the observed signal will go to zero once each acoustic cycle, so the observed frequency will be at  $f_{signal}$  and not at  $2f_{signal}$ .

### 1.3.5 Allan Variance

In the early days of atomic and crystal clock references it was discovered that in addition to white noise they also contained other noise, such as flicker frequency noise. This noise, which follows a  $1/f$  distribution (pink noise), introduces problems such as the divergence of the standard deviation of the frequency fluctuations vs number of samples taken. Attempts were made to analyze clock stability both experimentally and theoretically [52, 53]. David Allan proposed an  $M$  sample variance that could be used as a way to overcome these characterization problems and also provided a way to convert between the  $M$ -sample variance and a  $N$ -sample variance using a 2-sample variance [54]. The  $M$



sample variance however does not converge for large  $M$ . Still seeking a solution, IEEE later established the 2-sample variance as the preferred method of reference [55].

To understand the concept and importance of using the Allan variance to characterize a sensor, let us consider an example. Figure 1.7 shows voltage readings taken from the analog input of a Microchip ATmega328P microcontroller. An important question to ask is, how many data points are needed to reach the lowest uncertainty attainable? The data set obtained contains a little over 1.2 million data points (though the graphed data has been severely decimated for clarity), but this an impractical amount of data to take for this purpose. It is also not necessary.

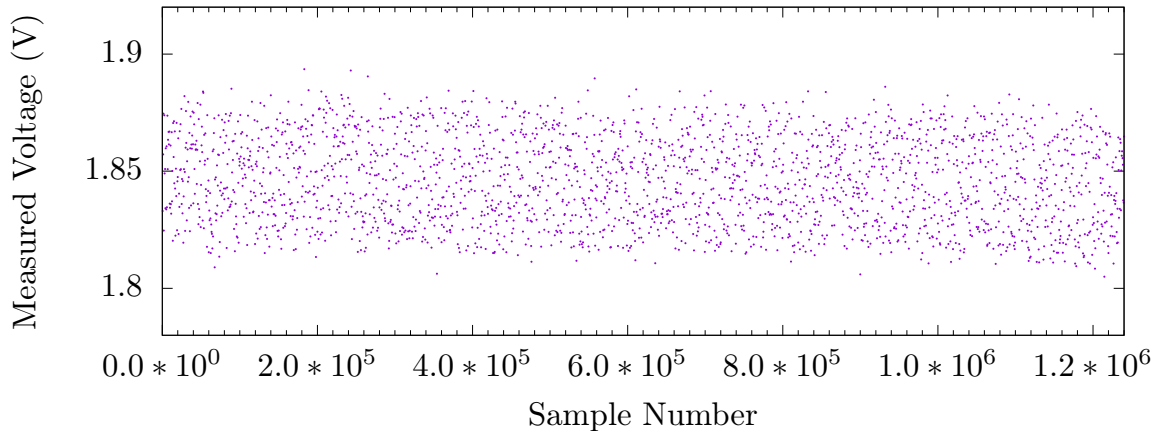


Figure 1.7: Sample data of a voltage reading over time.

Clearly, taking any two random samples has a large uncertainty associated with it, while measurements with 10,000 points averaged will have a much low uncertainty between measurements. Therefore, the variance, or how the variance changes with time, can be used to find the sweet spot of points needed to dependably obtain the lowest uncertainty between consecutive sample periods. The Allan variance finds that minimum point.

The Allan variance is defined as

$$\sigma_y^2(\tau) = \frac{1}{2} \langle (\bar{y}_{n+1} - \bar{y}_n)^2 \rangle, \quad (1.31)$$

where  $\tau$  is the observation period and  $\bar{y}_i$  is the  $n$ 'th averaged data block over the observation time  $\tau$ . To compute the Allan variance then, one can follow the these steps,

1. Split data into group sizes. In this case, we will have 1.24 million groups of one, 620,000 groups of two, 413,333 groups of three, and so one.
2. Now average these groups individually (this is what the bar above the  $y$  means) and subtract the  $n$ 'th group from the  $n-1$ 'th group for all consecutive groups of one, two, etc.
3. Square these all these differences and average them together (the reason for the angled brackets in eq. 1.31).
4. Plot the results (on a Log-Log plot)!

The resulting Allan variance of the data above is shown in figure 1.8 Sometimes the square root of the data is taken and plotted as the Allan deviation. For an example of using this graph as the deviation, consider the point at 30 samples, which give a variance of  $\approx 10^{-6} \text{ V}^2$ . This means that around 32% of the data is greater than 1 mV above the mean and less than -1 mV below the mean.

There are a lot of sources of noise that are discussed in detail elsewhere for Allan variance plots, but I will mention some of the most important features for our purposes.

1. The first point on the graph (sample 1 of figure 1.8) gives a measure of the single point uncertainty of the measuring device. In principle we would like this value to start off as low as possible.

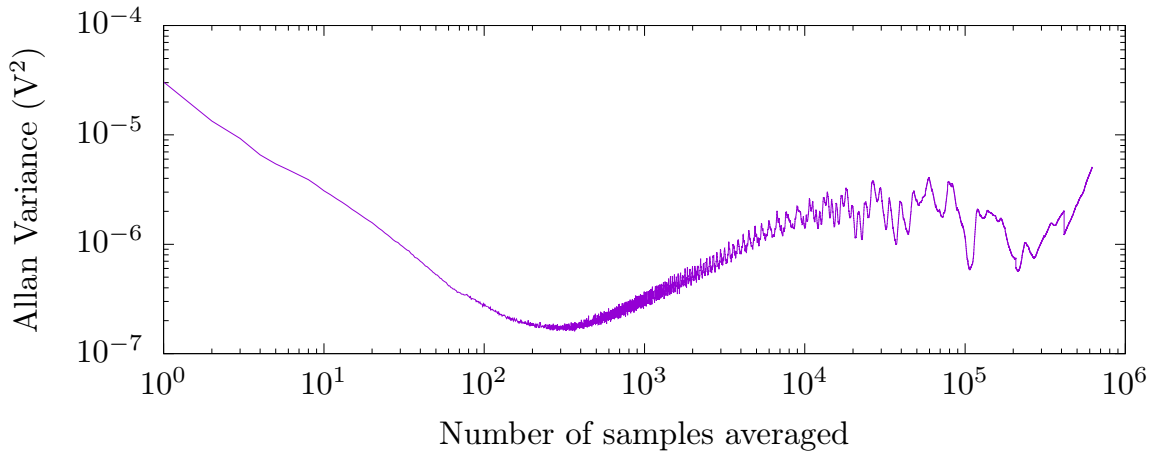


Figure 1.8: Allan variance of the data above.

2. The region from the first point to the minimum uncertainty is a negative sloping line. This is because fast oscillatory noise mostly averages out with increased samples. For some applications, the minimum of uncertainty is not necessary. It is only required that you go below a certain uncertainty. The slope of this line gives a measure of how long you will have to wait to reach that goal. Different sensors will often have different slopes, therefore this gives a measure of what equipment you can use to acquire the data in the required time.
3. The lowest point of the graph is, of course, the minimum of the uncertainty. It is that happy medium where enough averages have been performed to cut down on the fast oscillatory noise, but not too long that slow processes start hurting the data precision. The better the equipment and the more well crafted the experiment, the lower this point will be.
4. After the minimum of uncertainty, it starts to rise again. This is due to long frequency processes, such as random walk, thermal drift, mechanical drift, etc. Some devices have very bad long term noise. So if you have an experiment that you have

to take a measurement once every two days, you will want a device that is as stable as possible in this long term drift region to have consistent data.

## 2. STIMULATED BRILLOUIN SCATTERING MICROSCOPY\*

### 2.1 Introduction

Brillouin scattering originates from a non-elastic light interaction with acoustic waves in a medium that are generated by thermodynamic fluctuations. The scattered light is shifted in frequency according to the relation [47]

$$\Omega_B = 2n\omega\frac{v}{c}\sin(\theta/2), \quad (2.1)$$

where  $n$  is the index of refraction,  $\omega$  is the frequency of the incident light,  $v$  is the speed of sound in the material,  $c$  is the speed of light in vacuum, and  $\theta$  is the angle between the incoming and backscattered light. The speed of sound for a material depends on properties such as compressibility, shear modulus and density for solids, and pressure, density, temperature, composition and heat capacity for non-ideal gases and liquids. Some of these properties listed above are not easily determined by spectroscopy techniques that interact with atomic or molecular energy levels. Brillouin scattering provides a powerful method to assess these properties. In addition, fluorescent methods often require wavelengths in a specific wavelength range, but Brillouin scattering, similar to Raman scattering spectroscopy, will always give a frequency shift. This allows the option for laser sources that are, for example, cheaper and/or have frequencies that scatter (Rayleigh and Mie) less in the material of interest. Since Brillouin scattering is a label-free, frequency independent method, it opens many new possibilities in biosensing and imaging. Brillouin scattering offers a possible route for deep tissue imaging by selecting a longer wavelength where

---

\*Portions of this chapter are reprinted with permission from “Stimulated Brillouin Scattering Microscopic Imaging” by Ballmann, C W, Thompson, J V, Traverso, A J, Meng, Z, Scully, M O, Yakovlev, V V, 2015. Scientific Reports, 5, 1–7, Copyright 2015 Nature Publishing Group

lossy (Rayleigh and Mie) scattering in tissue is relatively small. Furthermore, the generated signal, being very close in wavelength to the incident light, will also have minimal lossy scattering and transmit out of the sample for detection.

The first published theoretical work predicting the scattering of photons by acoustic phonons was by Brillouin in 1922 [3] and was experimentally verified in crystals and liquids in 1930 by Gross [4]. Over the years, spontaneous Brillouin scattering has been applied to many complex materials such as muscle fibers [5], bone tissue [6], eyes [7], spider silks [8], thin films [9] and quantized spin waves [10]. A few physical properties of materials that spontaneous Brillouin has been applied to are tensile and compressive strain [11], temperature [12], elastic moduli [13, 14], bulk viscosity [15], acoustic velocity, refractive index, and phonon lifetime [16]. Brillouin scattering can be performed using surface acoustic waves as well and not just in bulk material. Surface Brillouin scattering has been used to characterize very hard films [17] and thin metal films [18]. Brillouin scattering has also been proposed for remote sensing [19] such as in Brillouin-LIDAR [20, 21].

Many instrumentation improvements have recently been made for spontaneous Brillouin experiments [22, 23, 24], particularly for biological applications. Since Brillouin scattering is a non-contact, label free method, it has seen many applications in biology for the measurement of properties that would be difficult to measure with other methods. The internal mechanical properties of a single biological cell have been reported using GHz ultrasound imaging induced by ultrashort laser pulses [25, 26], as well as the elastic properties of viruses, which have been assessed using conventional Brillouin spectroscopy [27]. Several studies have been initiated to observe changes in soft tissue due to injury or disease [28, 29, 30]. Confocal Brillouin and Raman microscopy has been combined to give exciting flexibility for a large number of applications, with the ability to measure many properties simultaneously [31, 32]. Recently, we have demonstrated simultaneous imaging spontaneous Brillouin and Raman microscopy [56]; clearly, the same approach

can be extended to nonlinear Brillouin and Raman microscopes, which potentially offer better spatial resolution and faster acquisition rate imaging.

Stimulated Brillouin scattering was first observed experimentally by Chiao *et al.* in 1964 [57]. Spontaneous Brillouin scattering becomes stimulated Brillouin scattering when a second counterpropagating beam (with frequency detuned from the first beam by  $\Delta\omega = \pm\Omega_B$ ) causes beating between the fields and enhances the sound wave. This second beam is either a separate probe beam (the method used in this work), or if the incident beam has enough intensity such that backscattered spontaneous Brillouin becomes appreciable, this backscattered light will beat with the incident beam. A striking advantage stimulated Brillouin has over spontaneous Brillouin is that the efficiency of conversion can be much higher, and with sufficient intensities, can approach 100% [16]. In addition, stimulated Brillouin is not encumbered by the large spontaneous Rayleigh peak, the spectral resolution of the obtained spectrum depends only on the linewidth of the lasers used, and the spectral range is limited only by the pump tuning range [58]. All properties that can be measured with spontaneous Brillouin spectroscopy can also be measured with stimulated Brillouin scattering spectroscopy. However, there are limitations to the use of stimulated Brillouin scattering such as power and geometry. For instance, high power lasers with tunable narrowband radiation are not routinely available, and a special arrangement is needed to allow for a counterpropagating probe beam. In addition, laser stability is a significant concern, especially when using a pump-probe setup, and the alignment of the two beams must be very precise for spatial overlap in the focal region. Laser stability and tunability can be overcome by the use of high-speed EOMs [59], in this way the beams are self referenced and drift is no longer a concern.

In the literature, most studies and applications of stimulated Brillouin scattering have been done in optical fibers. Very little has been done to apply it to biology, making it a relatively unexplored subfield of stimulated Brillouin scattering. For spontaneous Brillouin

loun, two [60] and three [7] dimensional imaging has been done, but, to our knowledge, imaging has not been done previously with stimulated Brillouin scattering. Going to stimulated Brillouin has the benefits discussed above, especially high conversion efficiency, wide tuning abilities and no spontaneous Rayleigh peak.

In this work, we apply stimulated Brillouin scattering in a proof-of-principle experiment to perform 2D imaging. A brief theoretical description is given to provide an order of magnitude estimation of signal strength to be compared to the experimental data. Finally, the image results are shown and methods to improve and extend the current setup for more challenging applications are discussed.

## 2.2 Conceptual Framework

Stimulated Brillouin scattering (SBS) can be treated with a general theoretical model of light scattering from inhomogeneous thermodynamic fluctuations caused primarily by fluctuations in pressure (Brillouin) and temperature (Rayleigh) (see, e.g., Boyd [16] Ch. 9). A conceptual picture of stimulated Brillouin for counterpropagating pump and probe beams is shown in Figure 4.1. The counterpropagating pump and probes beams with center frequencies at  $f_1$  and  $f_2$ , respectively, beat together in the medium, which will generate and amplify the sound wave in the medium which oscillates at the beat frequency  $f_{beat} = |f_1 - f_2|$ . Efficient stimulated Brillouin scattering of the beams will occur only when  $f_{beat} \simeq \Omega_B/2\pi$ . This nonlinear (stimulated) interaction of light with the medium is due primarily to electrostriction and absorption, however absorption is a small effect for SBS except for lossy optical media [16].

In the following derivation and results, we assume that  $\omega_1 > \omega_2$ , but it is easily applied to the other case. Starting with the equation of motion for a pressure wave [47] and using the approximations that phonon propagation distance is small compared to distance that the source term varies dramatically, and assuming steady state conditions, we easily obtain an



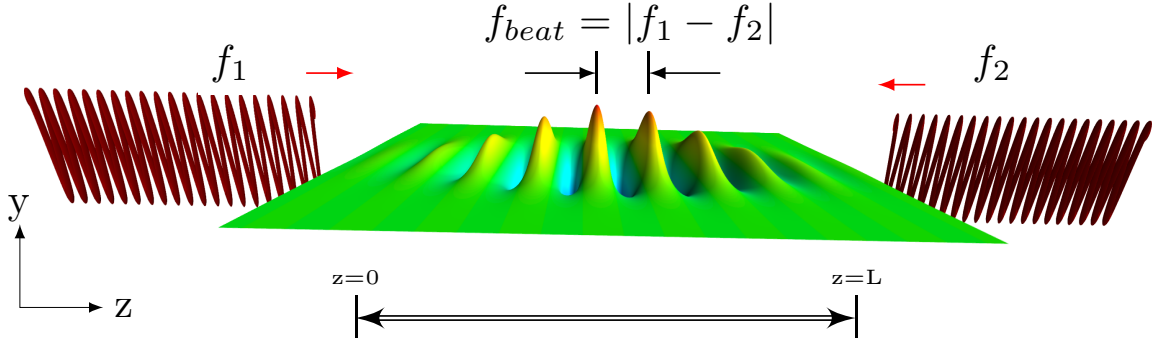


Figure 2.1: Conceptual picture illustrating stimulated Brillouin scattering. The two fields are incident from the left and right at frequencies  $f_1$  and  $f_2$  respectively. In the center, the waves in the medium represent the density variations (acoustic waves).  $L$  is the total interaction length in the sample. (Figure graphic generated in Mayavi2 [1])

expression for the acoustic waves. This expression is then used as the fluctuating dielectric constant in the expression for the polarization of the medium. This expression and the expressions for the optical fields are then used in the wave equation to determine the field propagation. After making the slowly-varying amplitude approximation, using steady state conditions and setting  $\omega_1 = \omega_2$  (except for frequency difference terms) since  $\omega_1 \simeq \omega_2 = \omega$ , the equations for the spatial rate of change of the intensities of the two fields are

$$\frac{dI_1}{dz} = -gI_1I_2 - \alpha I_1, \quad (2.2)$$

$$\frac{dI_2}{dz} = -gI_1I_2 + \alpha I_2, \quad (2.3)$$

where  $\alpha$  is the optical absorption coefficient and  $g$  is the gain factor for SBS. In equation 2.3, the second term on the RHS has a plus sign since  $I_2$  is propagating in the negative  $z$  direction (see figure 4.1). The gain factor  $g$  can be broken up into electrostrictive and absorptive factors as

$$g_B(\Delta) = g_B^e(\Delta) + g_B^a(\Delta), \quad (2.4)$$

where  $\Delta = \Omega_B - (\omega_1 - \omega_2)$ . For optical materials with low absorption ( $\alpha \leq 10^{-2} \text{ cm}^{-1}$ ), electrostriction is the dominant effect for SBS generation. For our proof-of-principle experiment, we used water, which has an absorption coefficient of  $\alpha \simeq 10^{-2} \text{ cm}^{-1}$  at  $\lambda = 780 \text{ nm}$  [61]. Using equations 2.2 and 2.3, we can derive an expression in the very weak probe and undepleted pump limit for the intensity of the probe after the interaction. For a weak probe and for pump intensities sufficiently low such that spontaneous Brillouin from the pump is weaker than the probe,  $dI_1/dz$  is very small. Therefore, in this limit,  $I_1$  is approximately constant in equation 2.3. In addition,  $\alpha$  is very small in our case, so the second term on the RHS of equation 2.3 will be ignored. Solving this equation (integrating from L to z) with  $\Delta = 0$  yields

$$I_2(z) = I_2(L)e^{g_0 I_1(L-z)}, \quad (2.5)$$

where  $g_0 = g_B(0) \simeq g_B^e(0)$  ( $g_B^a(0)$  has been neglected since it is very small for our case). Equation 2.5 will be used in the results/discussion section to derive the expected order of magnitude for the signal. The exact solutions to equations 2.2 and 2.3 (with  $\alpha = 0$ ) leads to a transcendental equation and must be numerically solved. However, looking at equation 2.3 tells us that increasing the intensity of either or both of the lasers increases the rate of increase of the signal (plotted numerical solutions in [16] show this clearly). The expression for the Brillouin shift is given in equation 2.1, and the Brillouin linewidth (FWHM) can expressed as[16]

$$\Gamma_B = \frac{(2\eta_s + \eta_d)q^2}{\rho_0}, \quad (2.6)$$

where  $\eta_s$  is the shear viscosity coefficient,  $\eta_d$  is the dilational viscosity coefficient,  $q = k_1 + k_2$  is the phonon wavenumber, and  $\rho_0$  is the average density of the material. The

Brillouin gain,  $g_B(0)$  for water is 0.048 m/GW, which is a factor of 3 to 5 less than many alcohols, ketones, or hydrocarbons. Water was chosen for our experiment because the volatility of water is lower than the previous mentioned compounds and was suitable for a long scan with little evaporation.

### 2.3 Experimental Configuration

In the experimental setup (Figure 5.2), a  $\sim 45$  mW tunable CW diode laser (Newport, Inc.; Vortex II TLB-6900) is used as the probe beam. The pump laser used is a  $>100$  mW tunable CW diode laser (Sacher Lasertechnik; Lion TEC-520-0780-100-M). Only the pump wavelength was scanned. The probe laser was tuned to the Rb D<sub>2</sub> transition ( $\lambda = 780.24$  nm) and remained untouched for the rest of the experiment. The pump and probe beams were amplitude modulated (Gooch & Housego; 23080-1-LTD AOM) at 102 kHz and 2 kHz respectively. The high modulation frequency substantially reduces the noise in the sample. The difference frequency was output to the lock-in amplifier (Stanford Research Systems; SR830 DSP) for the reference frequency and the time constant was set to 300 ms. A portion of the probe beam  $\sim 1$  mW was split off after the acousto-optic modulator (AOM) using a CaF<sub>2</sub> window and then attenuated before being used as the reference beam in the balanced detector (New Focus; Nirvana 2007). Both beams were passed through 50  $\mu\text{m}$  pinholes after the AOMs to clean up the spatial beam mode of the diode lasers. The polarization of both beams was filtered by using  $\lambda/2$  waveplates and polarizing beam cubes. After the polarizing beam cubes, the two beams were passed side by side through a  $\lambda/4$  waveplate and converted into circularly polarized light in order to easily separate the two beams after the interaction. The counterpropagating pump and probe beams were then focused on the sample using 35 mm and 25.4 mm lenses respectively.

The estimated diameters at the focus for the pump and probe beams are  $\sim 4$   $\mu\text{m}$  and  $\sim 7$   $\mu\text{m}$  respectively. By the time the pump and probe reach the sample, the average power was

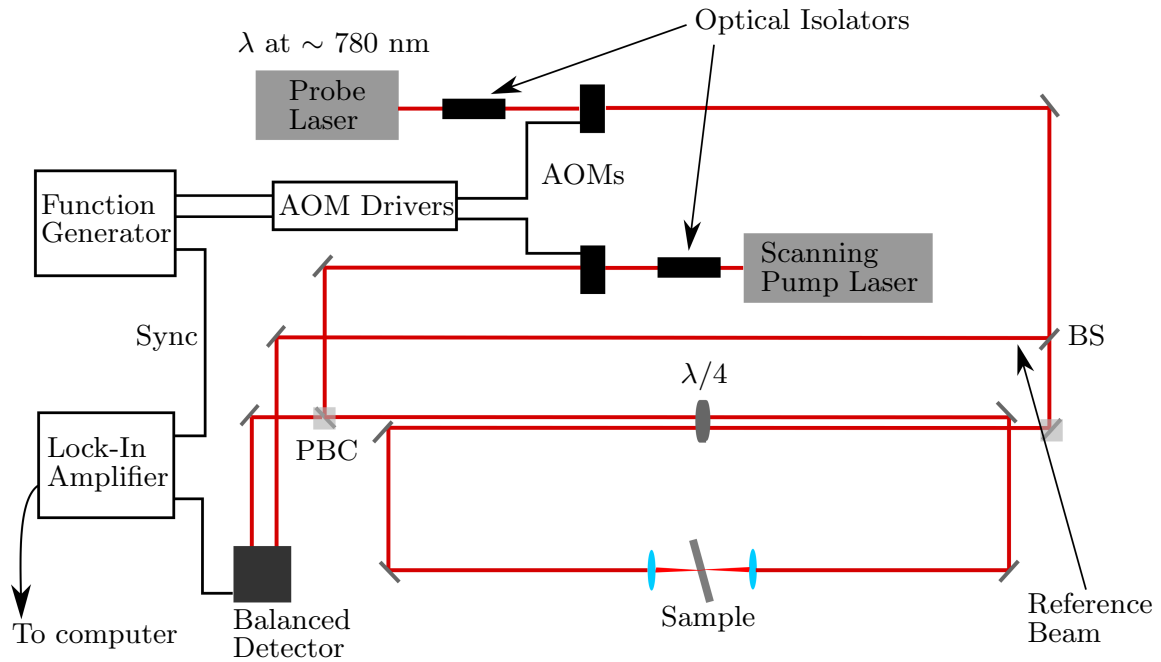


Figure 2.2: Schematic of the experimental setup. BS: Beam Splitter, PBC: Polarized Beam Cube, AOM: Acousto-optic Modulator

25 mW and 8 mW respectively. The sample was mounted on a xy stage system and was tilted to remove back reflections. After interaction, the beams then traveled back through the  $\lambda/4$  waveplate and were now rotated by 90 degrees. In this way, each beam could be removed from the beam paths at the polarization cubes with minimal loss in power. The probe pulse was then attenuated with a neutral density filter ( $\sim 200 \mu\text{W}$ ) and sent into the balanced detector input. The output signal from the balanced detector is first sent in to a highpass filter to remove the low frequency probe modulation and then sent into the lock-in amplifier. Both lasers, the lock-in amplifier and the xy stage were connected and controlled by a computer using NI LabVIEW<sup>TM</sup>. All optics used had an anti-reflective coating for 780 nm.

## 2.4 Experimental Results

A close-up schematic of the imaging setup is shown in Figure 5.1. A fixed probe laser and a tunable, counterpropagating pump laser are focused inside a sample to generate the SBS signal. The sample is mounted on a computer controlled xy stage system and scanned across the overlapped focal region of the two counterpropagating beams.

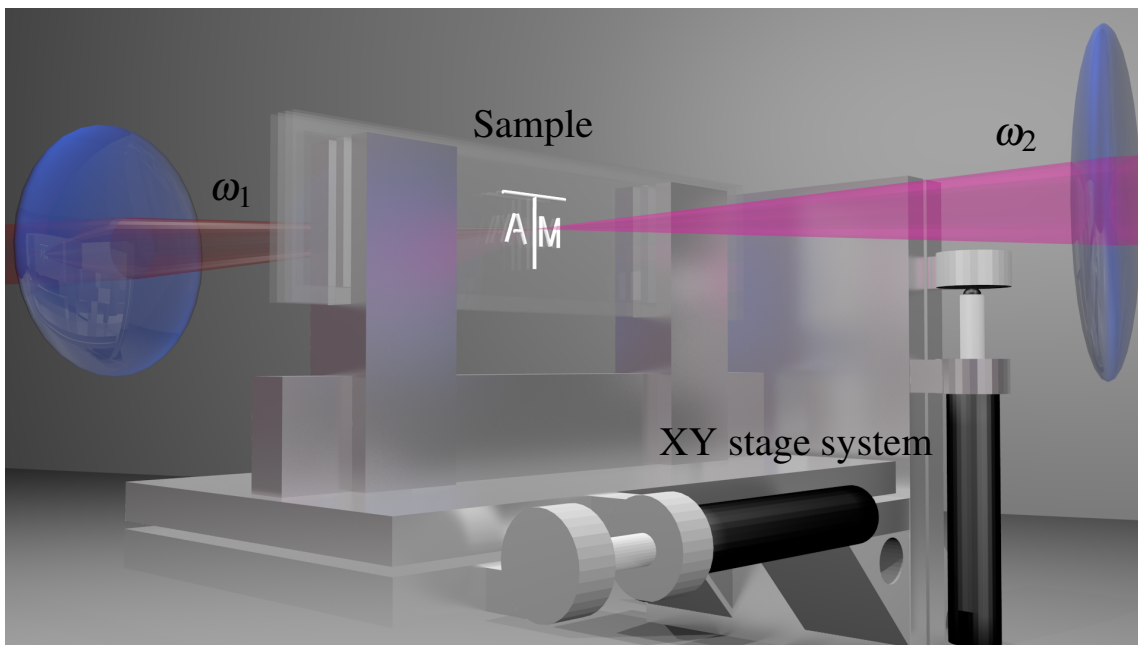


Figure 2.3: Schematic of the imaging setup. For illustration, the pump and probe beams are red ( $\omega_1$ ) and magenta ( $\omega_2$ ), respectively. Two glass slides are sandwiched together with 1 mm of separation between them and sealed to form a cell that was filled with water. The entire sample was mounted on a motorized xy stage system. See Methods section for further details.

Figure 2.4 shows a SBS spectrum of  $\text{H}_2\text{O}$  ( $T = 20.5^\circ\text{C}$ , reverse osmosis filtered) at one spot on the sample. The scan was performed using a  $\sim 26$  MHz step size. Using the formulas above, the Brillouin shift and linewidth are calculated to be  $\Omega_B/2\pi \simeq 5.06$  GHz and  $\Gamma_B/2\pi \simeq 300$  MHz (using [62] for viscosity coefficients), and are measured to

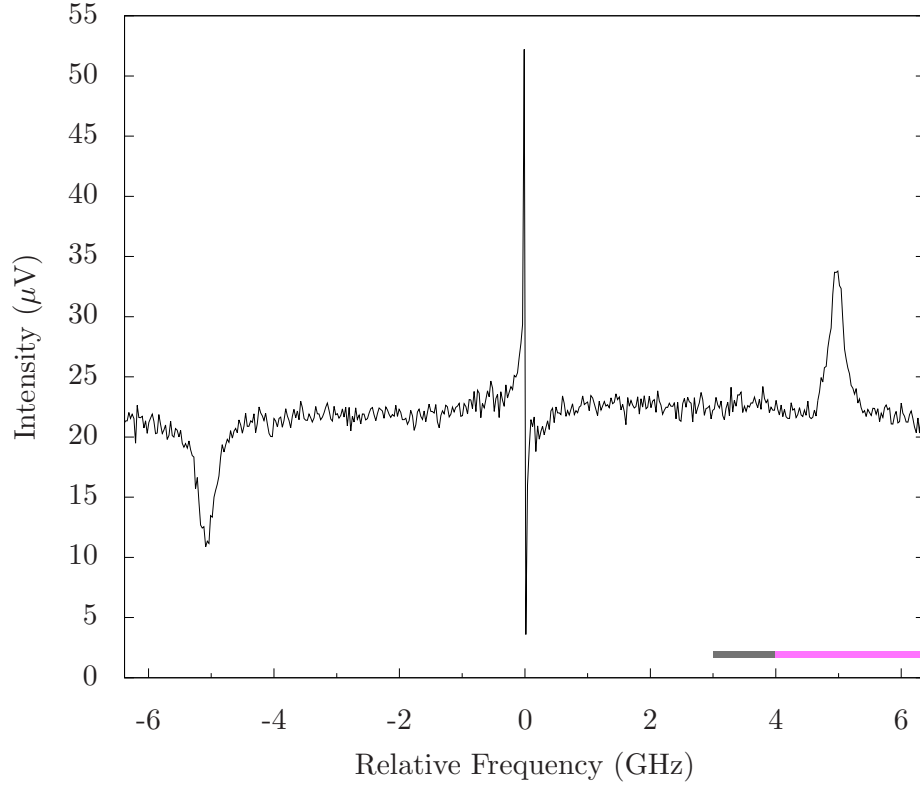


Figure 2.4: SBS spectrum of water. The loss and gain peaks on the left and right, respectively, are from SBS while the center feature is from absorptive stimulated Rayleigh scattering. The Brillouin frequency shift is measured to be  $\Omega_B/2\pi = 5.04 \pm 0.15$  GHz with a Brillouin linewidth of  $\Gamma_B/2\pi = 245 \pm 30$  MHz. The grey and magenta bars at the bottom indicate the frequency ranges used for the background (Figure 4.3b) and signal (Figure 4.3c), respectively, of the image scans.

be  $\Omega_B/2\pi = 5.04 \pm 0.15$  GHz and  $\Gamma_B/2\pi = 245 \pm 30$  MHz. This is in agreement with previous experiments [16]. The dip on the left (at  $\sim -5$  GHz) and peak on the right (at  $\sim 5$  GHz) of zero are the stimulated Brillouin loss and gain peaks, respectively, caused by the first term on the RHS of equation 2.4. The center feature is caused by absorptive stimulated Rayleigh scattering. The signal to noise for this experiment is calculated to be  $\sim 15$  for SBS in Figure 2.4. For an order of magnitude calculation of the expected signal, we can use equation 2.5 (since the approximations for deriving equation 2.5 are valid) for the signal after the interaction  $I_{\text{out}} = I_{\text{probe}}(L)e^{g_0 I_{\text{pump}} L}$ , where  $g_0$  is the max SBS gain

and  $L$  is the total interaction length. For our case,  $g_0 = 0.048 \text{ m/GW}$ ,  $L \simeq 2z_R \sim 100 \mu\text{m}$  ( $z_R$  is the Rayleigh length; the signal will come almost entirely where the intensity is the largest), and  $I_{\text{pump}} \simeq 0.6 \text{ GW/m}^2$ . This yields  $g_0 I_{\text{pump}} L \simeq 3 \times 10^{-6}$ . Therefore,  $I_{\text{out}} \simeq I_{\text{probe}}(1 + 3 \times 10^{-6}) = I_{\text{probe}} + I_{\text{probe}} \times (3 \times 10^{-6}) = I_{\text{Common Mode}} + I_{\text{Signal}}$ . From this we see that the maximum SBS signal going into the detector is about  $10^{-6}$  of the total probe power ( $\sim 10^{-4} \text{ W}$ ) going into the detector. Therefore this SBS signal is  $\sim 10^{-10} \text{ W}$ . The shot noise limit of the balanced detector used is  $\sim 120 \text{ dB}$ , and the best common mode rejection ratio is close to this ( $\sim 118 \text{ dB}$ ), therefore the weak signal ( $I_{\text{Signal}}$ ) will experience  $\sim 10^5$  gain with respect to gain of the common mode probe signal ( $I_{\text{Common Mode}}$ ). The detector has  $\sim 5 \times 10^5 \text{ V/W}$  gain which amplifies the signal to  $\sim 10^{-5} \text{ V}$ . As can be seen in Figure 2.4, this is about the expected order of magnitude.

In our experiment, we obtained a 2D image with SBS by scanning a limited region in frequency covering the gain peak for each pixel in the image. For Figure 4.3c, each pixel scan took  $\sim 1$  min to obtain with the frequency scan range from  $\sim 4$ –6.3 GHz (magenta bar in Figure 2.4). The spatial scan step size was  $100 \mu\text{m}$  in both dimensions. Figure 4.3b is a comparison image that was taken with frequency scans from  $\sim 3$ –4 GHz (grey bar in Figure 2.4), so the SBS signal is not present. The sample consisted of two glass slides separated by 1 mm with water sealed between them. On one slide, the logo was etched on the inside of the glass by a  $\text{CO}_2$  laser cutting machine (Figure 4.3a). The lines making up the letters are  $\sim 250 \mu\text{m}$  wide. This etch frosts the glass and attenuates the probe beam when scanning over it. Therefore, the signal from water is everywhere except where the logo blocks the probe. By performing a frequency scan (scanning range  $\sim 2.3$  GHz with  $\sim 50$  MHz steps) for each pixel, a good signal to noise ratio was obtained to discern between signal and backscattered light. In addition, these scans allow for the small drift in the lasers over the duration of the scan without having to lock them.

## 2.5 Discussion

The present imaging configuration is time consuming and would not be practical for real world applications. Fortunately, this setup can be easily modified to perform similar imaging at much higher acquisition speeds with improved spatial and spectral resolution. For example, a tremendous improvement in frequency stability and low acquisition time can be achieved by implementing a high frequency EOM to create a Stokes/anti-Stokes pair [59] and a virtually imaged phased array (VIPA) with a CCD for faster signal acquisition. In the theory section, we discussed that increasing the intensity of either or both fields will yield a stronger signal. Therefore, using either more powerful CW lasers or using pulsed lasers would yield a stronger signal. In addition, photons at wavelengths longer than 1000 nm greatly reduce optical damage and penetrate biological samples well due to



low absorption and small Rayleigh and Mie scattering cross sections. However, optical damage is also inversely proportional to the pulse length due primarily to multi-photon effects [63, 64, 65]. Therefore, care should be taken when using short-pulsed (pulse durations of a few picoseconds or less) lasers, especially on biological samples. With low power, low frequency CW lasers, such nonlinear effects are no longer a concern. In this setup, instead of generating a large signal from high power lasers, we focused on better signal sensitivity. This resulted in a measurable signal with pump and probe powers as low as 10 mW and 5.5 mW respectively. However, for many materials the SBS gain ( $g_B(0)$ ) is small (compared to  $g_B(0)$  of water), making detection difficult. By switching to lasers with outputs around several hundred milliwatts, this would drastically increase our SBS signal.

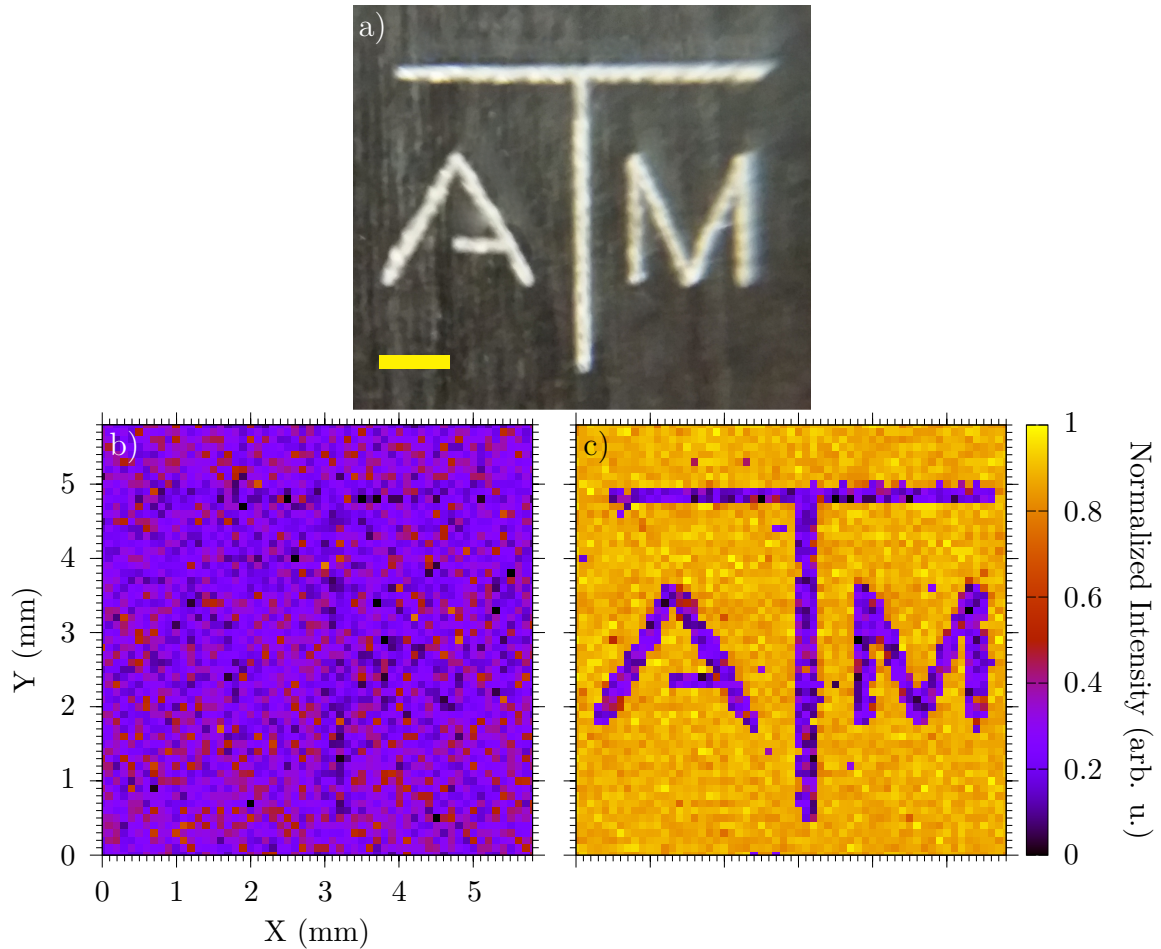


Figure 2.5: a) A picture of the image etched on a clear microscope slide (grey background is the table, yellow scale bar is 1 mm in horizontal direction). The etched lines are  $\sim 250 \mu\text{m}$  wide. Scan of the image in water without b) and with c) SBS. The step size is  $100 \mu\text{m}$  in each dimension. In b), the resulting image obtained when the frequency scan (per pixel) excludes the SBS gain peak by scanning the  $\sim 3\text{--}4$  GHz frequency range indicated by the grey bar in Figure 2.4. In c), the same image scan but with the SBS signal from water obtained by scanning the  $\sim 4\text{--}6.3$  GHz region indicated by the magenta line in Figure 2.4. The signal in c) is generated everywhere except where the glass is etched. The signals in b) and c) are normalized with the maximum of c).

### 3. OPTICAL GAIN IN A DRIVEN THREE-LEVEL $\Lambda$ SYSTEM IN RUBIDIUM

#### 3.1 Introduction

Two- and three-level systems have been studied extensively in recent years. Such simple systems are perfect for theoretically and experimentally testing quantum theory and light-matter interactions. Many interesting phenomena, such as resonance fluorescence [34], the Hanle effect [35], lasing without inversion (LWI) [36, 37], electromagnetically induced transparency (EIT) [38], and coherent population trapping [39] are just a few examples of important quantum optical effects demonstrated in such systems. Alkali metal vapors are important in such experiments since these vapors are monatomic elements (however at ultrahigh densities, dimers and trimers start forming as well) and have the lowest ionization energies of the elements, which allows the use of lower frequency light for excitation.

Sources of gain in atomic systems have been an important area of interest as well. Mollow was the first to theoretically consider the effects of a weak probe beam interacting with a two level atom in the presence of a strong pump field [40]. This was experimentally verified by Wu *et al.* in 1977 in an atomic sodium beam [41]. Gain in three level systems has also been theoretically described [42, 43, 44, 45]. However only in [42] and [45] is the absorption of a probe beam in a  $\Lambda$  system with a single pump considered. In [43, 44], a  $\Lambda$  configuration is considered, but almost entirely with two driving fields. Only in [42] is a three-level, non-degenerate  $\Lambda$  system considered where the pump is on resonance with the lower frequency transition.

We report experimental results with similar gain to that proposed in [42]. We briefly outline our experimental procedure and then present our results and discussion is made between the results as well as possible applications.

## 3.2 Experiment

In this section, we present our experimental setup to achieve gain followed by the parameters used in our experiment.

### 3.2.1 Experimental Setup

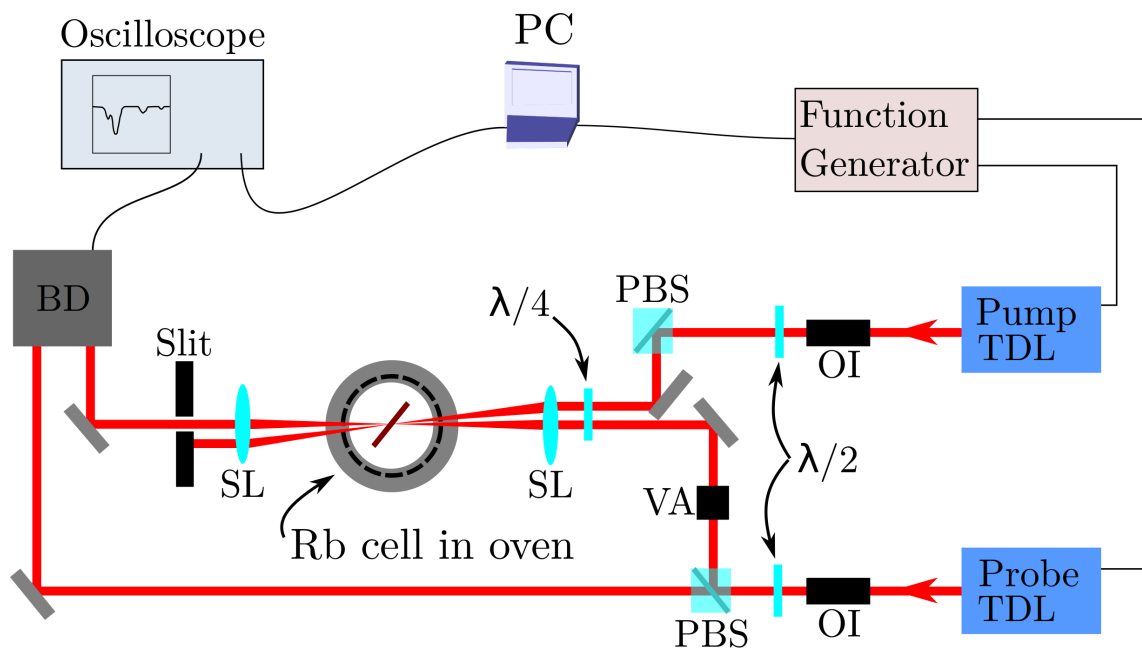


Figure 3.1: Diagram of the experimental setup. Both the pump and probe are tunable diode lasers (TDL). Both beams are polarization filtered to ensure they have the same polarization at the  $\lambda/4$  plate. OI, optical isolator; VA, variable attenuator; SL, spherical lens; PBS, polarized beam splitter; BD, balanced detector; All unmarked mirrors are dielectric mirrors.

Figure 3.1 shows a simplified diagram of the experimental setup. The pump laser consisted of a tunable CW diode laser (Sacher Lasertechnik; Lion TEC-520-0780-100-M) with  $> 100$  mW power and  $\sim 10$  kHz linewidth. The pump laser had wavelength tunability from 763 to 798 nm. The probe laser was a tunable CW diode laser (Newport,

Inc.; Vortex II TLB-6900) with the tuning range centered around 780 nm,  $\approx 45$  mW output power and  $\leq 300$  kHz linewidth. Both the pump and the probe beams are optically isolated and are polarization filtered to both have S-polarization using half-wave plates and polarization beam splitters. Part of the probe beam is split off at this beam splitter and used as the reference input for the balanced detector. The probe passes through a variable attenuator before passing through the quarter-wave plate. Both the pump and probe are then circularly polarized and focused (7.5 cm lenses (Thorlabs, Inc.; LA1608-B)) into the Rb cell. The pump beam is offset to the side of the probe beam and intersects the probe beam at the focus, allowing easy separation of the pump and probe on the other side of the cell. A bichromatic excitation level scheme [66] was used to produce a blue ( $\approx 420$  nm) fluorescence in the vapor that was characterized with a spectrometer to ensure overlap of the beams. This fluorescence is maximized when the overlap is maximized. The Rb cell was not magnetically shielded and no DC magnetic fields were used. A DC power supply was used to provide current to the oven heater elements. After the interaction in the Rb cell (2 mm thick interaction region, sapphire windows, natural abundance of isotopes), the probe beam is collected into the input of the balanced detector (New Focus; Nirvana 2007) and sent to an oscilloscope (Agilent Technologies; DSO6034A, 300 MHz). A computer collects the data from the oscilloscope and controls the function generator. Both the pump and the probe have piezo tunability. The probe beam is frequency modulated (via the internal piezo) with a linear triangle wave across the Rb resonance, while the pump is tuned with a DC bias on its piezo. After each spectrum taken, the bias voltage on the pump piezo is increased and another spectrum is taken, repeating the process until the pump and probe have scanned through all the desired wavelengths. Data is retrieved from oscilloscope and the function generator is controlled by a custom written code in NI LabVIEW™.

### 3.2.2 Experimental Parameters

The experimental parameters are shown in table 3.1. It should be noted that although

Experimental Parameters	
Item	Value
Pump power	70 mW
Probe power	250 $\mu$ W
Rb temperature	55 $^{\circ}$ C
Rb density	$2 \times 10^9 \text{ cm}^{-3}$
Focusing lens	7.5 cm
Polarization	circular

Table 3.1: Table of some important experimental parameters.

the cell is 2 mm thick, it was at a  $45^{\circ}$  angle with respect to the beams to minimize reflections. This gives a modified path length of  $\frac{2}{\cos(45^{\circ})} = 2\sqrt{2}$  mm. The signal will come from the region of highest intensity, which will be about  $2z_R$ , where  $z_R$  is the Rayleigh length. The diameter of each of the beams was about 3 mm before the lens, giving a Rayleigh length of about 2.4 mm. Figure 3.2 shows the  $D_2$  levels of  $^{85}\text{Rb}$  and  $^{87}\text{Rb}$  that are present in our cell. The ground state hyperfine splitting is shown, which is much larger than the first excited state splitting which is shown as several smaller lines [67, 68]. This splitting of the ground level creates the approximate  $\Lambda$  system. In our experiment, when we probed over both levels, the strongest effect came from the  $^{85}\text{Rb}$  system.

### 3.3 Results and Discussion

In the experiment, we first took a full scan of the  $D_2$  resonances with only linear polarization of both beams by removing the quarter-wave plate. The results are shown in figure 3.3. Here we see several effects such as hyperfine pumping [69, 70, 71] and avoided

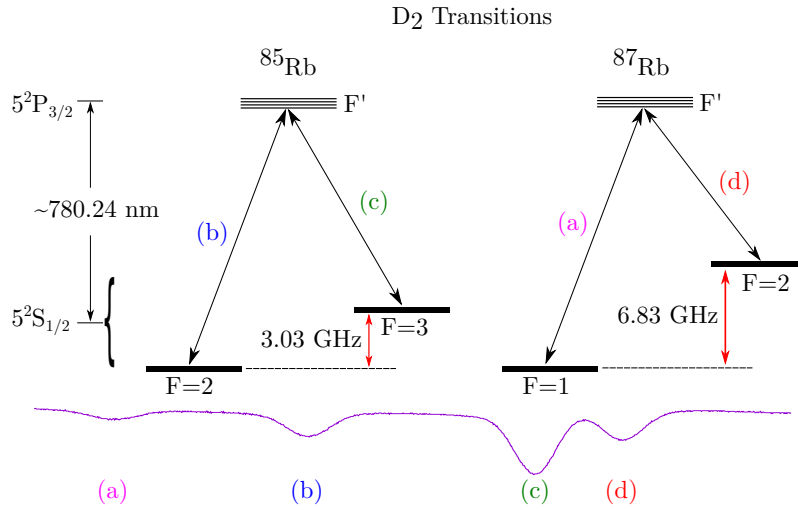


Figure 3.2: The D<sub>2</sub> levels of <sup>85</sup>Rb and <sup>87</sup>Rb in our cell at natural abundance ( $\approx 72\%$  and  $28\%$  of <sup>85</sup>Rb and <sup>87</sup>Rb respectively).

crossings [72]. The graph data is normalized to the maximum and minimum of the data. It is also apparent that no significant gain appears in this data. In addition, both of the two mixed polarization cases were considered, (linear pump, circular probe) and (circular pump, linear probe), and showed a similar response as figure 3.3 in terms of gain (and other effects).

When both the pump and probe are circularly polarized however, the situation is quite different. Figure 3.4 shows the results of the same scan, but with both pump and probe at the same circular polarization. Just like in figure 3.3, the graph data is normalized to the maximum and minimum of the data. Here we see many more processes happening that are not present above. The prominent feature however is the strong gain of the probe at the  $F = 2 \rightarrow F'$  transition when the pump is at the  $F = 3 \rightarrow F'$  transition in <sup>85</sup>Rb. This feature has gain on either side of the  $F = 2 \rightarrow F'$  transition with absorption in the middle. Since earth's magnetic field is adequate enough to cause Zeeman splitting of the hyperfine levels, it is believed that the role circular polarization plays is in optically pumping the atoms to

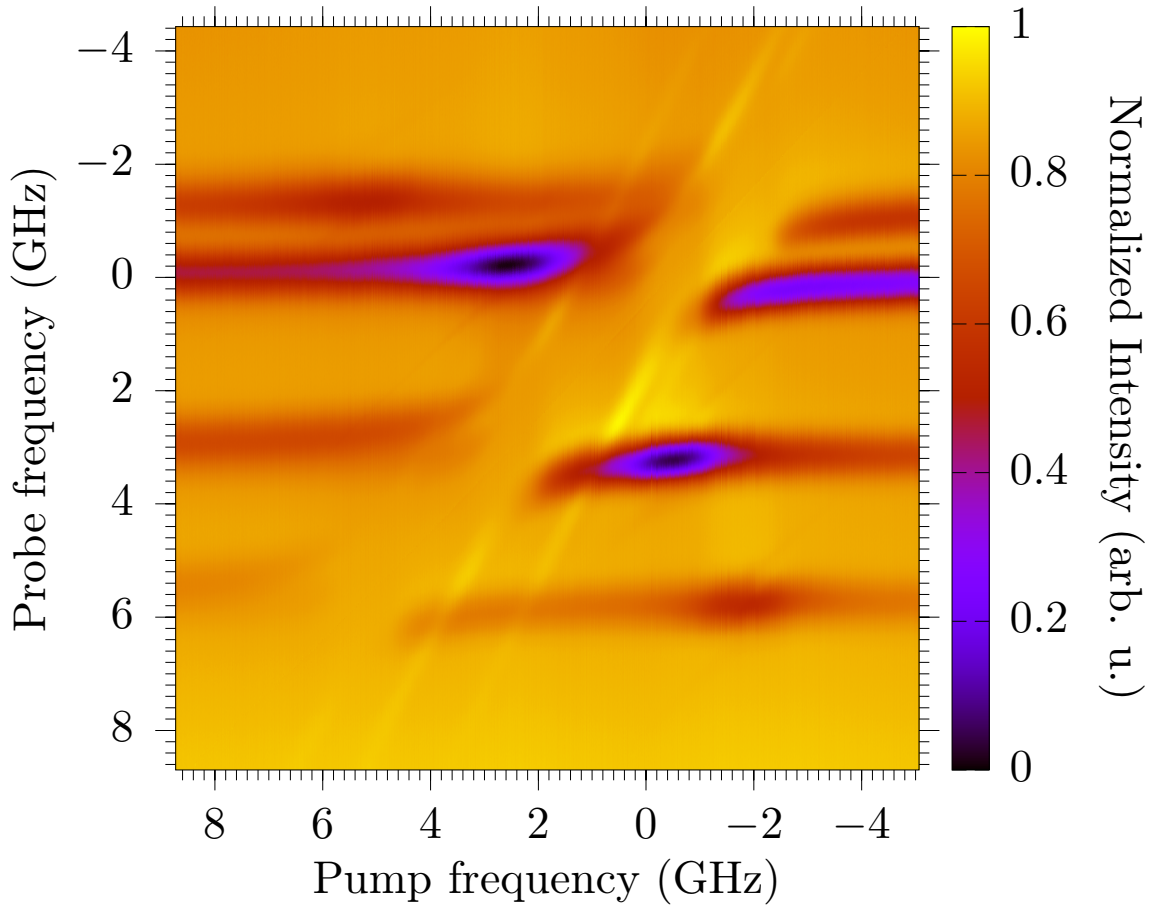


Figure 3.3: Scan of the pump and probe lasers over the  $^{85}\text{Rb}$  and  $^{87}\text{Rb}$   $D_2$  levels with both beams linearly polarized. The graph data is normalized to the maximum and minimum of the data.

the extrema angular momentum states, thus making the system closer to a true three-level system.

The maximum increase in voltage on the photodiode is 0.15 V. Since the balanced detectors maximum AC conversion gain at this wavelength is  $\approx 5 \times 10^5$  V/W, this gives a increase in the probe power of about  $0.3 \mu\text{W}$ . Therefore, the maximum gain achieved is about 0.12% gain.

Unlike the work of Wu for gain in 2 level systems, this was not performed with a molecular beam but in a warm Rb gas with appreciable Doppler broadening. In addition,



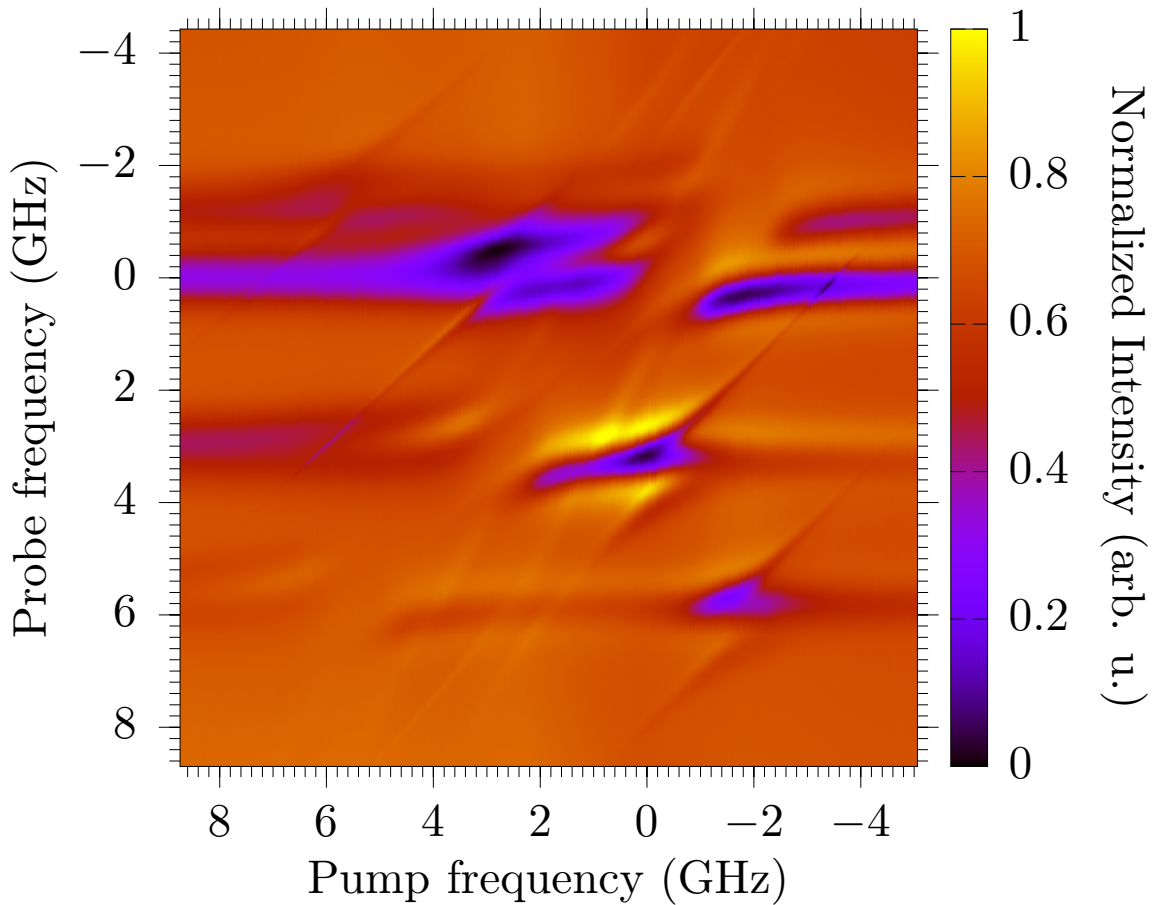


Figure 3.4: Scan of the pump and probe lasers over the  $^{85}\text{Rb}$  and  $^{87}\text{Rb}$   $\text{D}_2$  levels with both beams circularly polarized. The graph data is normalized to the maximum and minimum of the data. We see strong gain around the  $F = 2 \rightarrow F'$  transition when the pump is at the  $F = 3 \rightarrow F'$  transition in  $^{85}\text{Rb}$ .

this setup is significantly easier and cheaper to build and run than a molecular beam experiment. While 0.12% gain appears small at first glance, this is a significant increase when using common sensitive detection systems. Since this can be achieved in a Doppler broadened system, it is not limited to special, hard to achieve conditions. This shows promise for extending this method to molecules as a probing method with a resonant pump present.

## 4. IMPULSIVE STIMULATED BRILLOUIN SCATTERING MICROSCOPY\*

### 4.1 Introduction

Brillouin spectroscopy is an emerging tool in biomedical sensing and imaging [7, 73, 74]. Similar to Raman spectroscopy, which is providing chemical and structural information about interrogated molecules in the focal volume, Brillouin spectroscopy relies on inelastic light scattering. However, the contrast mechanism in Brillouin scattering is derived from acoustic (material) vibrations, thus providing a spectroscopic method to assess mechanical properties of materials [75, 8]. Biomedical applications of Brillouin spectroscopy were first suggested 40 years ago [76, 77], but the technical complexity of Brillouin scattering experiments and the lack of appropriate commercial instruments slowed down the penetration of Brillouin spectroscopy into the biomedical field. Recent advances of Brillouin spectroscopy based on the development of multichannel detection [78] made it possible to expand the applications of Brillouin spectroscopy to new areas [7, 79, 22, 80]. Unprecedented accuracy in determining the Brillouin shift [81] and the ability to combine Brillouin microscopy with other non-invasive optical imaging techniques, such as Raman spectroscopy/microscopy[56], prompted a further push to improve the speed of data acquisition towards attaining video rate imaging speed which can be on par with the state of the art nonlinear Raman imaging [82]. We have recently explored stimulated Brillouin scattering [83], which can also be used in a highly scattering biological environment [84]; however, the use of CW excitation substantially limits the efficiency of this nonlinear process. In this report, we explore an alternative approach based on impulsive stimulated Brillouin scattering (ISBS) [85, 86, 49, 87, 88] and demonstrate high speed microscopic

---

\*Portions of this chapter are reprinted with permission from “Impulsive Brillouin microscopy” by Ballmann, C W, Meng, Z, Traverso, A J, Scully, M O, Yakovlev, V V, 2017. *Optica*, 4, 124–128, Copyright 2017 Optical Society of America

imaging using this approach.

## 4.2 Conceptual Framework

Since the theoretical foundation [3] and experimental verification [4, 89, 90] of Brillouin scattering, many methods have been developed to extract the information that this type of scattering provides. Brillouin scattering can be probed in either one of two regimes, spontaneous or stimulated. Spontaneous Brillouin scattering is the scattering of light from acoustic fluctuations in materials. This scattered light is usually collected in the backward direction and is sent to a Fabry-Pérot or a dispersive etalon to measure the frequency shift (typically  $\sim$  GHz).

There are several drawbacks to using spontaneous Brillouin scattering however. The signal is typically weak and requires long ( $\sim$  1 second) acquisition times to obtain a high signal-to-noise spectrum. In addition, spontaneous Brillouin is plagued by a strong background from Rayleigh scattering that can saturate the detectors used and hide the weak Brillouin signal. Most of the problems mentioned above can be eliminated by resorting to a stimulated Brillouin scattering technique, such as ISBS.

ISBS was first discovered by Boersch and Eichler in 1967 [48]. It was immediately recognized as an important spectroscopic method for materials' characterization. Briefly, ISBS is a form of stimulated Brillouin scattering that generates acoustic waves by intersecting two focusing beams of light from a pump laser. Where these two beams intersect, they form an interference pattern of periodic field intensity (Figure 4.1(b)). This in turn induces a periodic grating in the index of refraction of the material that propagates in both directions at the speed of sound of the material. The sound waves generated are then probed by a probe laser and the signal is measured. The frequency of the sound waves are controlled by the intersection angle of the two pump beams. The frequency of this acoustic wave is given by [91]  $f_s = 2 \frac{v_M}{\lambda_{\text{pump}}} \sin(\Theta/2)$ , where  $v_M$  is the speed of sound of the ma-

material,  $\lambda_{\text{pump}}$  in the pump vacuum wavelength and  $\Theta$  is the angle between the intersecting beams measured from outside the material. The scattered probe is modulated at the acoustic frequency and is detected with a photodiode and collected by an oscilloscope. Unlike stimulated Brillouin scattering in backscattering or counterpropagating pump/probe configurations, ISBS allows one to use broad bandwidth, high intensity pump lasers without affecting the frequency resolution.

The methods and capabilities of ISBS have been improved over the years. One such improvement is the use of a phase mask (typically a transmission grating) to generate the grating [50, 51, 92, 93]. In this method, a transmission grating is used to split the copropagating pump and probe beams. Taking only the first order diffracted beams, they are then imaged onto the sample using a 4f lens configuration. This approach provides many benefits. First, it allows perfect phase matching without difficult alignment procedures and is a very robust system that could be implemented easily in any lab. Second, the frequency of the grating can be easily changed by using a grating with a different period. Third, it allows one to easily use optical heterodyne detection to increase the detected signal intensity.

Spontaneous Brillouin has been used for biological imaging applications at the cellular [7] and subcellular [24, 73] level. Stimulated Brillouin scattering has only recently been reported for imaging purposes [83]. While single-point acquisition time is dramatically reduced in stimulated Brillouin scattering, it takes a significant amount of time to collect the full Brillouin spectrum, which is necessary for an accurate assessment of viscoelastic properties. One of the ways to improve the data acquisition is to employ impulsive stimulated Brillouin scattering (ISBS), which allows simultaneous recording of the full spectrum.

In this report, we demonstrate the first two dimensional ISBS imaging. This work shows many improved aspects over SBS imaging. The use of a high intensity pulsed pump

laser generates a strong grating, which provides a deep modulation of the CW probe that is easily collected with a photodiode. Guided by our experimental data, we also evaluate the ways to improve detection sensitivity and lower acquisition times further to the point of single shot detection, which could potentially be used to perform Brillouin scattering video rate imaging.

### 4.3 Experimental Configuration

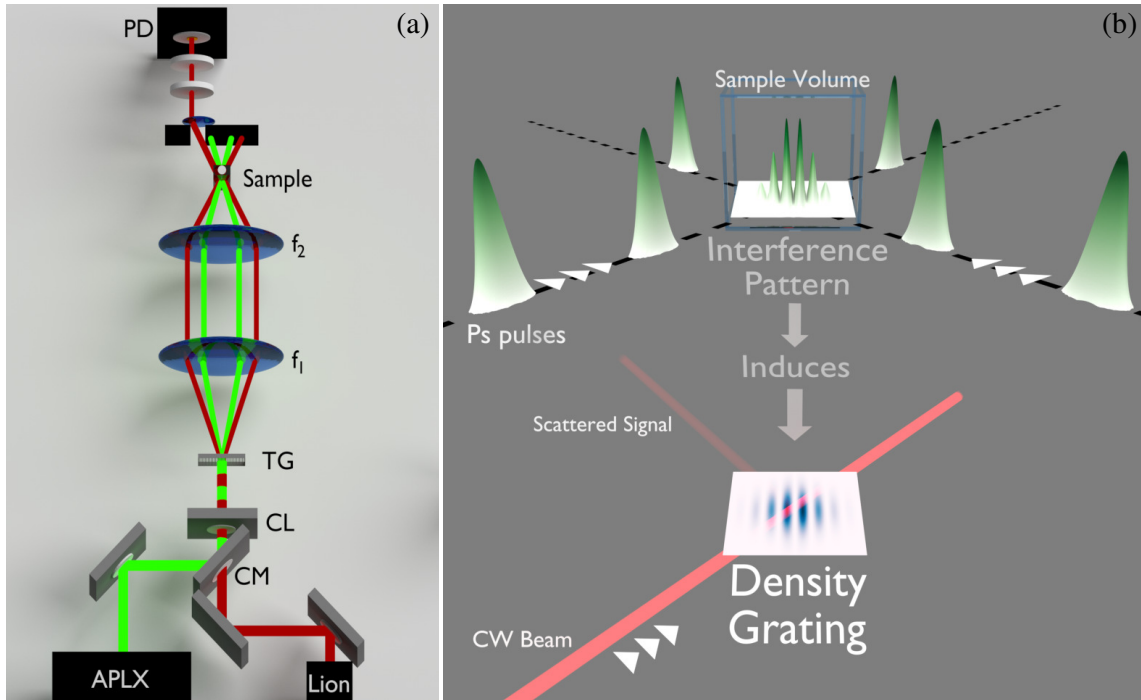


Figure 4.1: Conceptual picture illustrating ISBS. In (a), the pump beam (APLX, 6 ps) is combined with the probe laser (Lion, CW) using a cold mirror (CM) and focused with a cylindrical lens (CL) onto the transmission grating (TG). The grating is then reimaged with a 4f lens telescope ( $f_1$  &  $f_2$ ) into the sample and collected on a photodiode (PD). The ISBS process is shown conceptually in (b). The incoming pump pulses intersect and interfere in the medium. This intensity distribution induces a density grating, which may be both acoustic(propagating) and thermal(static). The blue waves illustrate the density variations in the material that make up the induced grating. The probe beam (red) scatters off this grating and is measured. The reference beam from the probe is not shown for clarity.

The experimental setup (shown in Figure 4.1(a)) consisted of a 532 nm, 6 picosecond pump laser (Attodyne, Inc.; APLX-1064-532) with  $\approx 100 \mu\text{J}$  per pulse at 10 KHz repetition rate, and a 780 nm, 100 mW CW diode laser (Sacher Lasertechnik; Lion TEC-520-0780-100-M) for the probe. The two beams were combined with a cold mirror (HT @ 780 nm, HR @ 532 nm) and were then focused (in the vertical direction) with a 20-cm focal length cylindrical lens onto a transmission grating ( $48 \mu\text{m}$  grating period) that serves as the phase mask. Only the first order modes were kept and allowed to pass through the 4f telescope system. The 4f telescope reimages the grating into the sample with a period proportional to the ratio of the 4f lens focal lengths (the first and second lens focal lengths were  $f_1=75 \text{ mm}$  and  $f_2=25.4 \text{ mm}$ ). The total pulse energy of the two intersecting pump beams was  $\approx 40 \mu\text{J}$  with a vertical width of about  $6 \mu\text{m}$  (this vertical focusing being a reimaging of the cylindrical lens focus at the grating). We use a heterodyne configuration [51] for the probe beam with the reference beam attenuated. Therefore, the signal and reference beams from the CW laser were 25 and 16 mW respectively.

The sample is mounted on an xy motor controlled stage system (Newport, Inc.; ESP300) and is moved after the data for that pixel has been collected. After the interaction in the sample, the signal and reference beam travel through another cold mirror to remove most of the pump light, and then pass through a 760 long-pass filter (IR-76; Edmund Optics, Inc.) with a 532 notch filter which are mounted to the photodiode (Thorlabs; DET10A) to remove any remaining 532 from the beam. The signal from the photodiode is then amplified 625 times using a 350 MHz preamplifier (Stanford Research Systems; Model SR445A). A dc block is used on one of the inputs to remove the dc bias from the photodiode. The signal is then collected using an oscilloscope (Agilent Technologies; DSO6034A, 300 MHz). The oscilloscope is triggered from another photodiode close to the laser output. The signal was extracted from the oscilloscope by a computer. The stage system and oscilloscope are controlled by a custom written code in NI LabVIEW™.

#### 4.4 Experimental Results

Figure 4.2(a) shows a zoomed in region of an example signal (512 averages) collected by the oscilloscope from the photodiode (after amplification). Each pixel in the scan has a trace that is recorded and is later processed to make the image. An FFT is taken of each trace (Figure 4.2(b)) and fitted to find the center frequency. The frequency resolution is on the order of a megahertz with a SNR of about 8. All these frequencies are collected in a matrix that, when plotted, gives an image of the frequency shifts in the sample.

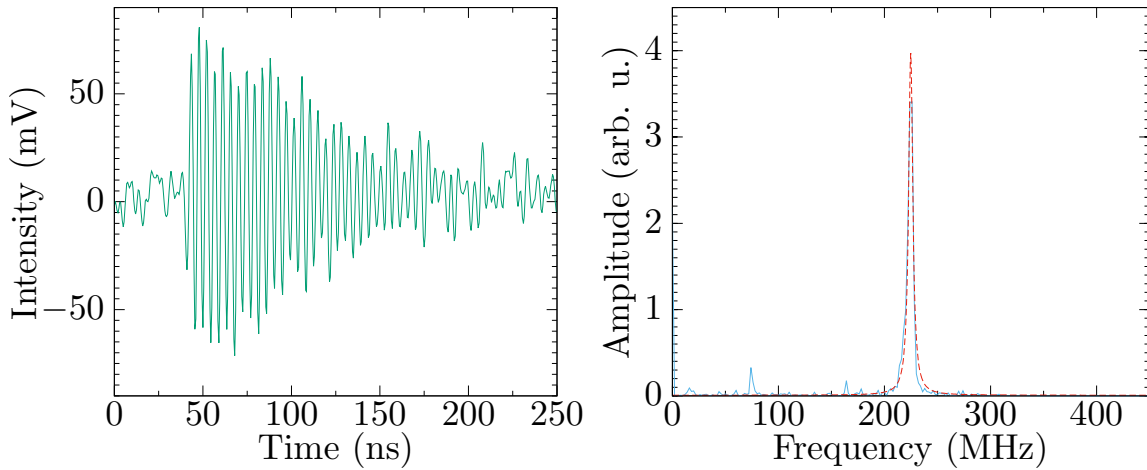


Figure 4.2: (a) A typical ISBS signal (512 averages) from a saturated brine solution ( $\sim 26\%$  NaCl at  $\sim 20^\circ\text{C}$ ) with (b) a corresponding Fourier transform. The dashed red curve in (b) shows a Lorentzian fit to the data.

As a test of our imaging setup, we used a window type cell where four subcells are connected together to form a window. Each of the four subcells were filled with different liquids. The subcells were about  $1\text{ cm}^3$ , however only a limited region at the intersection of the four cells was imaged. The resulting image is shown in Figure 4.3, where the modulation frequencies are shown on the color bar. In this scan, 512 averages per shot were taken per pixel ( $10^{-4}\text{ s}$  acquisition time per sample) and the image took about 40 minutes

to obtain with a  $250 \mu\text{m}$  step size in each dimension ( $65 \times 65$  pixel grid). Starting from the top right (yellow region) and going clockwise, the four liquids were saturated brine solution ( $\sim 26\%$  NaCl at  $\sim 20 \text{ }^\circ\text{C}$ ), plain tap water (which was chlorinated), Isopropyl alcohol (91% concentration in water) and Methanol. The black region in the center is where the cell walls are which block the beam entirely. For the focal length lenses used, the frequencies from the gratings generated in these liquids agrees very well with theory given in Ref. [86].

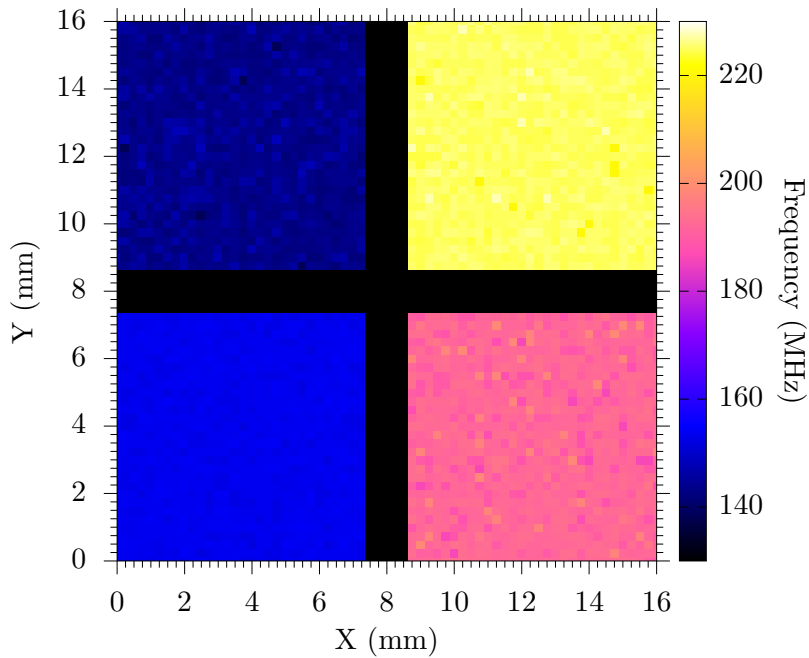


Figure 4.3: ISBS image of four liquids in a window cell. The liquids are (starting from top right and going clockwise) Brine ( $\sim 26\%$  NaCl), tap Water, Isopropyl Alcohol (91%) and Methanol.

To show a proof-of-principle of the efficacy of this method towards microscopy, we made use of a Y microchannel cell (Translume; YNZF-300500-L16-500500500) by imaging a close-up region at the intersection of the channels using  $50 \mu\text{m}$  step sizes. The cell



channels are  $300\ \mu\text{m}$  wide by  $500\ \mu\text{m}$  deep and were filled with tap water. The resulting image is shown in Figure 4.4 ( $81 \times 51$  pixel grid) using 1024 averages per pixel and took about 30 minutes to obtain. The water signal from the channels is seen in magenta. The signal from glass, which is everywhere outside the channels, is too high for our detector system, leaving just noise there. In the signal processing, we set an amplitude threshold for the signal, which if it goes into the noise, we set it equal to zero. At the intersection of the channels, there is a microjet that blocks the signal, hence why it is black as well. However, in the upper middle channel, a small amount of air (at  $X = 2\ \text{mm}$  and  $Y \simeq 1.3$  to  $1.8\ \text{mm}$ ) was left in the channel separating the water from the intersection. There is no signal here, which shows that the signal is coming from the water and not from a simple geometric scattering process. It should be noted that our setup is currently arranged only for measurements in transmission geometry. However, for thin samples we can measure the modulated backward reflection from surface acoustic waves on the sample and for thick, highly scattering samples, we expect the signal to be partially backscattered to the detector. These configurations add further flexibility in the use of ISBS in biology.

#### **4.5 Discussion**

These examples demonstrate the two dimensional imaging capability of the system. However, in order to translate those results to biological imaging, one has to achieve cellular level resolution and higher imaging speed to assess biological processes in living cells and tissues. Thus, the resolution and acquisition times can be substantially improved upon. The data acquisition process can be sped up by using a higher laser repetition rate and by improving the detection sensitivity of the system. With enough sensitivity, averages would not be necessary and single shot signal detection is possible. Another improvement would be to use a linear detector array so that a line on the sample could be analyzed simultaneously. Our current setup used a single non-amplified silicon photodiode. An example of an

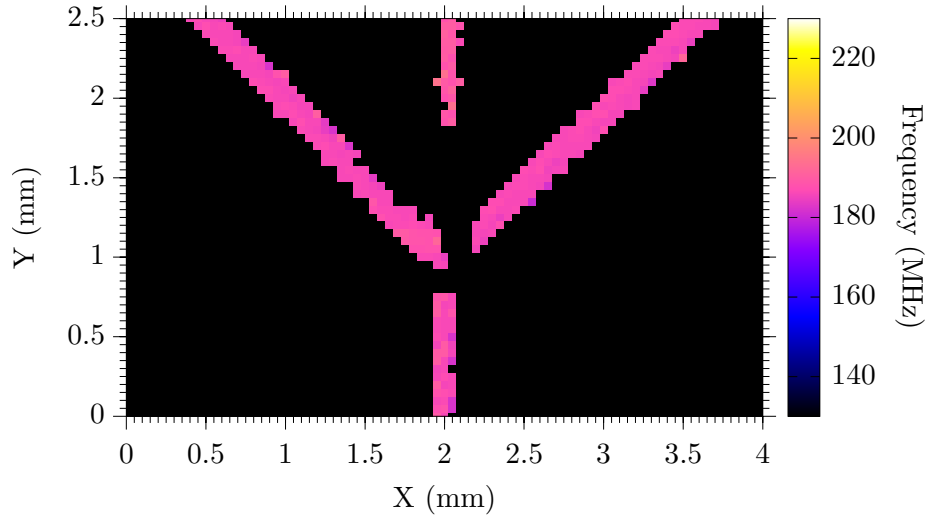


Figure 4.4: ISBS image of tap water in a Y microchannel cell. The upper middle channel contains a small amount of air, showing that this signal is coming from the water and not geometric scattering. The black outside the channels has a glass signal that is too high for our detection system.

improved detection system would be a linear photomultiplier tube array that is input into a multichannel digitizer. In addition, most of the time it took to perform our scan was from the xy stages themselves. For a practical experiment, using galvo mirrors or acousto-optic beam steering along with a scan lens to scan with the light and not move the sample would speed up the mechanical scanning rate several orders of magnitude. The resolution can be further improved simply by using shorter focal length objective lenses to image a grating with a smaller period into the sample. In our present setup, the spatial resolution is limited by the horizontal width of the probe beam at the focus, which is around  $200 \mu\text{m}$ . However, the probe only need scatter off of  $\geq 1$  acoustic periods for efficient diffraction [94]. Therefore, with a tighter probe focus, our spatial resolution would be limited by the distance of about 1 acoustic wavelength, which is around  $8 \mu\text{m}$  in water. As a future improvement, taking water as an example, an acoustic wave around 1 GHz will give sufficient diffraction to obtain a spatial resolution of nearly  $1 \mu\text{m}$ . This requires having a detection system that

has enough bandwidth ( $\sim$  GHz) for this signal. With the above mentioned improvements, assuming  $\simeq 500$  kHz laser rep rate with  $\simeq 1 \mu\text{J}$  pulse energy and single shot detection, video rate imaging over a  $800 \times 640$  image should be possible.

## 5. STATISTICAL COMPARISON OF SPONTANEOUS AND STIMULATED BRILLOUIN SCATTERING

### 5.1 Introduction

Spontaneous Brillouin scattering has been used over the years for many biological and material science purposes and is becoming an increasingly important spectroscopic technique. Brillouin scattering is a non-elastic scattering of light off of acoustic waves that are a result of thermodynamic fluctuations. Since the Brillouin shift is determined by several properties of the material such as the speed of sound, elasticity, etc., it provides a measure of these properties that are difficult to obtain otherwise. This is of particular interest for samples that are small and/or fragile, and has been successfully applied to materials such as spider silks [8], DNA [95, 75], viruses [27] and thin films [9, 17]. In recent experiments, it has shown much promise for use in biological spectroscopy [28, 29, 30, 31, 32] and microscopy [60, 7, 56].

Stimulated Brillouin scattering (SBS) has only recently been applied to microscopy [83] and has much potential. However, problems with the experimental realization of SBS, such as acquisition time and counterpropagating beam alignment at the focal region have made such methods difficult to use. One approach is the use of impulsive stimulated Brillouin scattering [96, 97, 98] to overcome these shortcomings [93]. ISBS is implemented by first generating a transient density grating in a material by intersecting two beams of high intensity laser pulses in the material. This grating is then probed by a weaker pulsed or CW laser by Bragg scattering off of the grating. Since this grating is moving, it will modulate the probe beam which is detected with a photodiode.

Data collection for ISBS is very fast compared with the above imaging methods. Also, unlike counterpropagating stimulated Brillouin scattering, ISBS allows one to use broad

bandwidth, high intensity lasers for the pump without affecting the frequency resolution. In this case the frequency resolution depends on things such as phonon lifetime, beam geometry at the focus and collection time length. Since broadband lasers can be used, we can take advantage of the high intensities from these type laser sources to obtain orders of magnitude higher signal than in the CW case. This signal frequency is also controlled by the pump laser overlap angle, which can be controlled. Overall, this enables us to obtain spectra much faster with a stronger signal.

Both SpBS and ISBS are important techniques and have a proper place in material and biological spectroscopy and microscopy. However, it would be of interest to have a comparison between the two techniques in order to determine which method is most appropriate for the task at hand. It is the goal of this work to provide such a comparison. We give a brief overview of the experimental configurations used, and then present the data, and in particular, statistics of the data to determine optimal samples needed for minimum uncertainty. We then compare both SpBS and ISBS, as well as nanosecond versus picosecond ISBS, in the discussion section and give strengths and weaknesses for both.

## 5.2 Experimental Configuration

The simplified experimental setups for ISBS and SpBS are shown in Figure 5.1 and Figure 5.2. For ISBS (Fig. 5.1), only the pump laser is changed between the two setups. The probe was a diode laser (Newport, Inc.; Vortex II TLB-6900) with 45 mW total power at 780 nm. The pump laser used for nanosecond data was a 532 nm, 1 ns fiber laser (IPG Photonics, Corp.; GLPR-10) with  $\sim 5 \mu\text{J}$  pulse energy at the sample at 100 kHz, and for the picosecond data we used a 532 nm, 6 ps hybrid fiber/free space amplified laser (Attodyne, Inc.; APLX-1064-532) with the power attenuated to give  $\sim 5 \mu\text{J}$  at the sample at 100 kHz. The pump and probe beams are combined with a cold mirror and focused on the transmission grating (48  $\mu\text{m}$  grating period) in the vertical direction using

a cylindrical lens (20 cm focal length). Using a 4f lens system ( $f_1$  and  $f_2$  are 75 and 25.4 mm, respectively), the grating is then re-imaged into the sample. After the sample, everything but the signal is blocked by a slit.

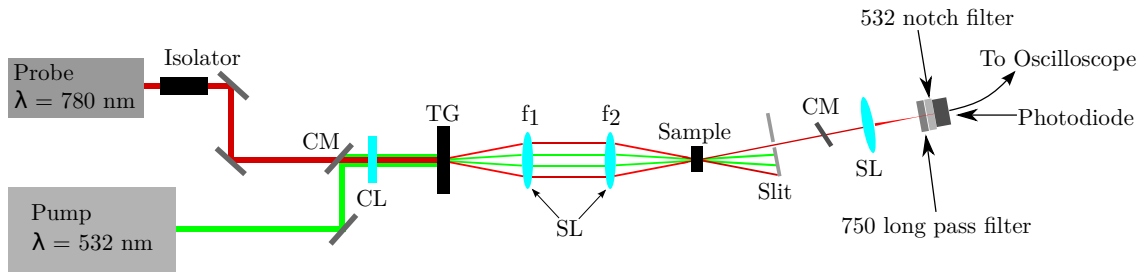


Figure 5.1: Simplified schematic of the ISBS setup. The two beams are loosely focused on a transmission grating (TG) and re-imaged on the sample. The signal is then optically filtered and sent to the photodiode. CL - Cylindrical Lens, SL - Spherical Lens, CM - Cold mirror (all other unmarked mirrors are dielectric)

A cold mirror blocks most of the stray 532 nm beam coming through, however a 750 longpass filter in conjunction with a 532 notch filter are used to further remove any remaining pump light. The signal is focused onto a photodiode (Thorlabs; DET10A) which is connected to a 350 MHz preamplifier (Stanford Research Systems; Model SR445A) and then sent to an oscilloscope (Agilent Technologies; DSO6034A, 300 MHz) for data collection. The oscilloscope is triggered from another photodiode at the pump output. The data is collected on a computer from the oscilloscope using a custom NI LabVIEW™ code.

Figure 5.2 shows a simplified schematic of our SpBS setup that starts with a diode seed laser (Pure Photonics, LLC; PPCL300) with center wavelength around 1560.48 nm which is input into a fiber amplifier (IPG Photonics, Corp.; EAR-5K-C-LP-SF). The output of the amplifier is passed through a second harmonic crystal (Covesion, Ltd.; MgO:PPLN, MSHG1550-1.0-20) where the output is now at the  $D_2$  resonance in Rb ( $\simeq 780.24$  nm).

The beam is reflected by a polarization cube and then passes through a  $\lambda/4$  waveplate before it is then focused on the sample. The signal light then passes through the  $\lambda/4$  waveplate and now passes through the polarization cube. This allows collection of all the backscattered light versus using a conventional beam splitter. The Rayleigh scattered light is then filtered from the signal beam by double passing it through a warm Rb cell ( $\sim 60 - 70$  °C). The signal is then focused into a VIPA and the far field image is collected with a CCD (Andor Technology, Ltd.; Neo 5.5 sCMOS).

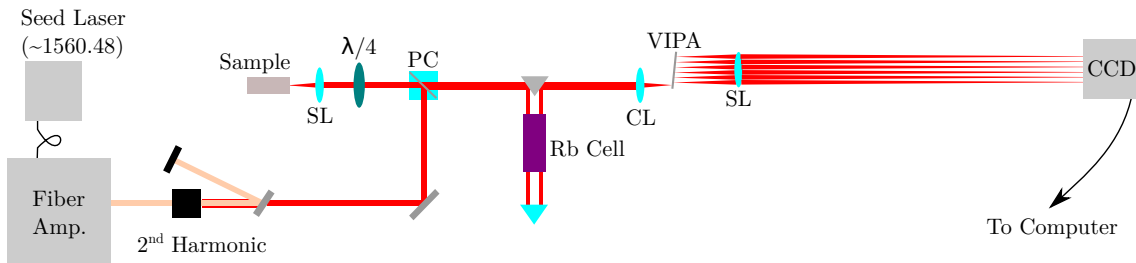


Figure 5.2: Simplified schematic of the SpBS setup. After the interaction the spontaneous Rayleigh scattered light is filtered with a Rb cell. The beam is then focused into a VIPA where it is dispersed. The far field image is collected with a CCD and then analyzed. SL - Spherical Lens, CL - Cylindrical Lens, PC - Polarization Cube

### 5.3 Experimental Results

In the following, we present the data for ISBS and SpBS and discuss various implications of the data.

#### 5.3.1 Impulsive Stimulated Brillouin Scattering Data

Figure 5.3 shows oscilloscope traces of signal from distilled water, methanol, and acetone for both nanosecond and picosecond data. Each plot is an average of  $10^5$  traces from the oscilloscope. This data was taken with a 10 cm cylindrical lens to focus onto the grating in the vertical direction (see figure 5.1). When the beams re-image the grating

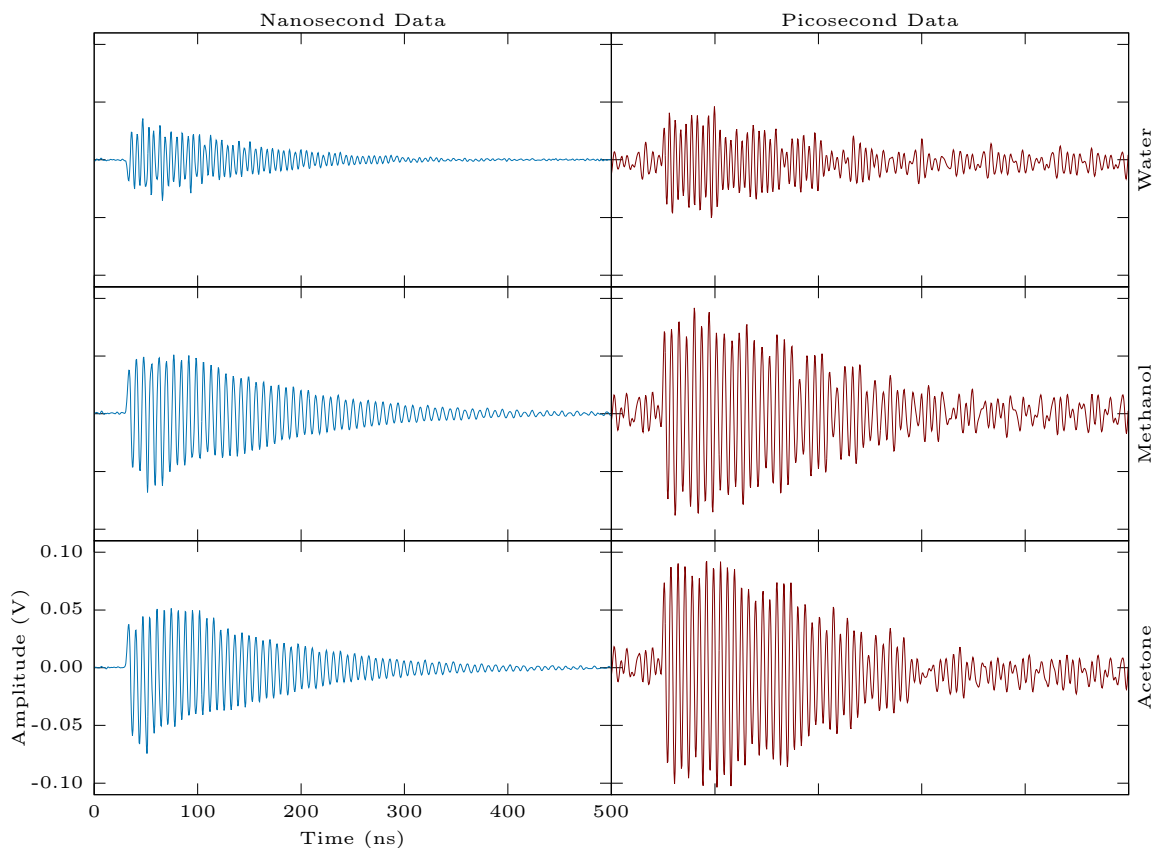


Figure 5.3: ISBS signals from an average of  $10^5$  oscilloscope traces for each liquid. The cylindrical lens used to focus onto the transmission grating was 10 cm.

into the sample, they will also focus cylindrically again with a magnification given by the  $4f$  system. Therefore, the focal length of the cylindrical lens will determine the vertical thickness of our sound generation region. Shortening the focal length of the cylindrical lens increases the intensity of the field and results in a larger amplitude sound wave generated. However, the sound wave will now diffract much faster as it propagates. Figure 5.4 shows the same results as figure 5.3 but with a 20 cm cylindrical lens.

We notice several things immediately. For the nanosecond case, the intensities are lower, but the oscillations last far longer than with a 10 cm lens. For the picosecond case, the intensities are greater, but there is little change in the lifetime of the observed



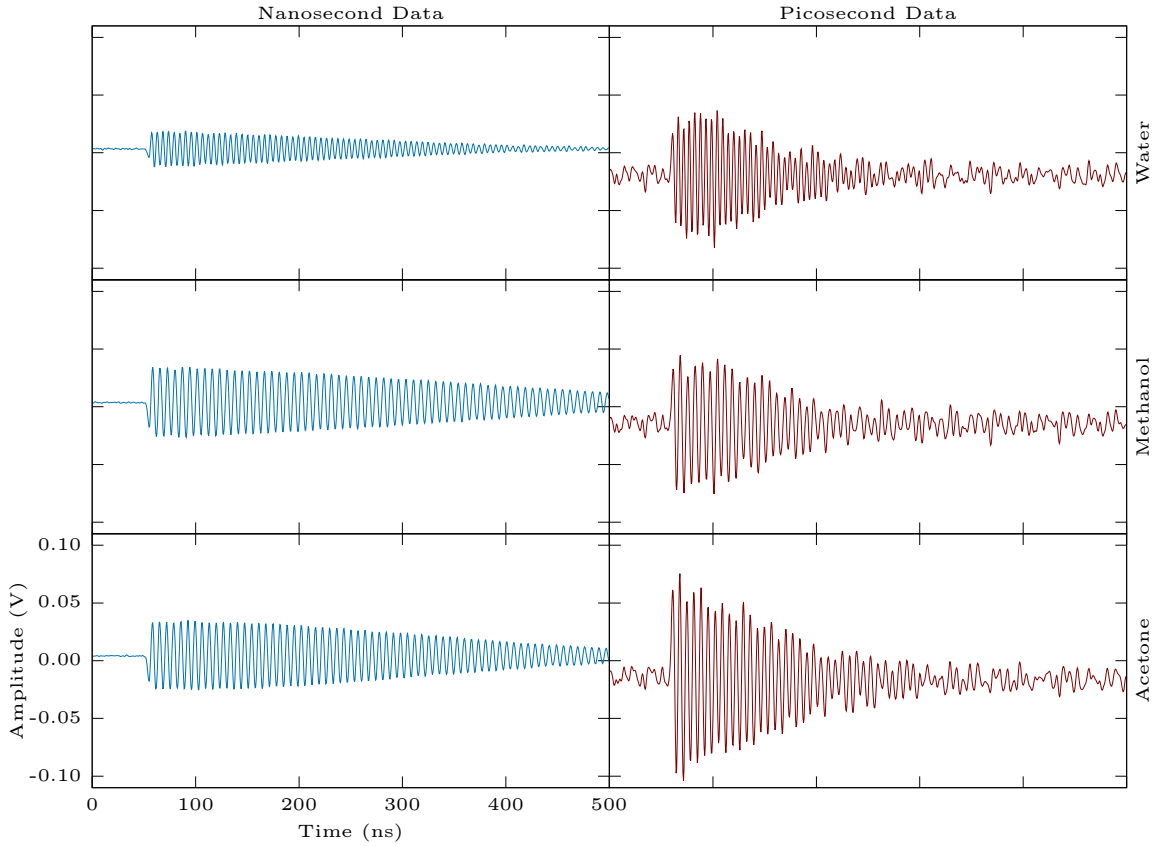


Figure 5.4: ISBS signals from an average of  $10^5$  oscilloscope traces for each liquid. The cylindrical lens used to focus onto the transmission grating was 20 cm.

wave. The discrepancy between the change in signal lifetime for the nanosecond and picosecond cases is a result of the two beams being different beam diameters from the lasers ( $D_{nano} = 2.3$  mm and  $D_{pico} = 0.7$  mm FWHM).

To investigate whether diffraction is the main source of these differences, we considered the following model. Let us consider each point on the sound waves that are being generated in the flat focal region in the experiment to be similar to plane waves of the same frequency diffracting through a single slit. The slit width is the same as the vertical excitation thickness at the focus in the sample, which is governed by the cylindrical lens. The results of this model are plotted in figure 5.5. We used the same parameters as in both

experiments for the slit width, sound wavelength and beam diameter. Figure 5.5 (a) and (b) shows the results for the nanosecond laser with the focal lengths of the cylindrical lens being 20 and 10 cm, respectively, while (c) and (d) show the results for the picosecond laser with the focal lengths being 20 and 10 cm, respectively. We see that the sound wave from the nanosecond beam diffracts substantially more with 10 cm vs 20 cm focal length. As noted above, the picosecond beam has a much smaller diameter than the nanosecond, therefore since it is not focusing as tightly, going from 20 to 10 cm does not cause such a significant increase in diffraction. In our experiment, we chose the 10 cm length lens for two reasons, higher intensity and higher resolution, the latter reason being of interest for microscopy. In passing, we note that considering the effects of diffraction of the sound waves and choosing lens focal lengths to minimize this is of utmost importance in ISBS studies of phonon lifetimes.

It is clearly seen that our picosecond data is more noisy than our nanosecond data. This noise, which is electrical and not optical, was traced to a noisy electrical ground in the lab. Let us consider the amplitude differences between the two pulse lengths. Assuming a rectangular geometry at the focus, the peak intensity of the nanosecond and picosecond beams was  $I_{nano,f} = 6.7 \times 10^7 \text{ W/cm}^2$  and  $I_{pico,f} = 1.1 \times 10^{10} \text{ W/cm}^2$ . Now the ratio between them is  $\frac{I_{pico,f}}{I_{nano,f}} \simeq 166$ , but in figure 5.3 we see that the signal from the picosecond is only about a factor of two greater than the nanosecond data. The reason for this is the result of the dynamics of transient SBS in general [99]. It has been shown [99, Ch. 2] that the threshold for SBS increases as the pulse length shortens. Therefore, as the pump pulse temporal width decreases, more intensity is needed to achieve the same reflectivity (from the generated Brillouin grating) as from pump pulses with longer duration. Using equations from [99] and assuming the pulses are rectangular pulses, we can plot the SBS threshold as a function of pulse length and is given in figure 5.6.

The green and blue dots mark the thresholds for pulses of length 6 ps and 1 ns, respect-

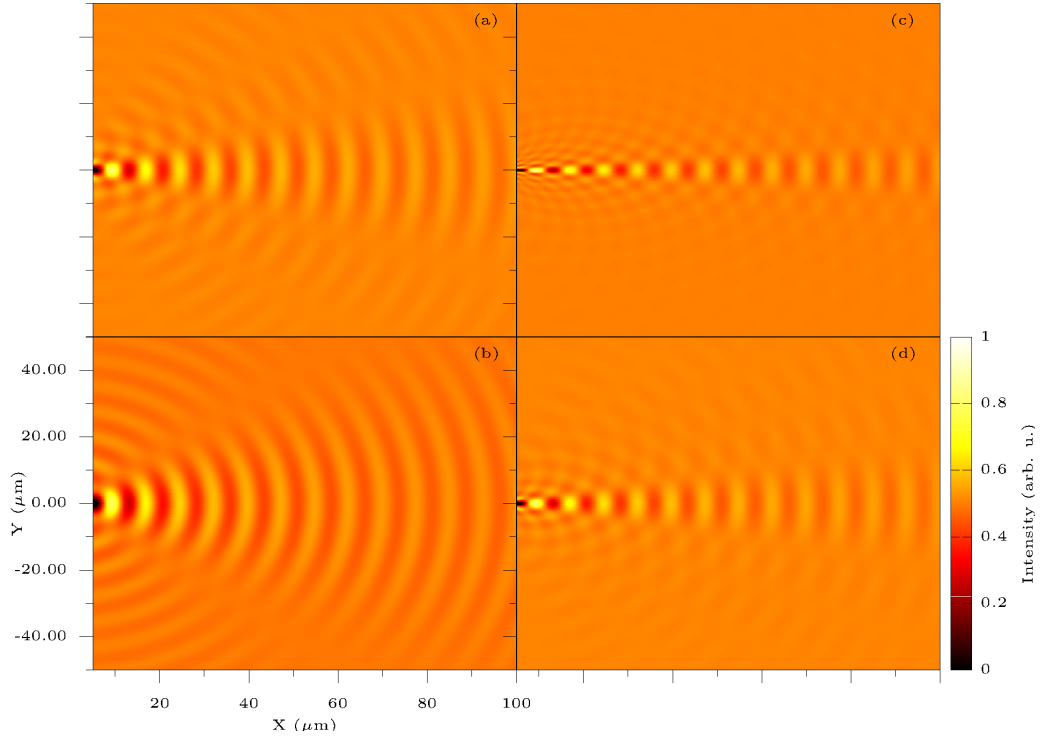


Figure 5.5: Simulations of sound waves diffracting through a single slit. (a) and (b) show the diffraction of sound waves generated from our nanosecond pulses using 20 and 10 cm cylindrical lenses, respectively. (c) and (d) show the diffraction of sound waves generated from our picosecond pulses using 20 and 10 cm cylindrical lenses, respectively. The difference in diffraction between nanosecond and picosecond beams is due to the fact that the nanosecond beam has a larger diameter, therefore it focuses down smaller.

fully. We see that there is a substantial increase of intensity needed to reach threshold for the picosecond beam as compared to nanosecond beam. The ratio of the picosecond to nanosecond threshold intensities is  $\frac{I_{\text{pico,Th}}}{I_{\text{nano,Th}}} \simeq 160$ . Now, in our experiment, we are above threshold for both beams. Once the intensity is above threshold and getting closer to saturation, the smaller the effect of a percent increase in the beam intensity. Comparing the two ratios above, we see that the intensity from the picosecond pulses in our experiment should only achieve a signal that is only slightly better than the nanosecond pulses.

To determine the frequencies, we take the Fourier transform of the time data and use a

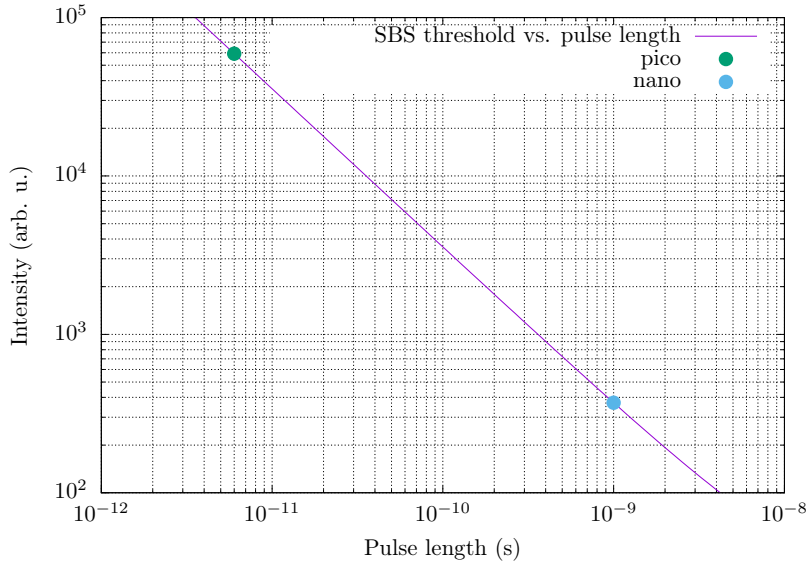


Figure 5.6: The threshold for SBS as a function of pulse length. As pulses get short, the intensity needed to reach threshold quickly rises.

custom written computer code to isolate the frequency peak in the frequency domain. For groups of data, we average the group before taking the Fourier transform. Once we have determined the frequencies, we perform our statistical analysis. Figures 5.7, 5.8 and 5.9 are plots of the Allan variance [54] for acetone, methanol and water as a function of the number of samples. The Allan variance gives a measure of the variance with respect to time, or number of samples (assuming the samples are taken periodically), and shows the influences of both short term and long term noise. The Allan 2-sample variance is given by

$$\sigma_y^2(\tau) = \frac{1}{2} \langle (\bar{y}_{n+1} - \bar{y}_n)^2 \rangle, \quad (5.1)$$

where  $\tau$  is the observation period and  $\bar{y}_i$  is the  $n$ 'th averaged data block over the observation time  $\tau$ . The minimum value of these plots gives us the optimum number of samples needed to reach the minimum uncertainty. For example, we see that as the pump power is increased (and hence the signal strength is increased), a lower uncertainty is reached

and it is reached with fewer samples. Each figure gives a side-by-side comparison of the nanosecond and picosecond results at multiple pump power levels. The nanosecond pump laser does not provide as much power as the picosecond laser we used, hence why the picosecond graph has a higher power data set. It should also be noted that anomalies in the data, such as the 180 and 220 mW cases for picosecond methanol data, are caused by unknown experimental errors for those data sets and are not physical processes. All graphs start out at a very high uncertainty ( $\sigma \simeq \sqrt{10^{15}} \simeq 10^{7.5}$  Hz), which is the uncertainty of various frequency components in the noise. This results from the fact that with low sample numbers and at low powers, the signal-to-noise is too low to determine the frequency. After a certain number of averages, the signal starts to rise out of the noise and causes a quick drop in the variance graphs. Now our oscilloscope time window was 500 ns, therefore our minimum frequency accuracy is 2 MHz. We see that after we have enough averages to determine the frequency, our uncertainty is already better than our accuracy. It was observed that while the uncertainty of acetone and methanol with a 1 Watt picosecond pump is still high with just one sample, the signal strength was sufficient to determine the frequency with one shot.

These figures give an estimate of how many pulses need to be averaged in our setup to confidently determine the frequency of the sample. At low sample numbers, the frequency of ISBS is in the noise and cannot be determined without special filtering, which would require the knowledge of the frequency before it was obtained. After a certain number of averages however, the signal rises above the noise and has converged close to its final value. As an example, acetone reaches the lowest uncertainty at about  $1 - 3 \times 10^4$  samples. Acquiring more samples will only degrade the signal further. We see this is the case for most of the higher power data sets.

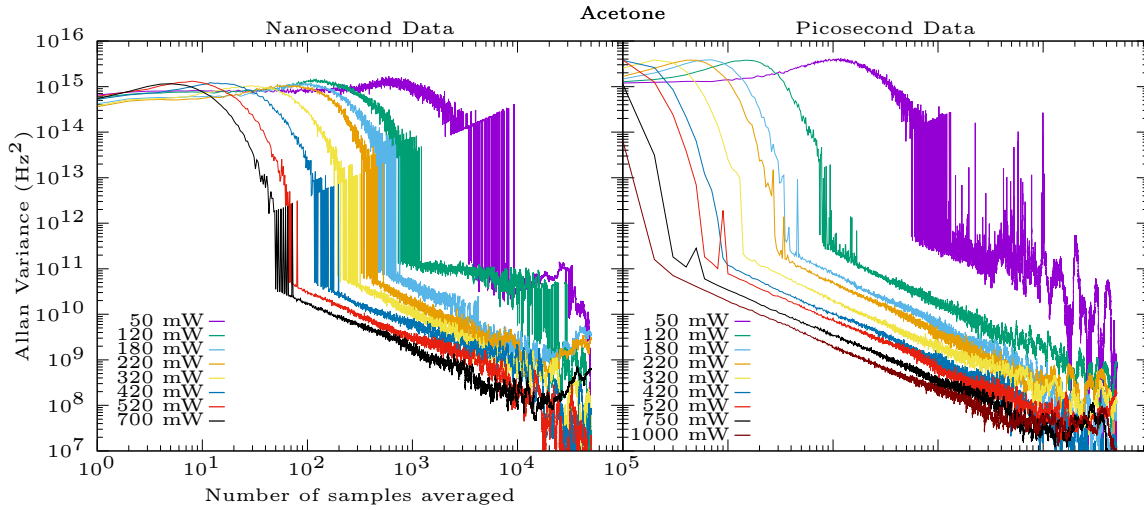


Figure 5.7: The Allan variances of the ISBS signal of acetone versus the number of samples taken.

### 5.3.2 Spontaneous Brillouin Data

Figure 5.10 shows an example spontaneous Brillouin spectrum for both acetone and methanol with 60 mW input power. This spectrum is produced by a full vertical binning of the CCD camera with 0.5 s integration time. The distance between the Stokes (or anti-Stokes) peak to the next Stokes (or anti-Stokes) peak is the free spectral range (FSR) of the VIPA. By taking the distance all of these FSRs in the array and using nonlinear fitting, we obtain a function to accurately ( $\sim$  MHz) determine the Brillouin shift. One immediate observation that can be made in comparing to our ISBS measurements above is that even a single measurement provides a signal-to-noise sufficient to measure the shift with only one measurement.

The Allan variances of the SpBS data are shown in Figure 5.11. As noted earlier, since we are able to determine the frequency with just one data sample, there is no fast drop in the variance as the signal rises above the noise like in the ISBS data. As expected, when the signal increases, the number of samples required to reach minimum uncertainty decreases.

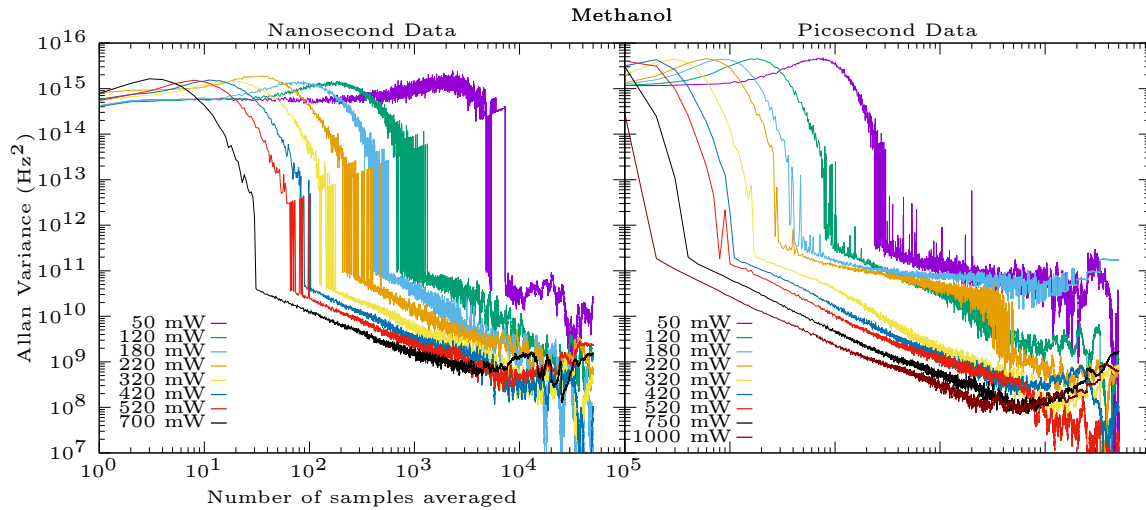


Figure 5.8: The Allan variances of the ISBS signal of methanol verses the number of samples taken.

It is also evident that fewer samples are needed to reach the minimum compared to ISBS. For the worst case, after about 100 samples our signal starts to degrade.

#### 5.4 Discussion

We will now compare between SpBS and ISBS. First, we should consider the time it takes to obtain the best data. It was already noted earlier that our SpBS integration time is 0.5 s, however it takes  $\simeq 0.9$  s per data point, since the computer has to process and save the data, and other time delays such as delay from the experiment control code. Therefore, for the best case scenario for SpBS (which is acetone at 60 mW) it takes about 25 samples for minimum uncertainty, which results in  $25 \times 0.9 = 22.5$  s. In contrast, ISBS worst case scenario is water at 50 mW pump power, which takes around 40,000 samples. However, each spectrum can be taken in  $10 \mu\text{s}$ , which results in  $4 \times 10^4 \times 10^{-5} = 0.4$  s total time. This shows quite an improvement over SpBS.

Next, consider the measured ISBS frequencies at the minimum uncertainty point in the data for each liquid at all power levels. This is provided in Figure 5.12. We see that the

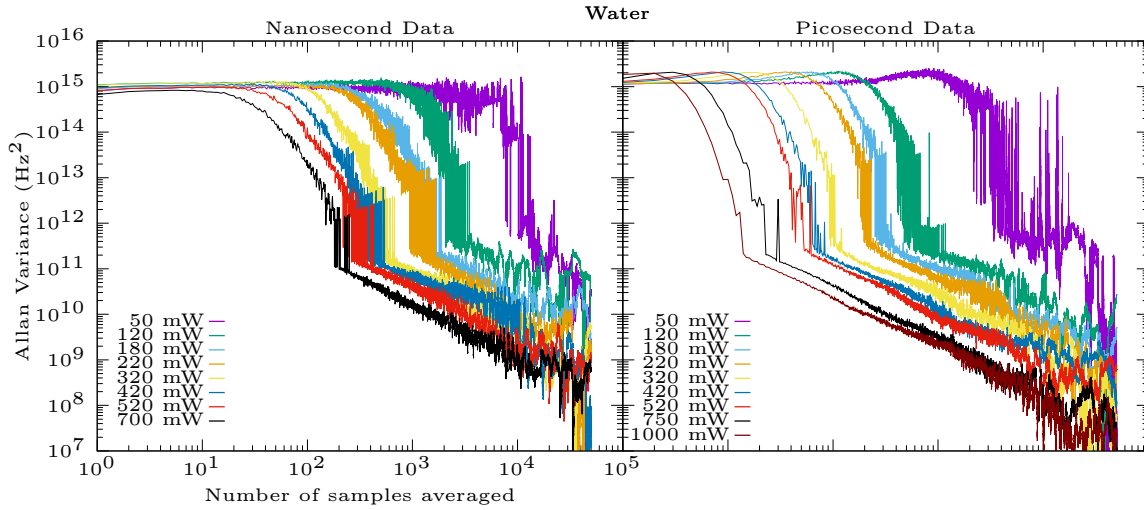


Figure 5.9: The Allan variances of the ISBS signal of water verses the number of samples taken.

measurement yields very close to the same result regardless of the pump power used.

Contrast that to the SpBS data in Figure 5.13. The signal appears to change more compared to ISBS, but note that we are measuring a higher frequency as well. In this case the signal is  $\sim$  GHz, therefore the best case signal difference is 14 MHz, which gives  $14 \text{ MHz}/3.78 \text{ GHz} \times 100 = 0.37\%$  error. For ISBS, worst case is 1.36 MHz, which gives  $1.36 \text{ MHz}/137.4 \text{ MHz} \times 100 = 0.98\%$  error. The best case for ISBS 0.096% (for water with ps pulses), but the average for all is 0.45%. Therefore, the reliability of the results for measurements taken at different power levels is nearly the same for both methods.

The strength of the ISBS signal for the lowest pump power is  $\sim 10 \text{ nW}$ . For SpBS however, even at 60 mW, the backward signal is at most  $\sim 100 \text{ pW}$ . In principle, with this stronger signal, we should expect faster data acquisition. However, it is noteworthy that with such a weak beam from SpBS, we still achieve good accuracy in a reasonable amount of time. One important comparison is that of frequency stability. In SpBS, the shift is a function of the input frequency. Therefore, laser drift is another source of noise



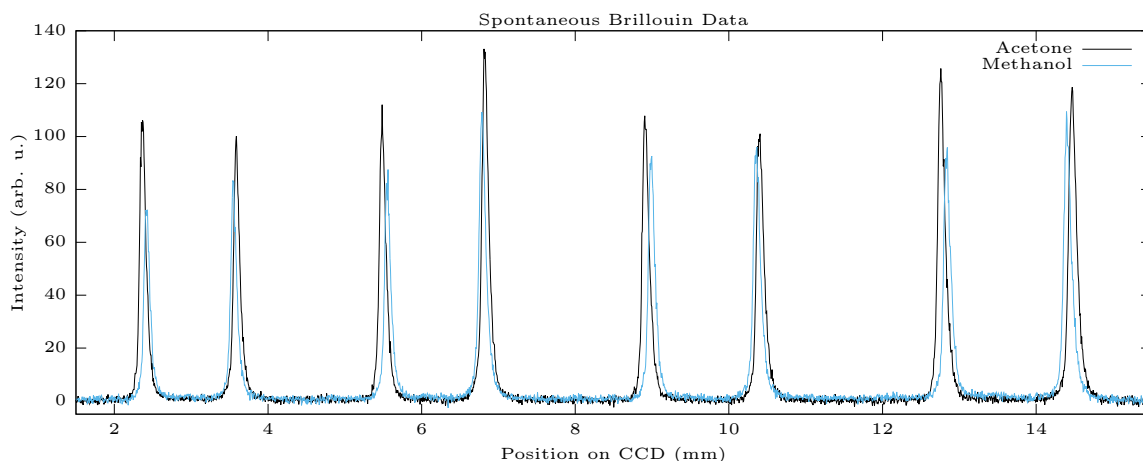


Figure 5.10: SpBS signals of acetone and methanol with 60 mW input power on sample.

for SpBS. For ISBS with a phase mask (such as used in this work), the measured frequency is independent of the frequency of the pump or probe.

One of the most important reasons for using SpBS over ISBS is the fact that SpBS is easily implemented in a backscattering geometry. This is of great importance for biological samples that are not transparent. ISBS in a backscattering geometry is not realizable to measure the interior of bulk samples. However, it has been realized for surfaces in a reflection geometry. Since many biological samples are either naturally thin or can often be made thin, this is not out of range for ISBS applications.

At this point, a comparison needs to be made between the two pulse lengths. We have already seen that with either 1 ns or 6 ps pump pulses, both with the same energy per pulse, the signal strengths are comparable. The answer depends on the application. Since thermal damage from absorption is lower with picosecond pulses compared to nanosecond, picosecond pulses are more desirable if a study is being done using only electrostrictive gratings. Also, in the picosecond regime, many nonlinear effects will happen in addition to ISBS; effects which can be used to probe other aspects of the material simultaneously. However, these nonlinear effects can be very undesirable in some materials, thus nanosec-

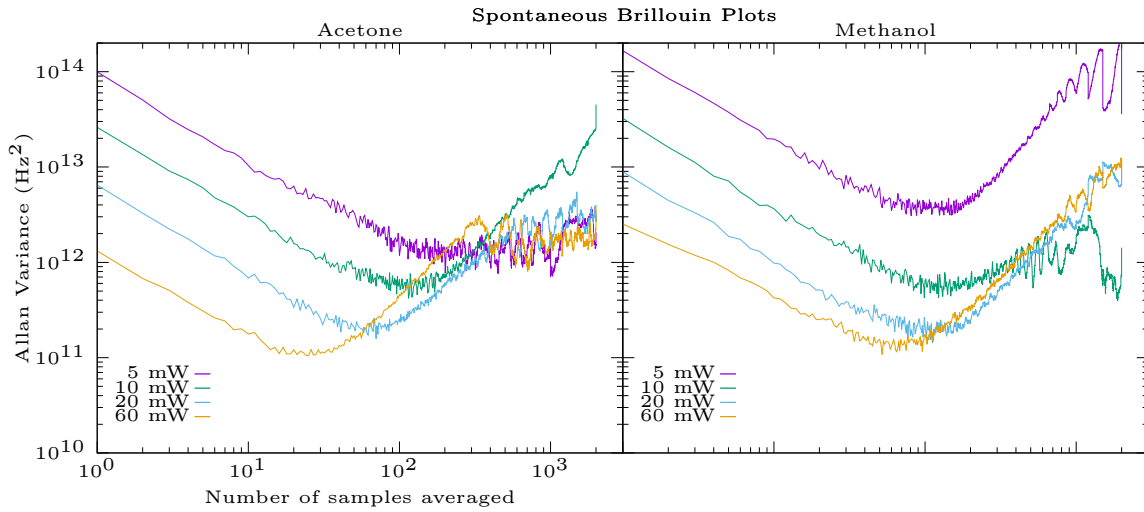


Figure 5.11: The Allan variance of the SpBS signal of acetone and methanol verses the number of samples taken.

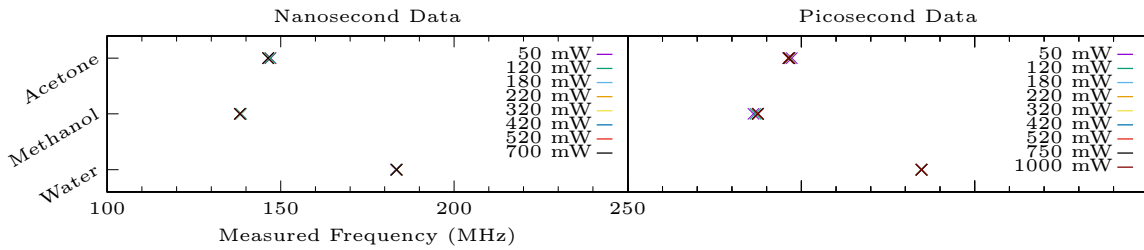


Figure 5.12: Measured ISBS frequencies using the number of averages required for the minimum uncertainty.

ond would be better in this instance. In order for ISBS to be impulsive, the pulse length must be shorter than the acoustic period of the generated sound wave. Therefore, for high frequency sound waves that are  $\geq 1$  GHz, pulses have to be in the sub-nanosecond range.

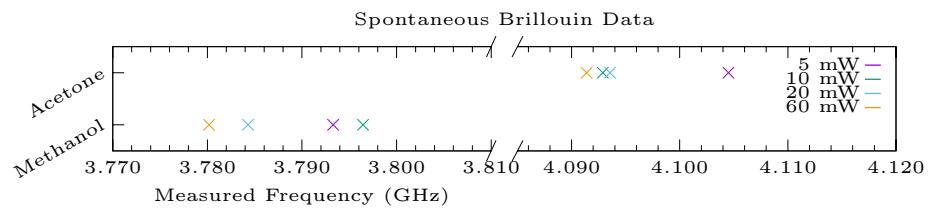


Figure 5.13: Measured SpBS frequencies using the number of averages required for the minimum uncertainty.

## 6. CONCLUSION AND FURTHER WORK

In conclusion, we explored several ways that stimulated Brillouin scattering can be implemented for spectroscopic, and more importantly, for microscopic purposes. Both spontaneous and stimulated Brillouin scattering have their strengths and weaknesses, which we performed a comparison between them as a guide for future reference when trying to decide which method is appropriate for the task at hand. We also explored gain in a three-level  $\Lambda$  system with hopes that the general method will provide a useful technique for spectroscopy in the future. All experiments were designed with biological purposes in mind, and there is still much work to be done to effectively obtain commercial systems using this principle. However, these methods are rich with information that they can provide and are waiting to be explored.

## REFERENCES

- [1] P. Ramachandran and G. Varoquaux, “Mayavi: 3D Visualization of Scientific Data,” *Computing in Science & Engineering*, vol. 13, no. 2, pp. 40–51, 2011.
- [2] L. I. Mandelstam, “Light scattering by inhomogeneous media,” *Zh. Russ. Fiz-Khim. Ova.*, vol. 58, p. 381, 1926.
- [3] L. Brillouin, “Diffusion de la lumiere et des rayones X par un corps transparent homogene; influence del’agitation thermique,” *Ann. Phys. (Paris)*, vol. 17, pp. 88–122, 1922.
- [4] E. Gross, “Change of Wave-length of Light due to Elastic Heat Waves at Scattering in Liquids,” *Nature*, vol. 126, p. 201, 1930.
- [5] N. Berovic, N. Thomas, R. A. Thornhill, and J. M. Vaughan, “Observation of Brillouin scattering from single muscle fibres,” *European Biophysics Journal*, vol. 17, pp. 69–74, 1989.
- [6] V. Mathieu, K. Fukui, M. Matsukawa, M. Kawabe, R. Vayron, E. Soffer, F. Anagnostou, and G. Haiat, “Micro-Brillouin Scattering Measurements in Mature and Newly Formed Bone Tissue Surrounding an Implant.,” *Journal of Biomechanical Engineering*, vol. 133, p. 021006, Feb 2011.
- [7] G. Scarcelli and S. H. Yun, “Confocal Brillouin microscopy for three-dimensional mechanical imaging.,” *Nature Photonics*, vol. 2, pp. 39–43, Dec 2007.
- [8] K. J. Koski, P. Akhenblit, K. McKiernan, and J. L. Yarger, “Non-invasive determination of the complete elastic moduli of spider silks.,” *Nature Materials*, vol. 12, no. 3, pp. 262–267, 2013.

- [9] X. Jiang, M. Wang, K. Schmidt, E. Dunlop, J. Haupt, and W. Gissler, “Elastic constants and hardness of ion-beam-sputtered TiN<sub>x</sub> films measured by Brillouin scattering and depth-sensing indentation,” *Journal of Applied Physics*, vol. 69, no. 5, p. 3053, 1991.
- [10] S. O. Demokritov, B. Hillebrands, and A. N. Slavin, “Brillouin light scattering studies of confined spin waves: linear and nonlinear confinement,” *Physics Reports*, vol. 348, pp. 441–489, 2001.
- [11] X. Bao, M. DeMerchant, A. Brown, and T. Bremner, “Tensile and Compressive Strain Measurement in the Lab and Field With the Distributed Brillouin Scattering Sensor,” *Journal of Lightwave Technology*, vol. 19, no. 11, pp. 1698–1704, 2001.
- [12] T. R. Parker, M. Farhadiroushan, V. A. Handerek, and A. J. Rogers, “A Fully Distributed Simultaneous Strain and Temperature Sensor using Spontaneous Brillouin Backscatter,” *IEEE Photonics Technology Letters*, vol. 9, no. 7, pp. 979–981, 1997.
- [13] R. Vacher and L. Boyer, “Brillouin Scattering: A Tool for the Measurement of Elastic and Photoelastic Constants,” *Physical Review B*, vol. 6, no. 2, pp. 639–673, 1970.
- [14] C. H. Whitfield, E. M. Brody, and W. a. Bassett, “Elastic moduli of NaCl by Brillouin scattering at high pressure in a diamond anvil cell,” *Review of Scientific Instruments*, vol. 47, no. 8, p. 942, 1976.
- [15] J. Xu, X. Ren, W. Gong, R. Dai, and D. Liu, “Measurement of the bulk viscosity of liquid by Brillouin scattering,” *Applied Optics*, vol. 42, no. 33, p. 6704, 2003.
- [16] R. W. Boyd, *Nonlinear Optics*. Burlington, MA: Academic Press, 3rd ed. ed., 2008.
- [17] P. Zinin, M. H. Manghnani, X. Zhang, H. Feldermann, C. Ronning, and H. Hof-sass, “Surface Brillouin scattering of cubic boron nitride films,” *Journal of Applied Physics*, vol. 91, no. 7, p. 4196, 2002.

- [18] M. G. Beghi, C. E. Bottani, P. M. Ossi, T. a. Lafford, and B. K. Tanner, “Combined surface Brillouin scattering and x-ray reflectivity characterization of thin metallic films,” *Journal of Applied Physics*, vol. 81, no. 2, p. 672, 1997.
- [19] G. D. Hickman, J. M. Harding, M. Carnes, A. Pressman, G. W. Kattawar, and E. S. Fry, “Aircraft Laser Sensing of Sound Velocity in Water: Brillouin Scattering,” *Remote Sens. Environ.*, vol. 36, no. 3, pp. 165–178, 1991.
- [20] K. Schorstein, A. Popescu, G. Scheich, T. Walther, and E. S. Fry, “Towards a Brillouin-LIDAR for remote sensing of the temperature profile in the ocean,” *IEEE Oceans 2006*, 2006.
- [21] K. Schorstein, E. S. Fry, and T. Walther, “Depth-resolved temperature measurements of water using the Brillouin lidar technique,” *Applied Physics B*, vol. 97, pp. 931–934, Jul 2009.
- [22] Z. Meng, A. J. Traverso, and V. V. Yakovlev, “Background clean-up in Brillouin microspectroscopy of scattering medium,” *Optics Express*, vol. 22, no. 5, pp. 144–148, 2014.
- [23] Z. Meng and V. V. Yakovlev, “Optimizing signal collection efficiency of the VIPA-based Brillouin spectrometer,” *Journal of Innovative Optical Health Sciences*, vol. 8, p. 1550021, Nov 2015.
- [24] Z. Meng and V. V. Yakovlev, “Subcellular imaging of mechanical and chemical properties using Brillouin and Raman microspectroscopies,” *Proc. of SPIE*, vol. 9328, p. 93280P, 2015.
- [25] C. Rossignol, N. Chigarev, M. Ducouso, B. Audoin, G. Forget, F. Guillemot, and M. C. Durrieu, “In Vitro picosecond ultrasonics in a single cell,” *Applied Physics Letters*, vol. 93, no. 12, pp. 1–3, 2008.

- [26] M. Ducouso, T. Dehoux, B. Audoin, O. Zouani, C. Chollet, and M. C. Durrieu, “Picosecond ultrasonics in single cells: Interface step motion for thin animal cells and Brillouin scattering for thick vegetal cells,” *Journal of Physics: Conference Series*, vol. 269, p. 012024, 2011.
- [27] B. Stephanidis, S. Adichtchev, P. Gouet, A. McPherson, and A. Mermet, “Elastic Properties of Viruses.,” *Biophysical Journal*, vol. 93, no. 4, pp. 1354–1359, 2007.
- [28] Z. Steelman, Z. Meng, A. J. Traverso, and V. V. Yakovlev, “Brillouin spectroscopy as a new method of screening for increased CSF total protein during bacterial meningitis,” *Journal of Biophotonics*, vol. 8, no. 5, pp. 408–414, 2015.
- [29] Z. Meng, R. Baker, V. M. Panin, and V. V. Yakovlev, “Brillouin spectroscopy reveals changes in muscular viscoelasticity in *Drosophila* POMT mutants,” in *Proc. of SPIE* (K. V. Larin and D. D. Sampson, eds.), vol. 9327, p. 932713, Mar 2015.
- [30] Z. Meng and V. V. Yakovlev, “Brillouin spectroscopy characterizes microscopic viscoelasticity associated with skin injury,” in *Proc. of SPIE* (E. D. Jansen, ed.), vol. 9321, p. 93210C, Mar 2015.
- [31] Z. Meng, B. Basagaoglu, and V. V. Yakovlev, “Atherosclerotic plaque detection by confocal Brillouin and Raman microscopies,” in *Proc. of SPIE* (B. Choi, N. Kollias, H. Zeng, H. W. Kang, B. J. F. Wong, J. F. Ilgner, A. Nuttal, C.-P. Richter, M. C. Skala, M. W. Dewhirst, G. J. Tearney, K. W. Gregory, L. Marcu, A. Mandelis, and M. D. Morris, eds.), vol. 9303, p. 93033N, Feb 2015.
- [32] Z. Meng and V. V. Yakovlev, “Probing microscopic mechanical properties of hard tissues with Brillouin spectroscopy,” *Proceedings of SPIE*, vol. 9303, p. 930342, Feb 2015.



- [33] A. J. Traverso, C. O. Brien, J. V. Thompson, L. Yuan, G. I. Petrov, B. H. Hokr, C. W. Ballmann, A. A. Svidzinsky, M. O. Scully, and V. V. Yakovlev, “Directional Coherent Light via Intensity Induced Sideband Emission,” *Light: Science & Applications*, vol. 6, 2017.
- [34] R. E. Grove, F. Y. Wu, and S. Ezekiel, “Measurement of the spectrum of resonance fluorescence from a two-level atom in an intense monochromatic field,” *Physical Review A*, vol. 15, no. 1, pp. 227–233, 1977.
- [35] W. Hanle, “Über magnetische Beeinflussung der Polarisation der Resonanzfluoreszenz,” *Z. Phys.*, vol. 30, no. 1, pp. 93–105, 1924.
- [36] S. E. Harris, “Lasers without inversion: Interference of lifetime-broadened resonances,” *Phys. Rev. Lett.*, vol. 62, no. 9, pp. 1033–1036, 1989.
- [37] M. O. Scully, S. Y. Zhu, and A. Gavrielides, “Degenerate quantum-beat laser: Lasing without inversion and inversion without lasing,” *Physical Review Letters*, vol. 62, no. 24, pp. 2813–2816, 1989.
- [38] S. E. Harris, J. E. Feild, and A. Imamoglu, “Nonlinear Optical Processes using Electromagnetically Induced Transparency,” *Phys. Rev. Lett.*, vol. 64, no. 10, pp. 1107–1110, 1990.
- [39] H. R. Gray, R. M. Whitley, and C. R. Stroud, “Coherent trapping of atomic populations,” *Optics Letters*, vol. 3, no. 6, pp. 218–220, 1978.
- [40] B. R. Mollow, “Stimulated Emission and Absorption near Resonance for Driven Systems,” *Physical Review A*, vol. 5, no. December, pp. 2217–2222, 1972.
- [41] F. Y. Wu, S. Ezekiel, M. Ducloy, and B. R. Mollow, “Observation of Amplification in a Strongly Driven Two-Level Atomic System at Optical Frequencies,” *Physical Review Letters*, vol. 38, no. 19, p. 1077, 1977.

- [42] C. Mavroyannis, “Strong amplification of sidebands in a strongly driven three-level atomic system,” *J. Math. Phys.*, vol. 26, no. 5, pp. 1093–1101, 1985.
- [43] L. M. Narducci, M. O. Scully, G.-L. Oppo, P. Ru, and J. R. Tredicce, “Spontaneous emission and absorption properties of a driven three-level system,” *Physical Review A*, vol. 42, no. 3, pp. 1630–1649, 1990.
- [44] A. S. Manka, H. M. Doss, L. M. Narducci, P. Ru, and G.-L. Oppo, “Spontaneous emission and absorption properties of a driven three-level system. II. the  $\Lambda$  and cascade models,” *Physical Review A*, vol. 43, no. 7, pp. 3748–3763, 1991.
- [45] A. D. Wilson-Gordon, “Gain in a three-level  $\Lambda$  system driven by a single pump,” *Phys. Rev. A*, vol. 48, no. 6, pp. 4639–4647, 1993.
- [46] J. D. Jackson, *Classical Electrodynamics*. Wiley, 3rd ed., 1999.
- [47] I. L. Fabelinskii, *Molecular Scattering of Light*. New York, NY: Plenum Press, 1968.
- [48] H. Boersch and H. Eichler, “Beugung an einem mit stehenden Lichtwellen gepumpten Rubin,” *Zeitschrift für Angewandte Physik*, vol. 22, no. 5, p. 378, 1967.
- [49] H. J. Eichler, P. Günter, and D. W. Pohl, *Laser-induced dynamic gratings*. Springer series in optical sciences: v. 50, Berlin ; New York : Springer-Verlag, 1986., 1986.
- [50] J. A. Rogers, M. Fuchs, M. J. Banet, J. B. Hanselman, R. Logan, and K. A. Nelson, “Optical system for rapid materials characterization with the transient grating technique: Application to nondestructive evaluation of thin films used in microelectronics,” *Applied Physics Letters*, vol. 71, no. 2, p. 225, 1997.
- [51] A. A. Maznev, K. A. Nelson, and J. A. Rogers, “Optical heterodyne detection of laser-induced gratings,” *Optics letters*, vol. 23, no. 16, pp. 1319–1321, 1998.
- [52] L. S. Cutler and C. L. Searle, “Some Aspects of the Theory and Measurement of Frequency Fluctuations in Frequency Standards,” *Proceedings of the IEEE*, vol. 54,

- no. 2, pp. 136–154, 1966.
- [53] D. B. Leeson, “A Simple Model of Feedback Oscillator Noise Spectrum,” *Proceedings of the IEEE*, vol. 54, no. 2, pp. 329–330, 1966.
- [54] D. W. Allan, “Statistics of Atomic Frequency Standards,” *Proceedings of the IEEE*, vol. 54, no. 2, pp. 221–230, 1966.
- [55] “IEEE Standard Definitions of Physical Quantities for Fundamental Frequency and Time Metrology - Random Instabilities,” *IEEE Std 1139-1999*, 1999.
- [56] A. J. Traverso, J. V. Thompson, Z. A. Steelman, Z. Meng, M. O. Scully, and V. V. Yakovlev, “Dual Raman-Brillouin Microscope for Chemical and Mechanical Characterization and Imaging,” *Analytical Chemistry*, vol. 87, no. 15, pp. 7519–7523, 2015.
- [57] R. Y. Chiao, C. H. Townes, and B. P. Stoicheff, “Stimulated Brillouin Scattering and Coherent Generation of Intense Hypersonic Waves,” *Physical Review Letters*, vol. 12, no. 21, pp. 592–595, 1964.
- [58] W. T. Grubbs and R. A. MacPhail, “High resolution stimulated Brillouin gain spectrometer,” *Review of Scientific Instruments*, vol. 65, no. 1, pp. 34–41, 1994.
- [59] M. Niklès, L. Thévenaz, and P. A. Robert, “Brillouin gain spectrum characterization in single-mode optical fibers,” *Journal of Lightwave Technology*, vol. 15, no. 10, pp. 1842–1851, 1997.
- [60] K. J. Koski and J. L. Yarger, “Brillouin imaging,” *Applied Physics Letters*, vol. 87, no. 6, p. 061903, 2005.
- [61] J. E. Bertie and Z. Lan, “Infrared Intensities of Liquids XX: The Intensity of the OH Stretching Band of Liquid Water Revisited, and the Best Current Values of the Optical Constants of H<sub>2</sub>O(l) at 25°C between 15,000 and 1 cm<sup>-1</sup>,” *Applied Spectroscopy*,

- vol. 50, no. 8, pp. 1047–1057, 1996.
- [62] S. M. Karim, “Second Viscosity Coefficient of Liquids,” *The Journal of the Acoustical Society of America*, vol. 25, no. 5, pp. 997–1002, 1953.
- [63] A. Hopt and E. Neher, “Highly Nonlinear Photodamage in Two-Photon Fluorescence Microscopy,” *Biophysical Journal*, vol. 80, no. April, pp. 2029–2036, 2001.
- [64] V. V. Yakovlev, “Advanced instrumentation for non-linear Raman microscopy,” *Journal of Raman Spectroscopy*, vol. 34, pp. 957–964, dec 2003.
- [65] Y. Fu, H. Wang, R. Shi, and J.-X. Cheng, “Characterization of photodamage in coherent anti-Stokes Raman scattering microscopy,” *Optics Express*, vol. 14, no. 9, p. 3942, 2006.
- [66] A. M. Akulshin, R. J. McLean, A. I. Sidorov, and P. Hannaford, “Coherent and collimated blue light generated by four-wave mixing in Rb vapour,” *Opt. Express*, vol. 17, no. 25, pp. 22861–22870, 2009.
- [67] D. A. Steck, “Rubidium 85 D line data,” *available online at <http://steck.us/alkalidata>*, 2013.
- [68] D. A. Steck, “Rubidium 87 D Line Data,” *available online at <http://steck.us/alkalidata>*, 2008.
- [69] P. L. Bender, E. C. Beaty, and A. R. Chi, “Optical detection of narrow Rb87 hyperfine absorption lines,” *Phys. Rev. Lett.*, vol. 1, no. 9, pp. 311–313, 1958.
- [70] K. Ernst and F. Strumia, “High Efficiency Hyperfine Pumping of Cesium Vapor,” *Physical Review*, vol. 170, no. 1, pp. 48–49, 1968.
- [71] A. Moretti and F. Strumia, “Hyperfine optical pumping of sodium vapors,” *Physical Review A*, vol. 3, no. 1, pp. 349–354, 1971.
- [72] C. Cohen-Tannoudji, B. Diu, and F. Laloe, *Quantum Mechanics, Vol I*. Wiley, 1991.

- [73] G. Scarcelli, W. J. Polacheck, H. T. Nia, K. Patel, A. J. Grodzinsky, R. D. Kamm, and S. H. Yun, “Noncontact three-dimensional mapping of intracellular hydromechanical properties by Brillouin microscopy,” *Nature Methods*, vol. 12, no. 12, pp. 1132–1134, 2015.
- [74] Z. Meng, A. J. Traverso, C. W. Ballmann, M. Troyanova-Wood, and V. V. Yakovlev, “Seeing cells in a new light: a renaissance of Brillouin spectroscopy,” *Advances in Optics and Photonics*, vol. 8, no. 2, pp. 300–327, 2016.
- [75] M. B. Hakim, S. M. Lindsay, and J. Powell, “The speed of sound in DNA.,” *Biopolymers*, vol. 23, no. 7, pp. 1185–92, 1984.
- [76] R. Harley, D. James, A. Miller, and J. W. White, “Phonons and the elastic moduli of collagen and muscle,” *Nature*, vol. 267, no. 5608, pp. 285–287, 1977.
- [77] J. M. Vaughan and J. T. Randall, “Brillouin scattering, density and elastic properties of the lens and cornea of the eye,” *Nature*, vol. 284, no. 5755, pp. 489–491, 1980.
- [78] M. Shirasaki, “Large angular dispersion by a virtually imaged phased array and its application to a wavelength demultiplexer.,” *Optics letters*, vol. 21, no. 5, pp. 366–368, 1996.
- [79] G. Scarcelli and S. H. Yun, “Multistage VIPA etalons for high-extinction parallel Brillouin spectroscopy.,” *Optics express*, vol. 19, no. 11, pp. 10913–10922, 2011.
- [80] Z. Meng and V. V. Yakovlev, “Optimizing signal collection efficiency of the VIPA-based Brillouin spectrometer,” *Journal of Innovative Optical Health Sciences*, vol. 8, no. 4, p. 1550021, 2015.
- [81] Z. Meng and V. V. Yakovlev, “Precise Determination of Brillouin Scattering Spectrum Using a Virtually Imaged Phase Array (VIPA) Spectrometer and Charge-Coupled Device (CCD) Camera,” *Applied Spectroscopy*, vol. 0, no. 0, pp. 1–8, 2016.

- [82] C. L. Evans, E. O. Potma, M. Puoris'haag, D. Côté, C. P. Lin, and X. S. Xie, "Chemical imaging of tissue in vivo with video-rate coherent anti-Stokes Raman scattering microscopy.," *Proceedings of the National Academy of Sciences of the United States of America*, vol. 102, no. 46, pp. 16807–16812, 2005.
- [83] C. W. Ballmann, J. V. Thompson, A. J. Traverso, Z. Meng, M. O. Scully, and V. V. Yakovlev, "Stimulated Brillouin Scattering Microscopic Imaging," *Scientific Reports*, vol. 5, pp. 1–7, 2015.
- [84] I. Remer and A. Bilenca, "Background-free Brillouin spectroscopy in scattering media at 780 nm via stimulated Brillouin scattering," *Optics Letters*, vol. 41, no. 5, pp. 926–929, 2016.
- [85] K. A. Nelson and M. D. Fayer, "Laser induced phonons: A probe of intermolecular interactions in molecular solids," *The Journal of Chemical Physics*, vol. 72, no. 9, p. 5202, 1980.
- [86] K. A. Nelson, D. R. Lutz, M. D. Fayer, and L. Madison, "Laser induced phonon spectroscopy. Optical generation of ultrasonic waves and investigation of electronic excited-state interactions in solids," *Physical Review B*, vol. 24, no. 6, pp. 3261–3275, 1981.
- [87] M. Fayer, "Picosecond holographic grating generation of ultrasonic waves," *IEEE Journal of Quantum Electronics*, vol. 22, no. 8, pp. 1437–1452, 1986.
- [88] Z. Meng, G. I. Petrov, and V. V. Yakovlev, "Flow cytometry using Brillouin imaging and sensing via time-resolved optical (BISTRO) measurements," *Analyst*, vol. 140, no. 21, pp. 7160–7164, 2015.
- [89] E. Gross, "The Splitting of Spectral Lines at Scattering of Light by Liquids.," *Nature*, vol. 126, no. 3176, p. 400, 1930.

- [90] E. Gross, "Splitting of the Frequency of Light scattered by Liquids and Optical Anisotropy of Molecules.," *Nature*, vol. 126, no. 3181, pp. 603–604, 1930.
- [91] K. A. Nelson, R. J. D. Miller, D. R. Lutz, and M. D. Fayer, "Optical generation of tunable ultrasonic waves," *Journal of Applied Physics*, vol. 53, no. 2, p. 1144, 1982.
- [92] J. A. Johnson, A. A. Maznev, M. T. Bulsara, E. A. Fitzgerald, T. C. Harman, S. Calawa, C. J. Vineis, G. Turner, and K. A. Nelson, "Phase-controlled, heterodyne laser-induced transient grating measurements of thermal transport properties in opaque material," *Journal of Applied Physics*, vol. 111, pp. 1–19, 2012.
- [93] Z. Meng, G. I. Petrov, and V. V. Yakovlev, "High-speed assessment of liquid viscoelasticity in flow cytometry using nonlinear Brillouin spectroscopy," *Proc. of SPIE*, vol. 9327, p. 93270P, 2015.
- [94] H. V. Hance and J. K. Parks, "Wide-Band Modulation of a Laser Beam, Using Bragg-Angle Diffraction by Amplitude-Modulated Ultrasonic Waves," *J. Acoust. Soc. Am.*, vol. 38, no. 14, pp. 14–23, 1965.
- [95] G. Maret, R. Oldenbourg, G. Winterling, K. Dransfeld, and A. Rupprecht, "Velocity of high frequency sound waves in oriented DNA fibres and films determined by Brillouin scattering," *Colloid and Polymer Science*, vol. 257, no. 10, pp. 1017–1020, 1979.
- [96] H. Eichler, "Time and frequency behavior of sound waves thermally induced by modulated laser pulses," *Journal of Applied Physics*, vol. 44, no. 8, p. 3429, 1973.
- [97] A. E. Siegman, "Bragg diffraction of a Gaussian beam by a crossed-Gaussian volume grating.," *Journal of the Optical Society of America*, vol. 67, no. 4, pp. 545–550, 1977.

- [98] H. Eichler, "Laser-induced Grating Phenomena," *Optica Acta: International Journal of Optics*, vol. 24, no. 6, pp. 631–642, 1977.
- [99] B. Y. Zel'dovich, N. F. Pilipetsky, and V. V. Shkunov, *Principles of phase conjugation*, vol. 42. Springer-Verlag Berlin Heidelberg GmbH, 1985.



## APPENDIX A

### COMPUTER CODE FOR SBS MICROSCOPY EXPERIMENT

The following is the LabVIEW code to control the SBS experiment.

Sacher Controls Vortex Controls Lock-in/Power Controls XY Stage Scanning/Results Numeric Save **STOP**

Translation Stage Address Connect 2  
 \* GPIB0:1-INSTR OFF/ON

Single axis linear motion 2D scan

**Initial position**

X0 position 0.000000  
 Y0 position 0.000000  
 Reset And Reload Scan OK

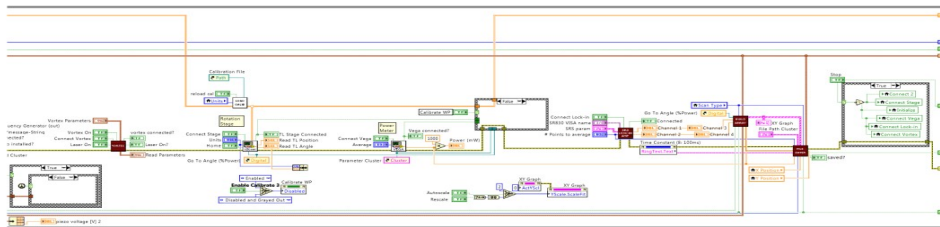
**XY scan parameters**

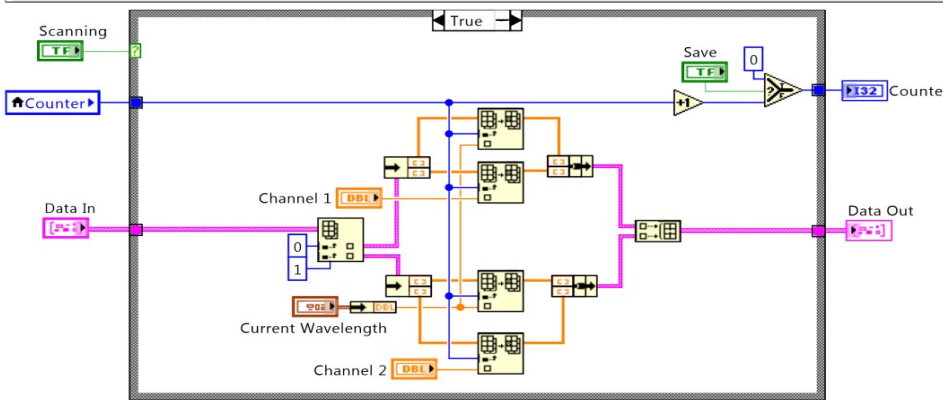
X Start 1.00000 Y Start 1.00000  
 X End 2.00000 Y End 2.00000  
 X Increment 0.250000 Y Increment 0.250000  
 size(t) 0  
 size(s) 2  
 Numeric 2 Next step x/y 4

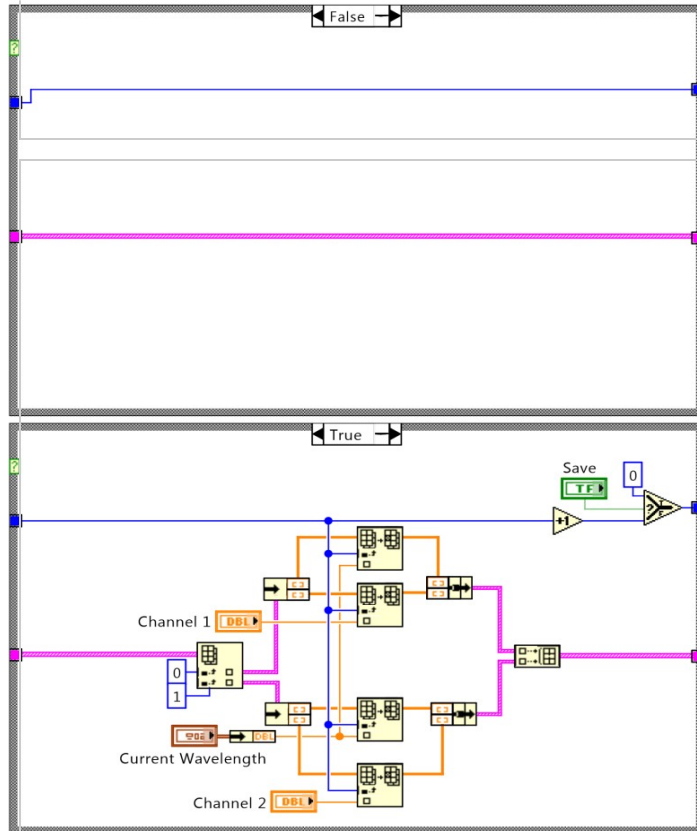
**Absolute or relative**

Absolute 0  
 X Position 0.000000  
 Y Position 0.000000  
 Reset Scan With Current Parameters OK

Array X	Array Y
0	1
1	1
1	1
1	1
2	1
2	1
2	1
1.75	1.25
1.75	1.25

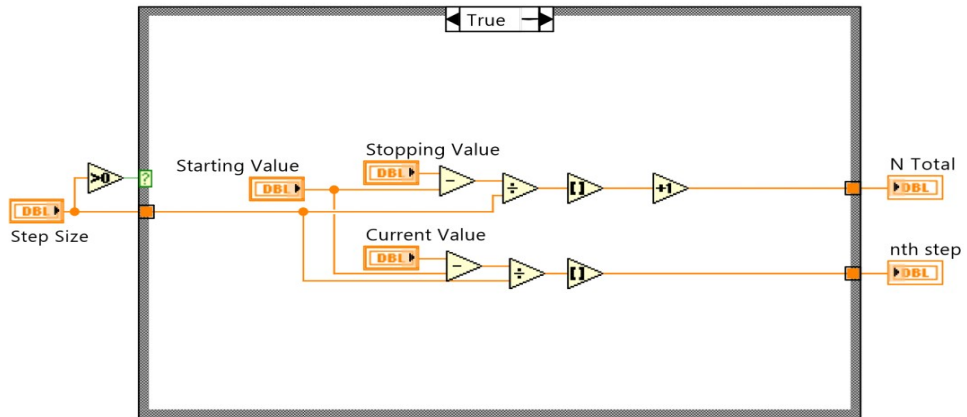


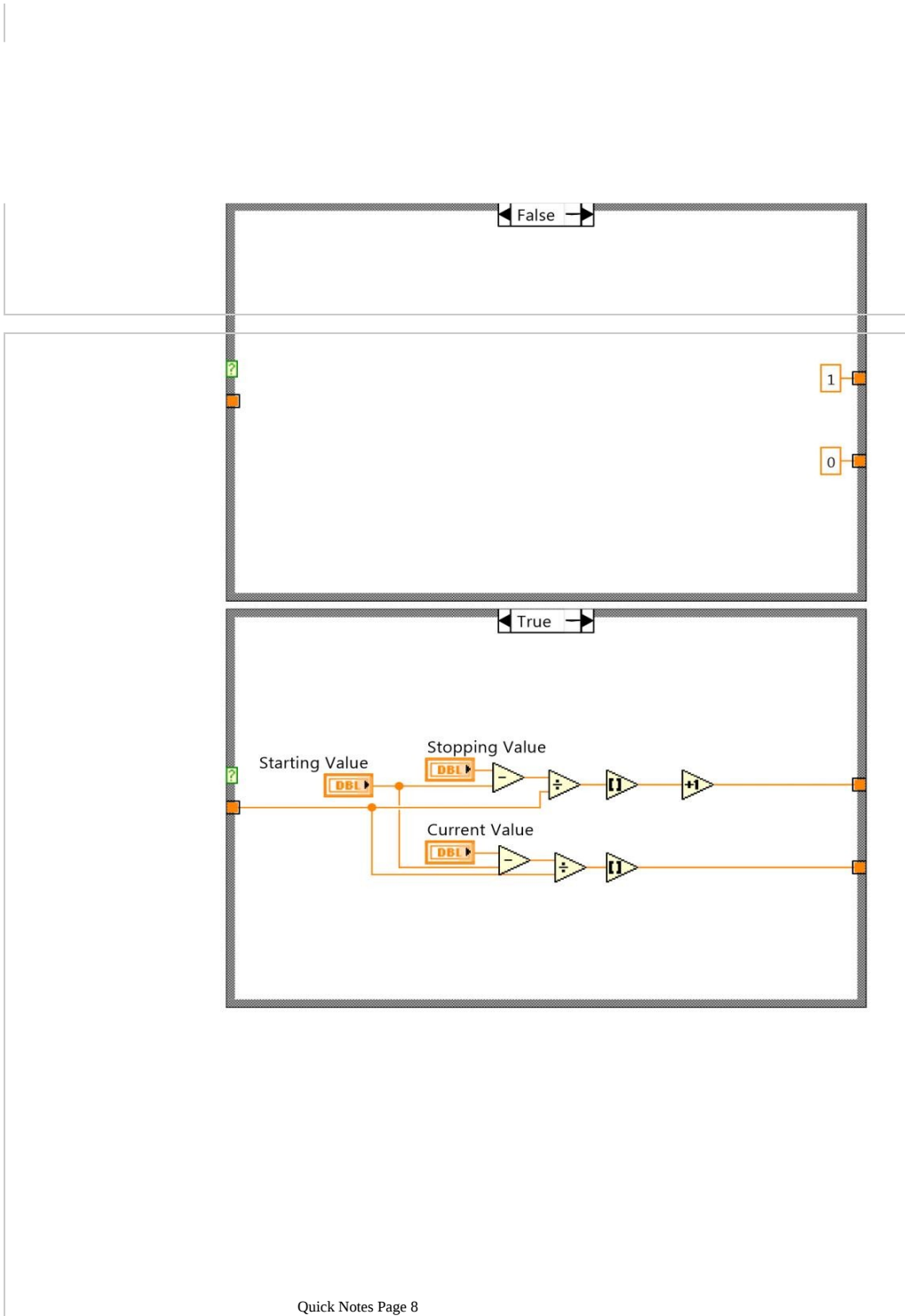




Starting Value	<input type="text" value="0"/>	nth step	<input type="text" value="0"/>
Stopping Value	<input type="text" value="0"/>	N Total	<input type="text" value="0"/>
Step Size	<input type="text" value="0"/>		
Current Value	<input type="text" value="0"/>		

# left = N(M-m)-n ; for 2d scan





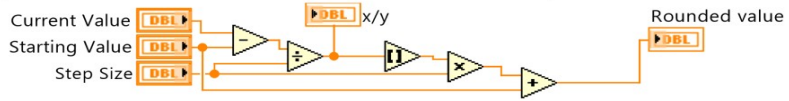
Starting Value

Current Value

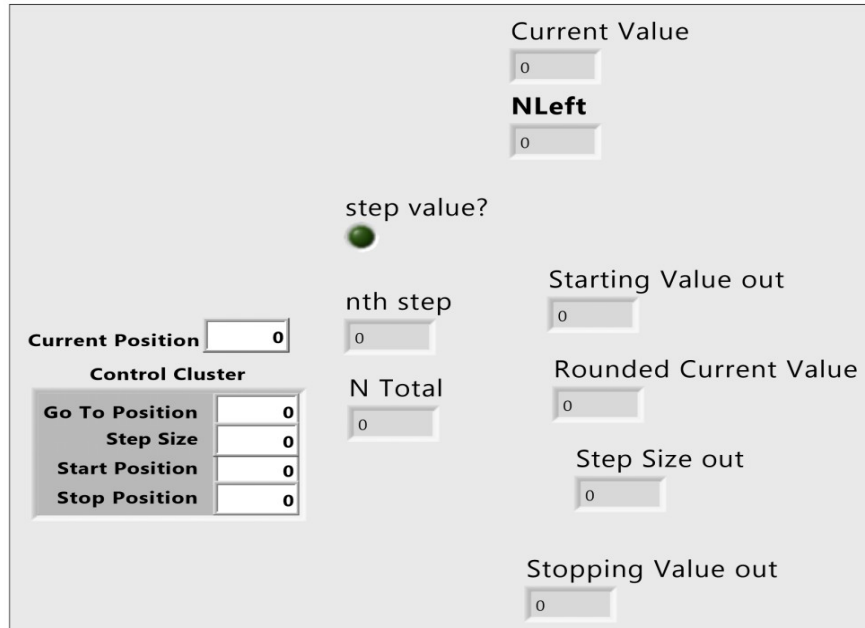
Step Size

x/y

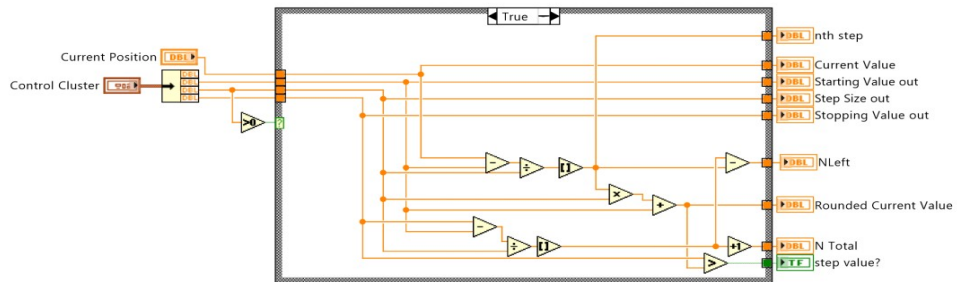
Rounded value

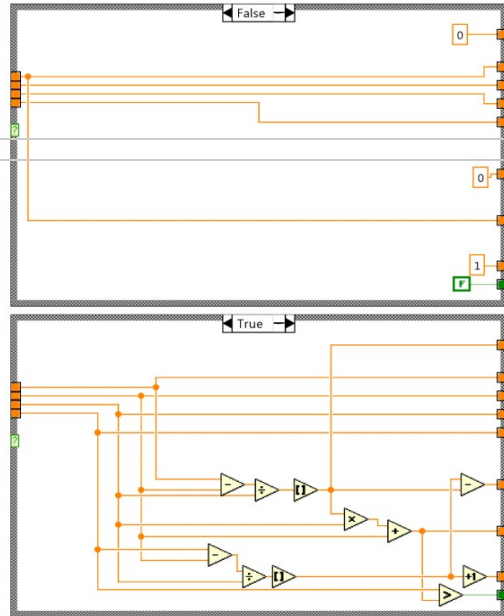


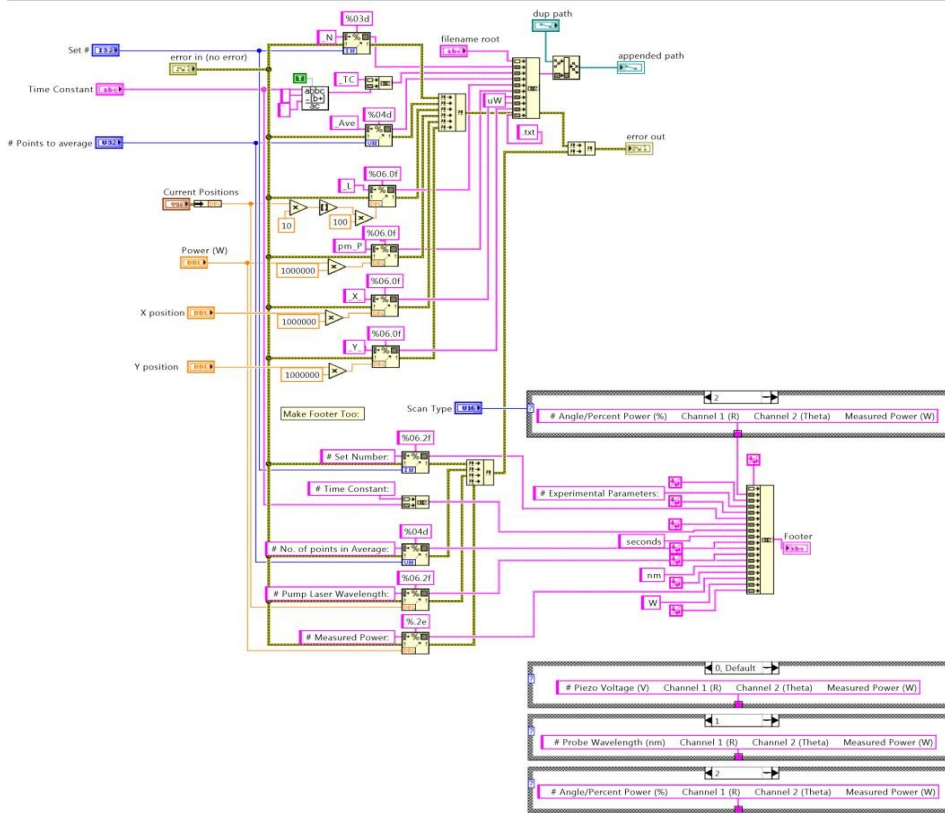
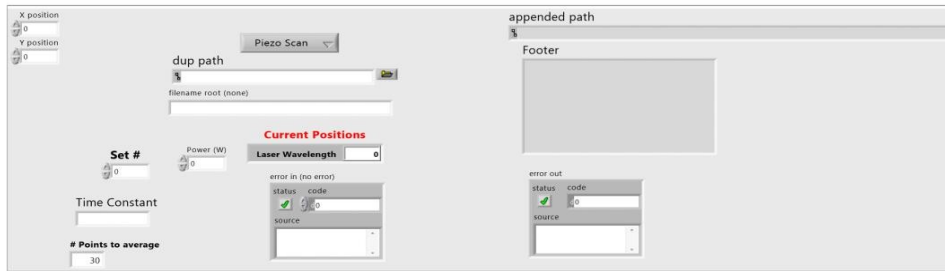




# left = N(M-m)·n ; for 2d scan







appended path

dup path

filename root (none)

**Current Positions**

Set # 0 Power (W) 0 Laser Wavelength 0

Pset Cluster error in (no error) status code source

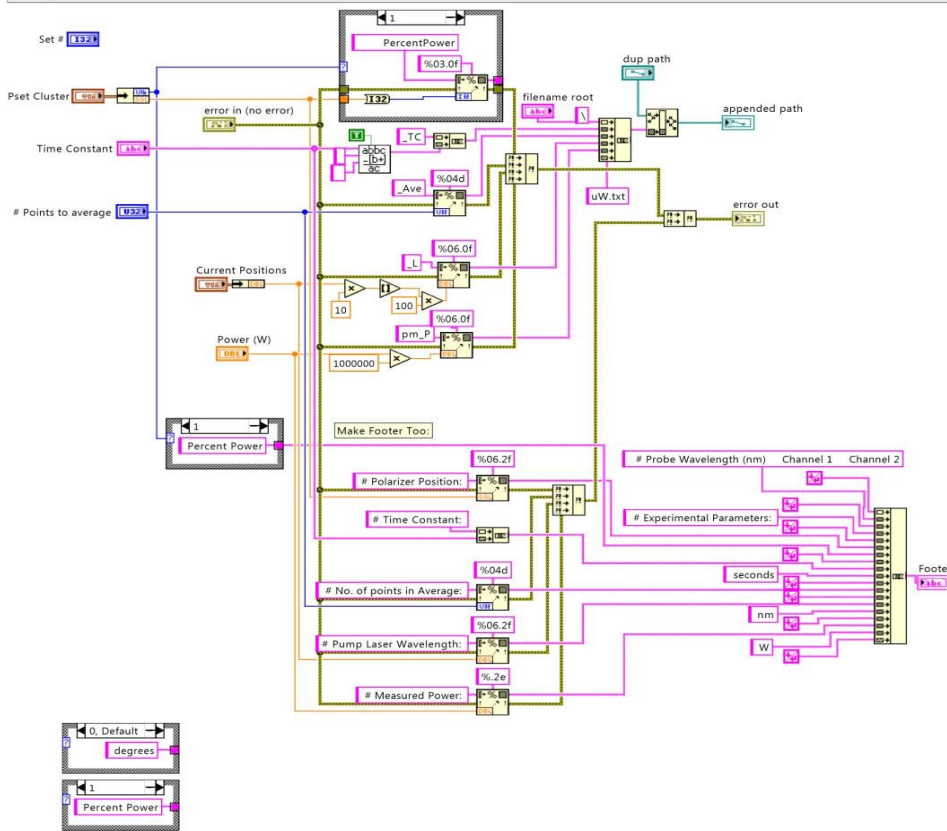
Time Constant Waveplate Angle 0

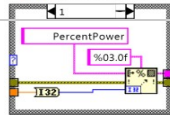
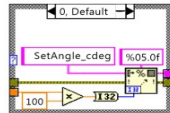
Units degrees

# Points to average 30

Footer

error out status code source





**Array**

**Power array (W)**

operation (0:open)

appended path in

**XY Data**

**xArray**

**Data In**

**xArray**

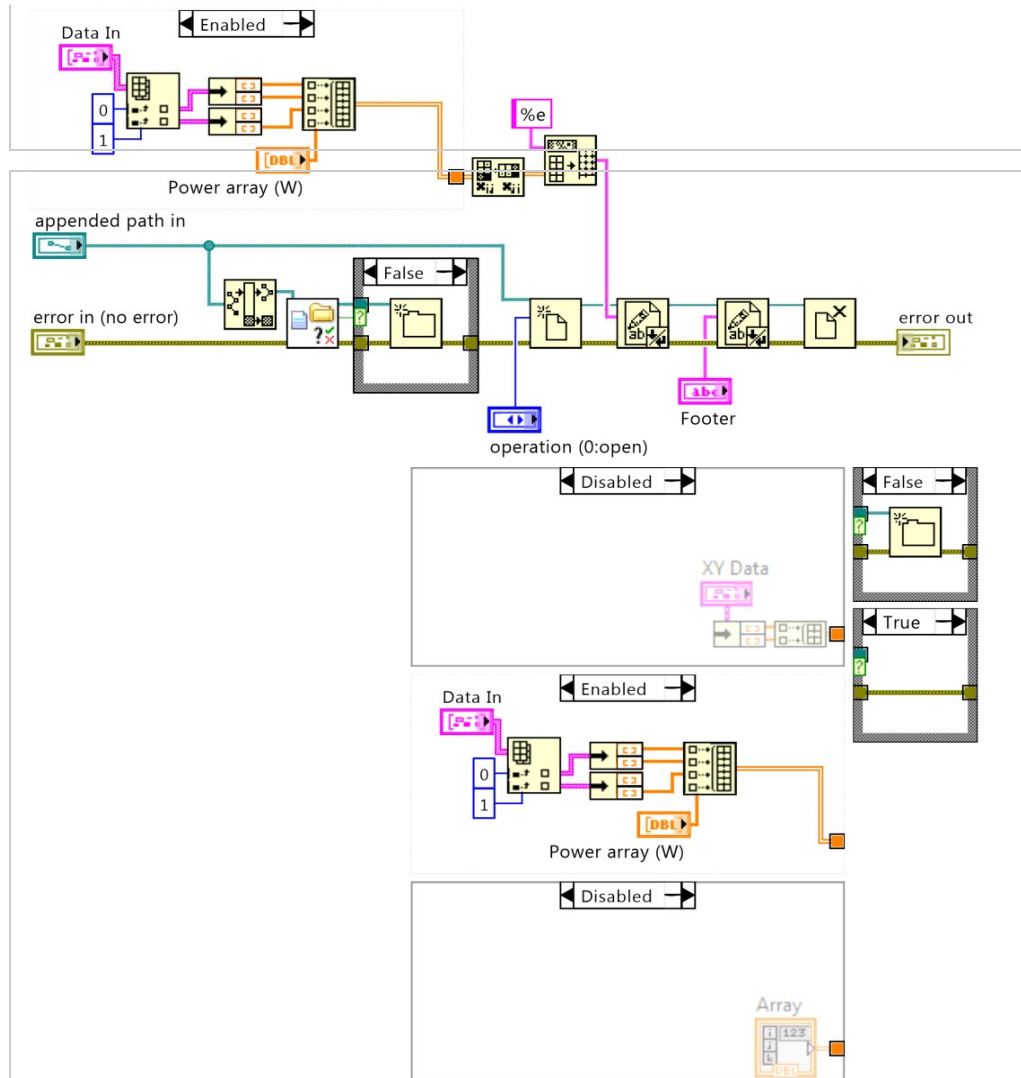
**Footer**

error in (no error)

status	code	
✔	0	<input type="text" value=""/>
source		
<input type="text" value=""/>		

error out

status	code	
✔	0	<input type="text" value=""/>
source		
<input type="text" value=""/>		



**Boolean**

laser current [A] 0  
 TEC temperature [°C] 0  
 piezo voltage [V] 0

Scan Type  
 Piezo Scan

Scanning

Laser Wavelength 780.00 nm

Channel 1	Channel 2
0.00	0.00

Save Power (mW)

Set Pos Refnum 0

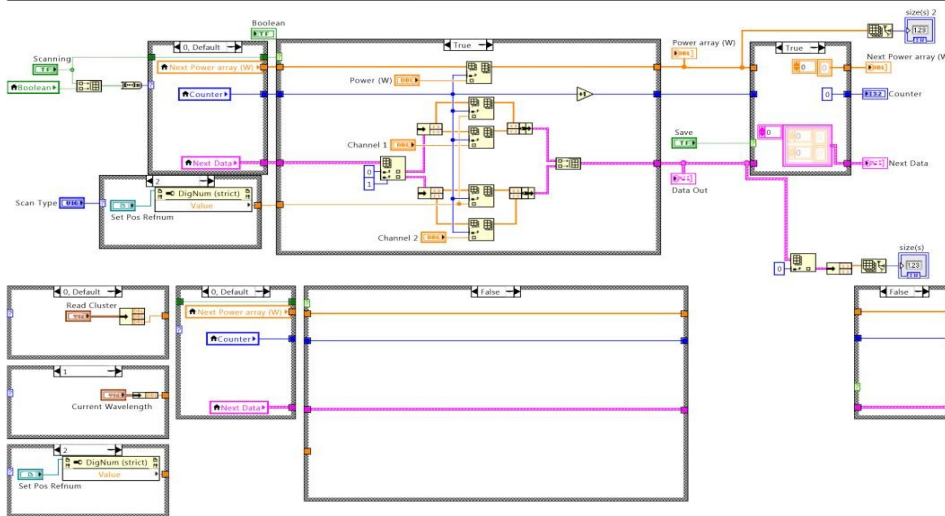
Next Data  
 size(s) 0  
 xArray

Next Power array (W)  
 size(s) 2  
 0

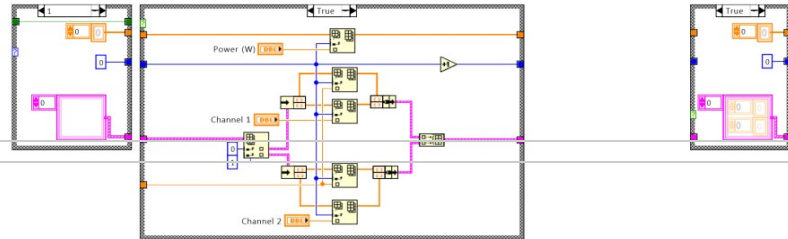
Counter  
 0

Data Out  
 xArray

Power array (W)  
 0







This sub-vi contains the Brains to Control: Set number Sacher Laser 1/Piezo. It also returns an ETA.

**Laser 1 Scan Control**

Go To Wavelength: 0  
Step Size: 0  
Start Wavelength: 0  
Stop Wavelength: 0

**Current Wavelength**

Laser 1: 780

error in: status code 0, source

**Piezo Scan Control**

Step Size[V]: 0.001  
Start Voltage[V]: 0.000  
Stop Voltage[V]: 0.000

# of Sets: 0

Start Scan, ABORT SCAN

Scan Type: Piezo Scan

**new wavelength** Move to Wav: 780.000

laser current [mA]: 0  
TEC temperature [°C]: 0  
piezo voltage [V]: 0.00

Current Time, Time Left, Set #

error out: status code, error 0, source

Save, Move to Wav 2, scanning?


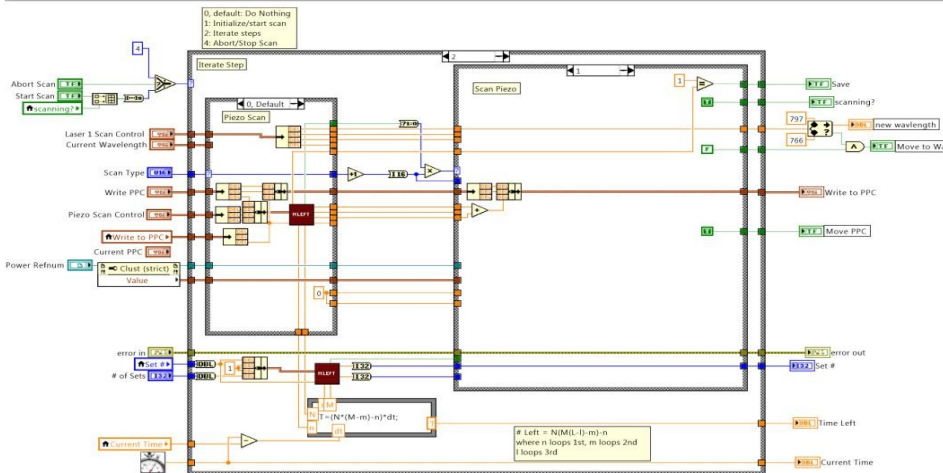
**Current PPC**

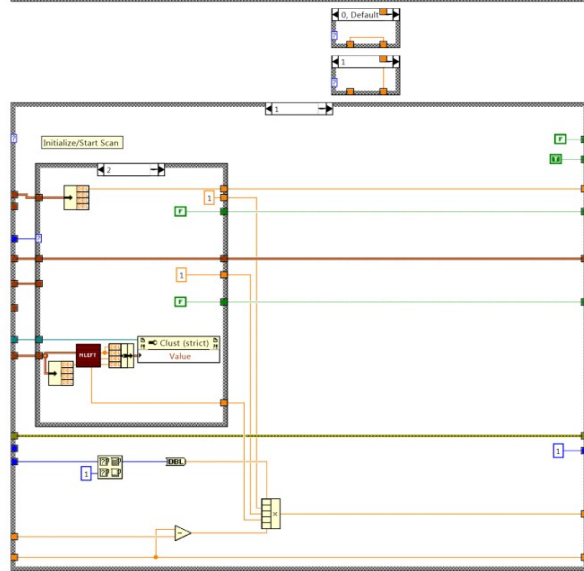
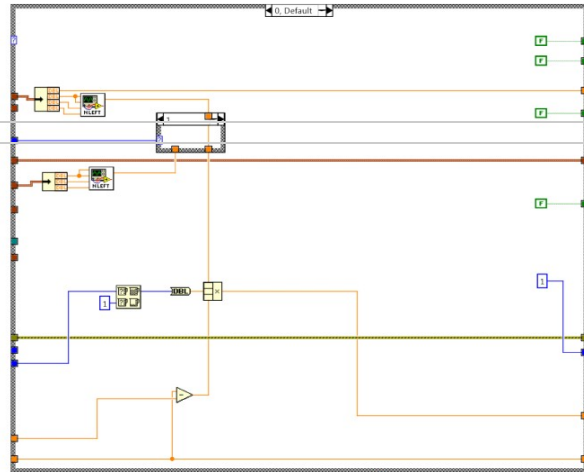
laser current [A]: 0  
TEC temperature [°C]: 0  
piezo voltage [V]: 0

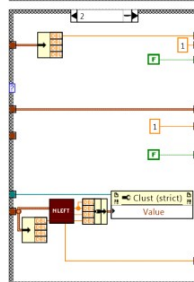
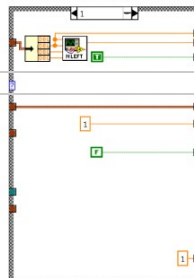
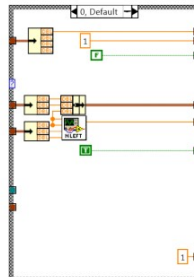
**Write PPC**

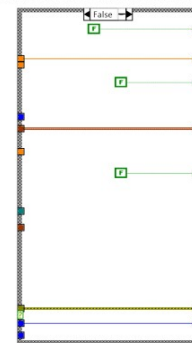
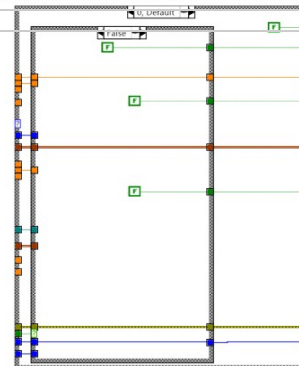
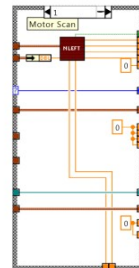
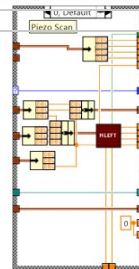
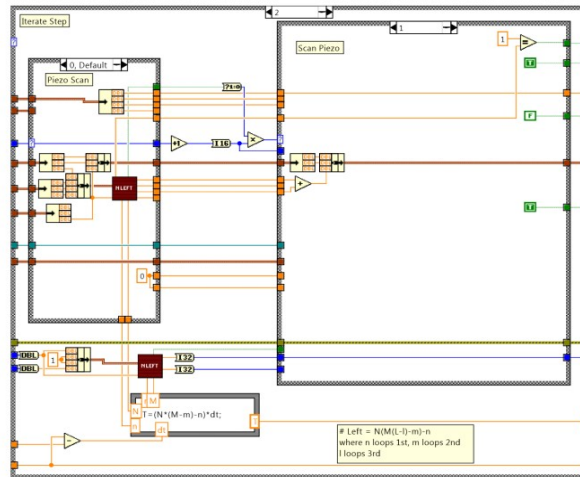
laser current [mA]: 0  
TEC temperature [°C]: 0  
piezo voltage [V]: 0.00

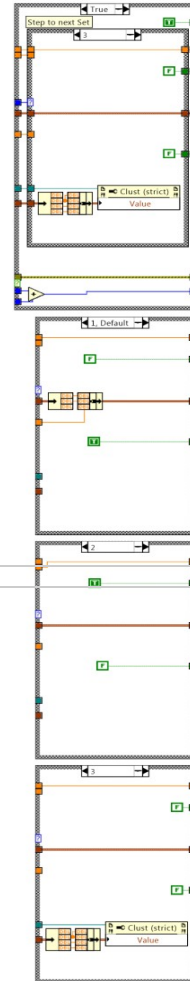
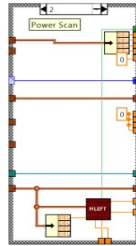
**Power Refnum**

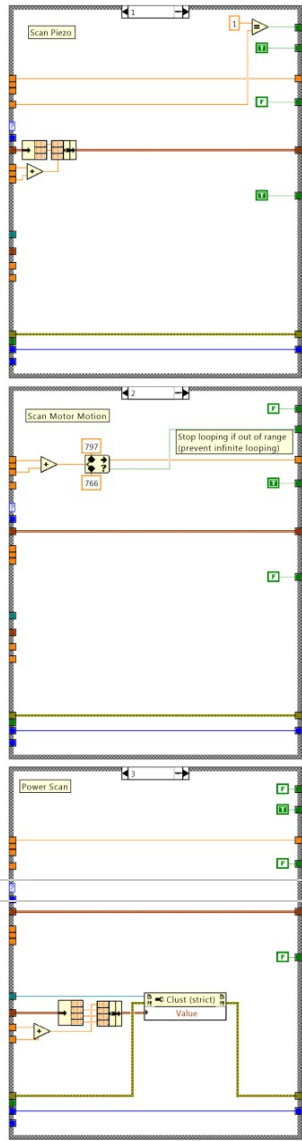



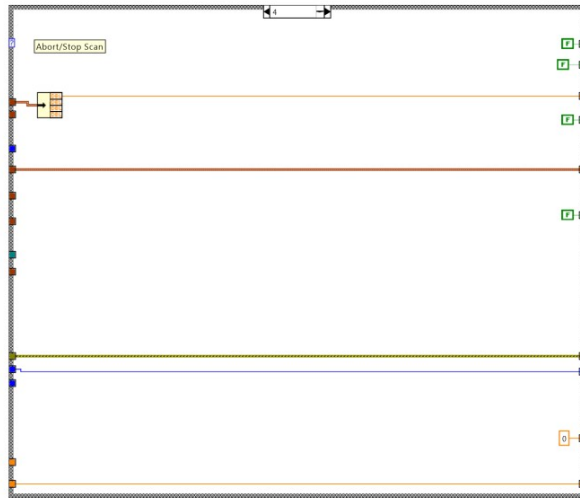














This sub-vi contains the Brains to Control: Sacher Laser 2, Sacher Laser 1, Thorlabs TDC001. It also returns an ETA.

**Laser 1 Scan Control**

Go To Wavelength: 0  
Step Size: 0  
Start Wavelength: 0  
Stop Wavelength: 0

**Current Wavelength**

Laser 1: 780

error in: status code 0, source

**Laser 2 Scan Control**

Go To Wavelength: 0  
Step Size: 0  
Start Wavelength: 0  
Stop Wavelength: 0

**Current Wavelength 2**

Laser 2: 780

Waveplate Refnum: Start Scan, ABORT SCAN

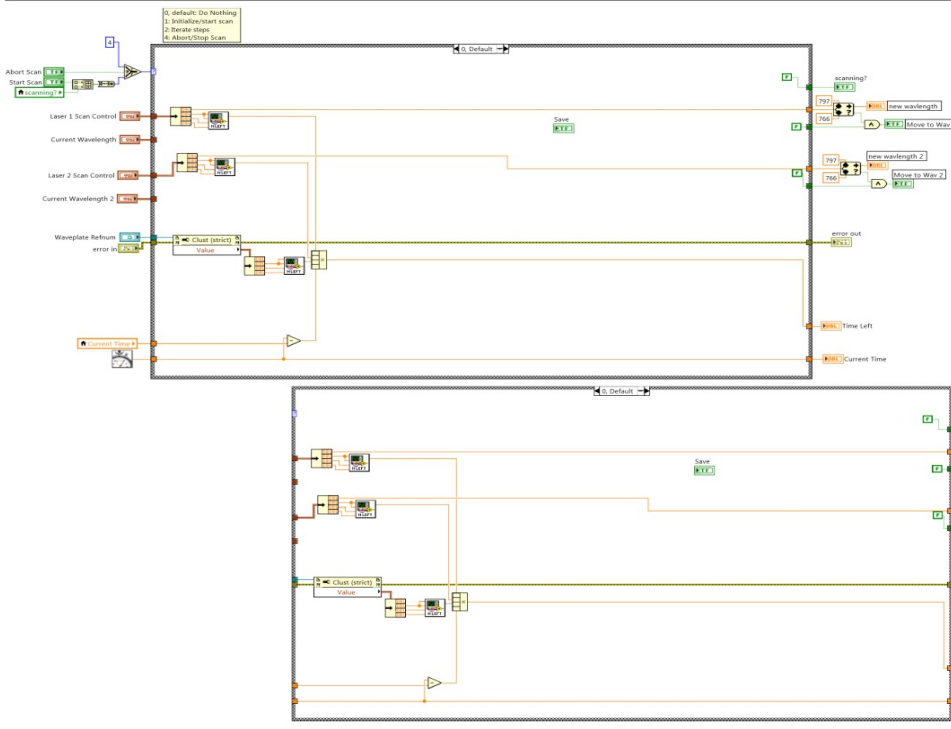
**new wavelength** Move to Wav: 780.000

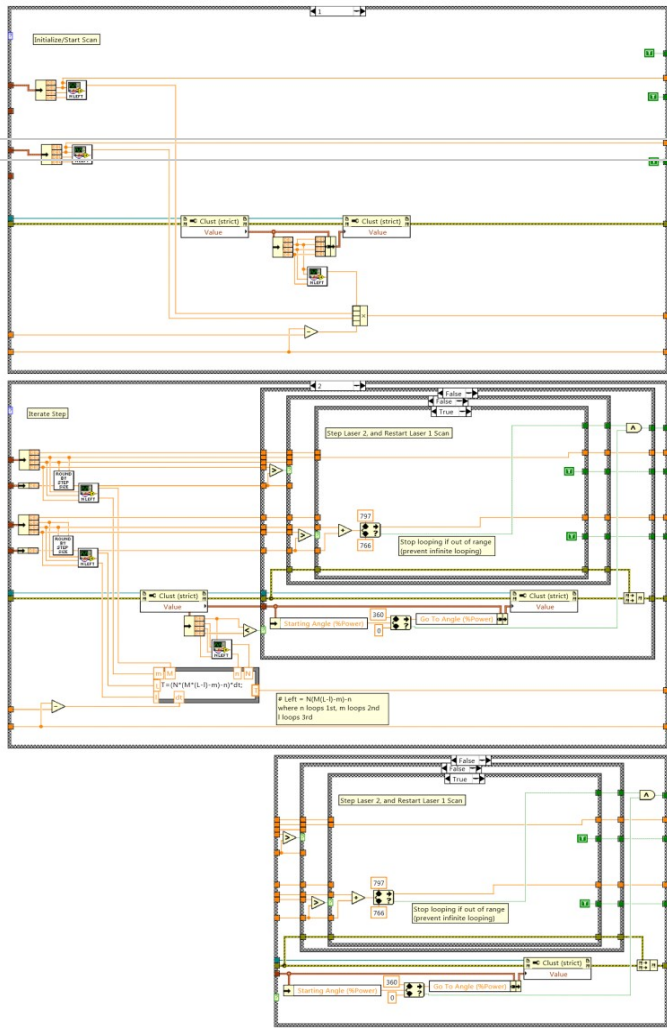
**new wavelength 2** Move to Wav 2: 780.000

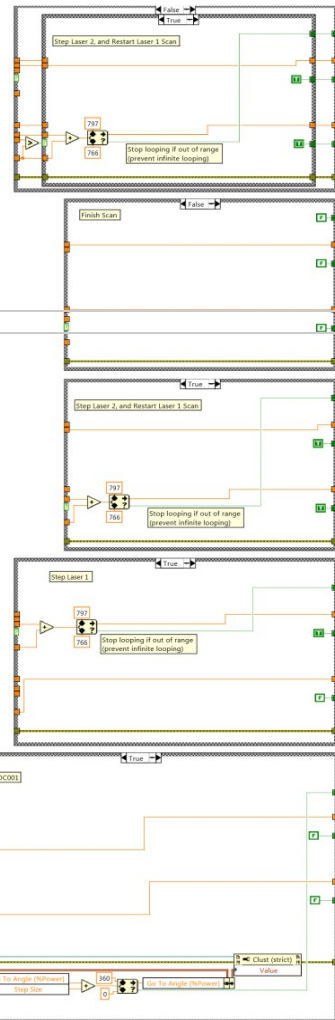
scanning? Save

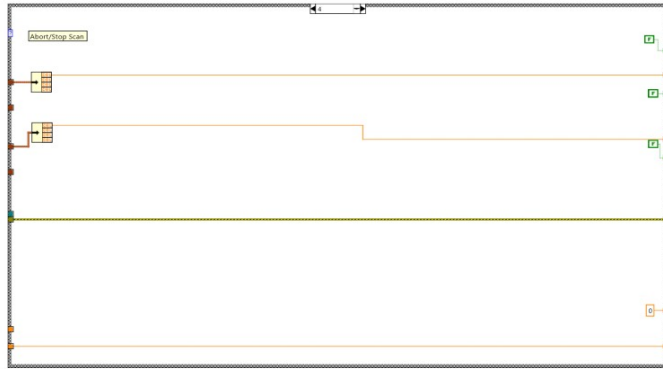
Current Time: 0, Time Left: 00:00:00

error out: status code error 0, source





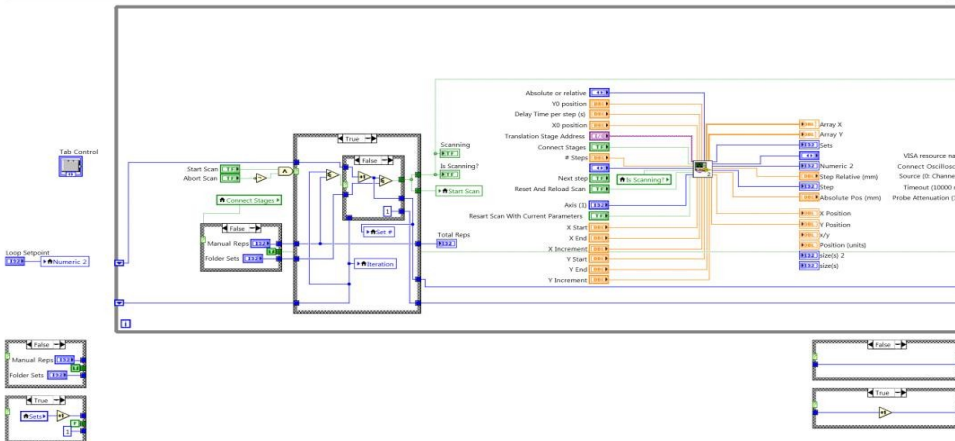
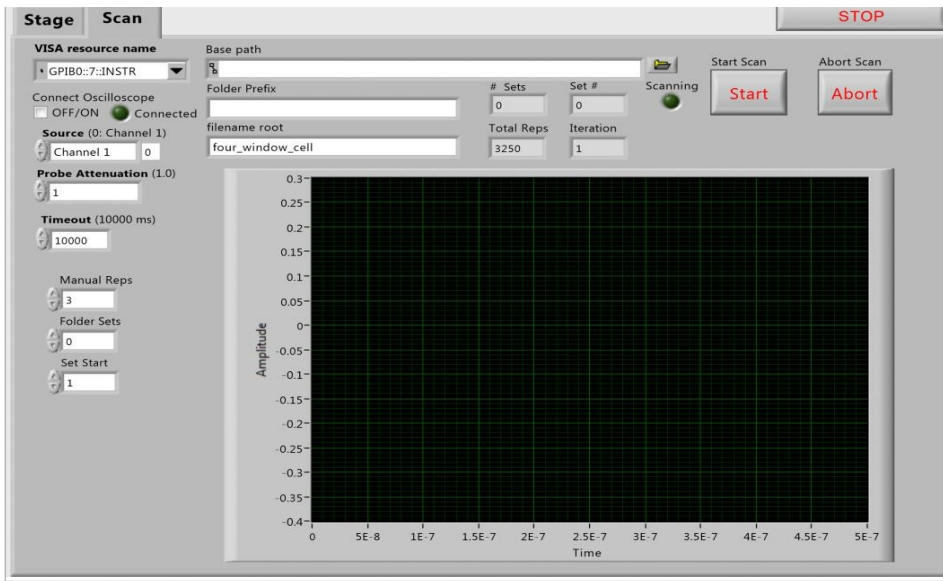


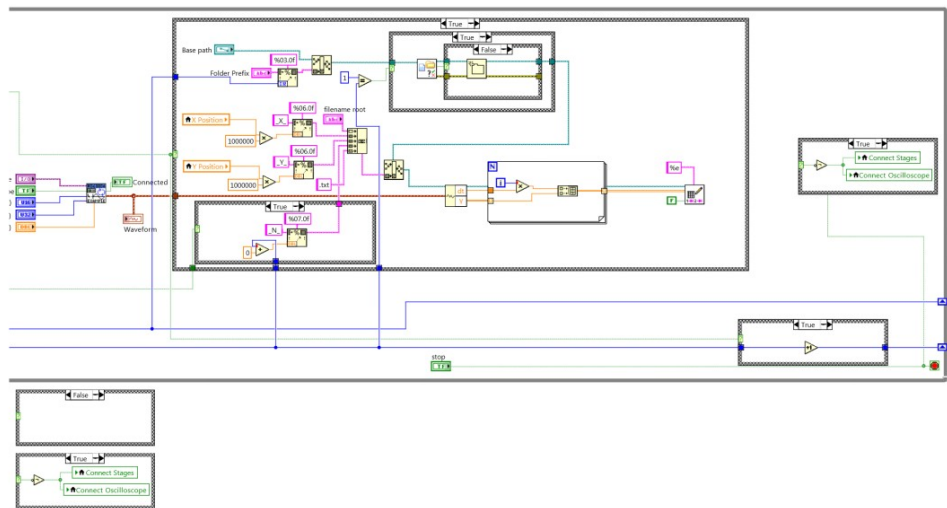


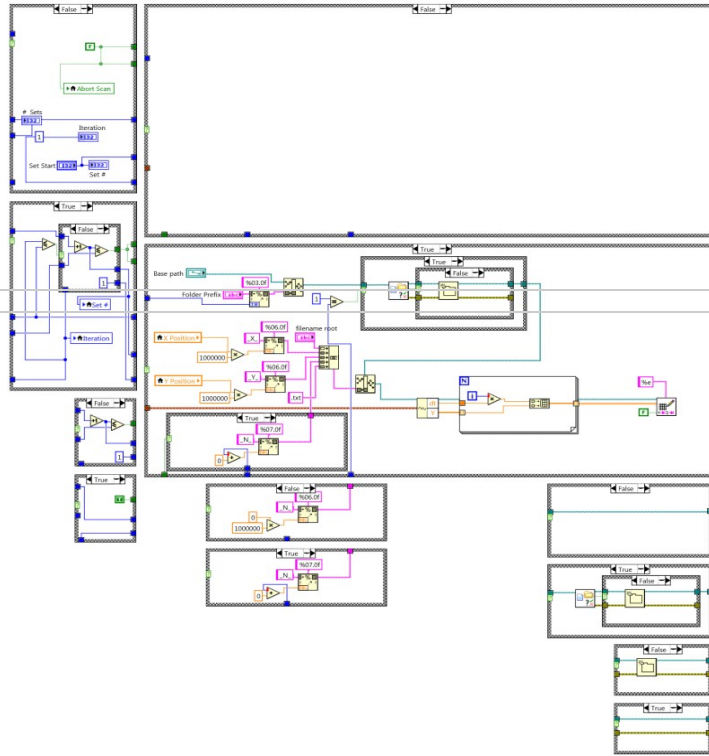
## APPENDIX B

### COMPUTER CODE FOR ISBS MICROSCOPY EXPERIMENT

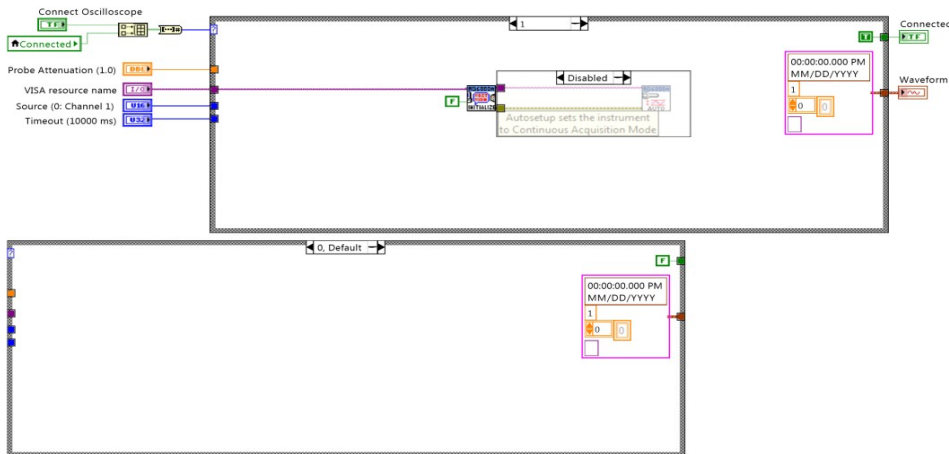
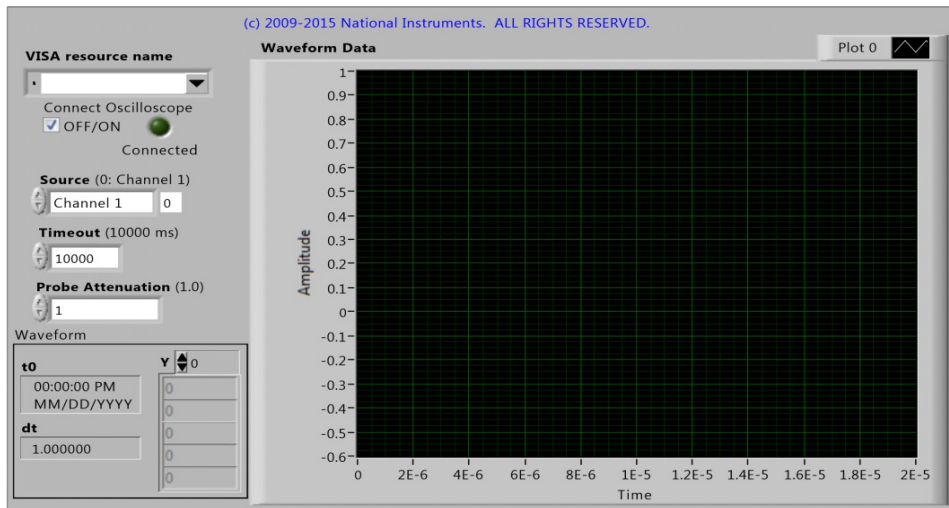
The following is the LabVIEW code to control the ISBS experiment.

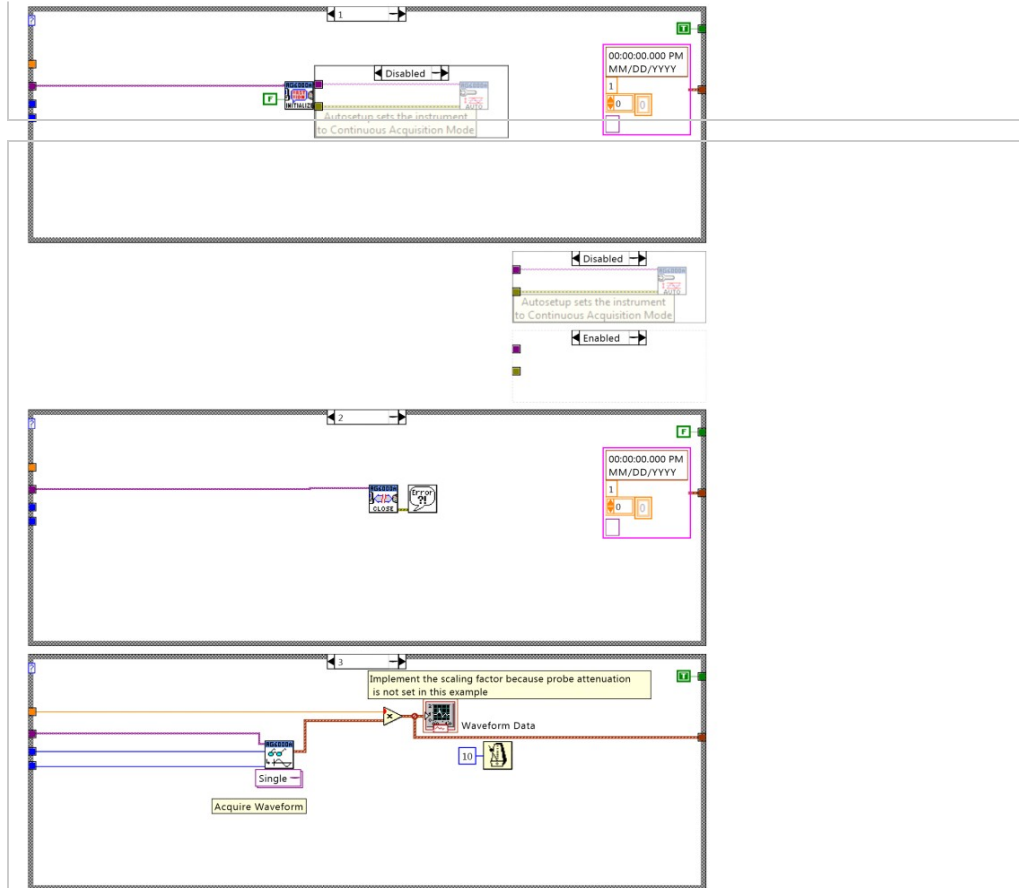












## APPENDIX C

### COMPUTER CODE FOR STATISTICAL COMPARISON EXPERIMENT

This is the computer code used to calculate the Allan Variance of time spectrum data from the oscilloscope. It loads the time data, takes the appropriate averages over the data columns, performs the Fourier transform and finds the frequencies and stores these values, from which it finally computes the Allan Variance.

```
1;
format short e
pkg load optim
tic

%=====
%=====

arg_list = argv()
file_name = arg_list{1};
bg_file_name = arg_list{2};
#file_name = input ("Please enter the file name: ','s');
M=[];

M=load(strcat("Data/",file_name,".dat"));
BG=dlmread(strcat("Data/",bg_file_name,".dat"));
printf("load done...\n");
tmp=[];
```

```

MM=[];
MF=[];
F=[];

skip=50;
precis=0.05;
width=0.5;
f=(2e9/1000)*(0:500);

printf("Before loop...\n");
start=1;
t_lk=length(M(1,:));
t_l=100000;
for l=start:t_l/2

if(l==1)
printf("first if entered...\n");
tmp=M;

for v=1:length(tmp(1,:))
Y=fft(tmp(:,v))-BG(:);
PY=Y.*conj(Y)/1000;
F=PY(1:501);
[r,m]=max(F(skip:end));
d2=m-width+skip-1:precis:m+width+skip-1;

```

```

temp=interp1(F,d2,"spline");
[m2,p2]=max(temp(:));
MM(1,v)=interp1(f,p2*precis+m+skip-2-precis,"spline");
%MM(1,v)=f(m+skip-1);
endfor
tmp=[];
MF(1,3)=mean(MM,2);
Mx(1,:)=1:length(MM)-1;
Mx(2,:)=2:length(MM);
MF(1,2)=0.5*mean((MM(1,Mx(1,:))-MM(1,Mx(2,:))).^2);
MF(1,4)=min(MM);
MF(1,5)=max(MM);
MM=[];
Mx=[];
else
index=1;
for k=1:l:t_lk

tmp=[];
Y=[];
PY=[];
if(k+l-1<=t_lk)

tmp=mean(M(:,k:k+l-1),2);

Y=fft(tmp(:))-BG(:);

```

```

PY=Y.*conj(Y)/1000;
F=PY(1:501);
[r,m]=max(F(skip:end));
check1 = 0;
check2 = 0;
f2=F;

lower_freq_cutoff=50;
%[d1, fm1]=max(f2(5:lower_freq_cutoff-1));

thresholdf=0;
thresholdb=0;
[d3, fm3]=max(f2(lower_freq_cutoff:end));

%if(d3 > 0.00013)

base=mean(f2(40:end));
threshnum=(d3)*0.002+base;
thresholdcomp=(threshnum*1e6);
fm3=fm3+lower_freq_cutoff-1;

#{
while (f2(fm3+thresholdf)*1e6) > thresholdcomp
maxf=fm3+thresholdf;
thresholdf++;

```

```

if( thresholdf+fm3>152 )
check1=1;
break;
endif
endwhile
if(check1 == 0)
while (f2(fm3+thresholdb)*1e6) > thresholdcomp
minb=fm3+thresholdb;
thresholdb--;
if( thresholdb+fm3<50 )
check2=1;
break;
endif
endwhile
endif
#}
if(check1 == 0 && check2 == 0)
%maxn1=maxf;
%minn1=minb;
maxn1=fm3+2;
minn1=fm3-2;
xdat = [minn1:maxn1]';

A0 = [xdat.^2, xdat, ones(size(xdat))];
b = log(f2(xdat));
xs1 = A0\b;

```

```

%sigma0 = abs(1/sqrt(-xs1(1)));
#c1 = -xs1(2)/(2*xs1(1));
c0 = -xs1(2)/(2*xs1(1));
if(c0>lower_freq_cutoff && c0<152)
#intf=f2(floor(c0),1):0.01:f2(ceil(c0),1);
MM(1,index)=interp1(f(:),c0,"spline");
%sigma=((f(maxn1)-f(minn1))/(maxn1-minn1))*sigma0;
%A1 = exp(xs1(3)-(xs1(2)^2)/(4*xs1(1)));

printf("c0 is %f and l is %i\n",c0,l);
else

d2=m-width+skip-1:precis:m+width+skip-1;
temp=interp1(F,d2,"spline");
[m2,p2]=max(temp(:));
MM(1,index)=interp1(f,p2*precis+m+skip-2-precis,"spline");

endif
else

d2=m-width+skip-1:precis:m+width+skip-1;
temp=interp1(F,d2,"spline");
[m2,p2]=max(temp(:));
MM(1,index)=interp1(f,p2*precis+m+
skip-2-precis,"spline");

```



```

endif

%else
% A1=0;
%endif
index++;

else
continue;
endif

endfor

Mx(1,:)=1:length(MM)-1;
Mx(2,:)=2:length(MM);
MF(1-start+1,2)=0.5*mean(( MM(1,Mx(1,:))-
MM(1,Mx(2,:)) )).^2);
MF(1-start+1,3)=mean(MM,2);
MF(1-start+1,4)=min(MM);
MF(1-start+1,5)=max(MM);
MM=[];
Mx=[];

endif

```

```
endfor
```

```
printf("mean and fft's done...\n");
```

```
MF(:,1)=start:t_l/2;
```

```
dlmwrite(strcat("Allan_Variance_",
```

```
file_name, ".dat"), MF, "\t");
```

```
printf("Allan_var of %s done\n", file_name);
```

```
total_time=toc
```